

No-Carrier-Added $^{69/71}\text{Ge}$ and $^{61/64}\text{Cu}$: Copper:

Foundations for Radiotracer and Targeted Radiotherapeutic
Development

By:

Christopher James Kuttyreff

A dissertation submitted in partial fulfillment of the requirements for the degree of

Doctor of Philosophy

(Medical Physics)

at the

UNIVERSITY OF WISCONSIN – MADISON

2022

Date of final examination: 6th of June, 2022

The dissertation is approved by the following members of the Final Oral Committee:

Jonathan W. Engle, Assistant Professor, Medical Physics

Wesley Culberson, Assistant Professor, Medical Physics

Bryan P. Bednarz, Associate Professor, Engineering Physics

Bradley T. Christian, Professor, Medical Physics

Christiaan E. Vermeulen, Physicist, Department of Energy

Acknowledgments

You might think that the hardest part of my life was long since passed, starting a few days after my 21st birthday when my father tragically and unexpectedly passed away. Shortly thereafter, my mother succumbed to prescription pain-killer addiction, and I joined the armed forces to earn money to support my mother and sister, who had just started her undergraduate work at NMSU in Las Cruces. Military training and service were taxing and challenging to me physically, mentally, and spiritually, though I managed to find my way into a military occupational specialty focused on lifesaving, rather than life-taking, operations. If anything, these difficult times served to prepare me for the arduous journey that led me here, to this moment, where I am finally close to accomplishing my professional goals and entering the career field I desire most.

I came to Wisconsin-Madison in June of 2016, far removed from my remaining family and friends. Roughly a 1500-mile drive to reach them from here, that isolation was difficult to bear. My first thanks go to my old friend Jimmie Horne, who helped me to establish some community here by putting me back in contact with other friends from high school, Tari and Dustin Poeppel. Thanks to them for being my friends and supporting me during the incredibly challenging time I had here during graduate school. To my undergraduate friend, Brittany, thank you for continuing to be my friend and for graciously reading my papers and unselfishly offering your time to proofread and revise. Thank you for always showing interest in the things I'm working on and struggling with, especially when no one else seems to care or notice.

I was very fortunate to have been selected as a SciMED graduate research scholar and have the funding and support of that program during my time here. In SciMED, I made my first new friend

here in Wisconsin, ironically a fellow New Mexican also up here for grad school, Luis Torres. Thank you, Luis, for all your comradery and commiseration, for letting me hang out with Kiba when I needed some doggo time, for the trips across the country to visit our families back home, and for introducing me to our friend Galen. You helped me build community and increase my resilience to face the trials and tribulations of our graduate program. Further, you helped me learn the MRI material that was poorly taught by the Socratic method in that class we took together, and without that, I would not have passed my reexamination on that portion of the qualifying exam; I am forever grateful to you for that.

To my friends, Drs. Matt Zammit and Lindsay Bodart, who I met in our cohort here at grad school, thank you both for years of friendship and encouragement. You are among the few who ever spent time with me in my home here in Wisconsin, and Sequoia and I will always remember the way you enriched our lives and helped us to be more socially active. Your successes have been an inspiration to me, and I look forward to following along in your footsteps as I move on to the next phase.

To my friends and neighbors, Dr. Benedict Geiger and his lovely wife Ninja, and their wonderful son Felix, I sincerely thank you for all the many years of your friendship we have enjoyed together, and the many more to come as you hopefully visit me in Arizona, and I you in Germany. Thank you, Ninja, for taking excellent care of Sequoia for me when I had no one else to turn to, and for generously volunteering to walk her for me. Thank you, Ben, for patiently allowing me to practice my rusty German, and for the many valuable discussions we enjoyed over a beer or two. We will never forget you and always miss you guys.

To my fellow students and colleagues in our lab: Jason, Margarita, Aeli, Kaelyn, Kendall, and Wilson. I thank you all for your encouragement and support these past years. Thank you for helping to make the lab a welcoming and accepting place to be. Anymore, science is a team sport, and I am grateful to have had teammates who care about my success and well-being, and who took the time to get to know me personally to better work together. I am sorry I was not a better role model, and for my impatience and grumpiness at times. I consider myself unbelievably fortunate to have been surrounded by such high-caliber people who were understanding and forgiving of my many shortcomings, personally and academically. I know you all will do great things in your lives, and I look forward to being impressed and amazed by them.

To my colleagues and supervisors: Drs. Eduardo Aluicio-Sarduy, Paul Ellison, Todd Barnhart, and Robert “Jerry” Nickles, I thank you all for your patience with me as I learned to be a researcher and member of the group. I could not recount here in the space available all the time you each selflessly volunteered to teach me across a staggering breadth of scientific topics. Any success I enjoy and whatever quality of scientist I have become is because of your incredible support, friendship, leadership, and mentorship these past 5 years. I aspire to your level of academic and professional greatness. Thank you for leading by example, and for not giving up on me.

To my committee members: Drs. Wes Culberson, Bryan Bednarz, Brad Christian, and Christiaan “Etienne” Vermeulen. My sincere and utmost thanks to you all for agreeing to serve on my committee. I am grateful to each of you for all the time, encouragement, and guidance you have offered me along the way, especially when things looked bleakest. You were all instrumental in my success here at UW-Madison, and I know I am a better scientist and medical physicist because of your mentorship and teachings. A special thanks to Etienne, who made himself regularly

available to me to help see me through the hardest parts and to stay positive, sharing his personal experiences and struggles in his Ph.D. work. At no small cost to yourself, you painstakingly carved time out of your life to help me succeed. I am and always will be very grateful.

To my advisor, Dr. Jonathan W. Engle, the words “thank you” will never convey the depth and gravity of my sentiment here. As someone who considers himself a decent leader, in part because of his strong followership, I know I have been a difficult subordinate to mentor. I want to thank you from the bottom of my heart for your dedication and unflinching effort to shape and mold me into a worthy scientist. You have taught me more than I can clearly express about scientific communication, critical thinking, and managing my troublesome temper. Your patience, kindness, and support have paved the way for me as I go on to residency and clinical radiation therapy physics. If all of that was not blessing enough, your support of me through the years when I was not on fellowship allowed me to earn a master's degree and Ph.D. without incurring massive student loan debt. I am forever indebted to you for that. I sincerely hope that one day I might be able to repay you, in any way that I can, and will endeavor to pay it forward both personally and professionally.

And finally, to my family. I love you more than words can say. To the memory of my departed loved ones, Dad, Grandma and Papa Nunz, Baba and Pop Kutyreff, this work and my life are dedicated in part to you. I love and miss you every day. In loving memory of my Papa, Dr. Gregory J. Nunz, this one is for you. It brings me great pride and honor to be your only progeny to carry on your legacy as a scientist, and to be the second Kutyreff in American history to contribute to cancer research; Baba, this one is for you too. As a descendant of Russian, Greek, and German immigrants on both sides, 2 and 3 generations back, and with my Native American heritage from

the Dakota Sioux, I am proud to be a military veteran and soon a Doctor of Medical Physics. Service to this country and our peoples will always be a foremost goal for me.

To my remaining family members: Mom, aunts DeeDee and Becky, uncles Charles, Jamie, Ricky, and Alex, my cousins Ashley and Elisa and their husbands, and my dearest friend and sister, Cherisse. I am sorry for the many years of my absence and distance. Your patience and acceptance of this, your unwavering support and love, all have been invaluable to me, and I would not have succeeded at all without you. I will cherish every moment of our remaining lives together, and I hope I make you proud. To my fur baby, Sequoia, dad loves you more than words can say. Thank you for being there for me in the darkest of times, for lovingly enduring all my many faults and failures as a pet owner/doggy dad. All of this would not have been possible without you, my love.

Abstract

With a growing number of radiotracers approved for clinical use, the development of efficient production of new positron-emitting radionuclides is warranted. Production methods for two novel, PET-imageable radionuclides were developed and reported for medical applications.

First, automated production of no-carrier-added $^{61/64}\text{Cu}$ was developed for a widely proliferated commercial radiosynthesis platform. The developed method will enable the production of $^{61/64}\text{Cu}$ radiotracers at hundreds of facilities worldwide currently using the platform. The synthesis time was 65 minutes and yielded >99% radionuclidically pure $^{61/64}\text{Cu}$ in 2 mL of dilute HCl. Apparent molar activities with NOTA were comparable to the values reported for routine ^{64}Cu produced manually in our lab, on the order of 5 Ci/ μmol . Using enriched target material, we achieved 90 and 95% recycling efficiency of ^{60}Ni and ^{64}Ni , respectively. Future work will focus on cassette-based labeling for single-platform $^{61/64}\text{Cu}$ isolation and radiotracer production.

Second, a growing body of literature describes the potential of Auger-electron-emitting radionuclides in TRT. This, combined with the unique emission spectrum of particles from its decay, makes ^{71}Ge an ideal candidate for probing the microdosimetric effects of low energy electrons absent confounding photon dose. This work reports a novel intermetallic compound of Co and Ga for accelerator production of no-carrier-added $^{69/71}\text{Ge}$. A new extraction chromatography method isolates the Ge product from irradiated Co-Ga targets with high chemical purity and concentration. Thiol-based chelation strategies were investigated for radiolabeling. Preliminary labeling results are encouraging, and work is ongoing to overcome challenges related to the solubility and stability of the radiolabeled complex.

Table of Contents

| | |
|---|-----|
| Acknowledgments | i |
| Abstract | vi |
| Table of Contents | vii |
| List of Tables | ix |
| List of Figures | x |
| Chapter 1: Introduction | 1 |
| 1.1) Organization of the Dissertation | 5 |
| Chapter 2: Automated production of no-carrier-added ^{61/64}Copper | 8 |
| 2.1) Background summary and hypothesis | 8 |
| 2.2) Materials and Methods | 15 |
| 2.2.1) Target Fabrication | 16 |
| 2.2.2) Target Irradiation | 16 |
| 2.2.3) Target Dissolution | 17 |
| 2.2.4) Target Separation | 17 |
| 2.2.5) HPGe and MP-AES Analysis | 19 |
| 2.2.6) AMA and Product Acidity Titrations | 20 |
| 2.3) Results and Discussion | 21 |
| 2.3.1) Target Fabrication and Irradiation | 21 |
| 2.3.2) Irradiated Target Dissolution and Separation | 22 |
| 2.3.3) Final Product Characterization | 23 |
| 2.4) Conclusions | 25 |
| Chapter 3: Gallium-based Targetry for Cyclotron/Accelerator Production of Radiogermanium | 27 |
| 3.1) Background summary and hypothesis | 27 |
| 3.2) Materials and Methods | 32 |
| 3.2.1) Target Fabrication | 32 |
| 3.2.2) Irradiation Configuration and Parameters | 34 |
| 3.2.3) HPGe and CdTe Spectrometry | 35 |
| 3.3) Results and Discussion | 35 |
| 3.3.1) Target Fabrication | 36 |

| | |
|--|-----------|
| 3.3.2) Irradiated Target Performance | 40 |
| 3.3.3) Comparison to previous methods | 48 |
| 3.4) Conclusions | 49 |
| Chapter 4: Isolation and Purification of Radiogermanium from Irradiated Targets | 50 |
| 4.1) Background summary and hypothesis | 50 |
| 4.2) Materials & Methods | 53 |
| 4.2.1) Target Dissolution | 53 |
| 4.2.2) Resin Affinity Studies | 55 |
| 4.2.3) Dynamic Column Separation | 56 |
| 4.2.4) Final Product Characterization | 57 |
| 4.3) Results and Discussion | 58 |
| 4.3.1) Target Dissolution | 58 |
| 4.3.2) Distribution Coefficients (K_D 's) | 59 |
| 4.3.3) Dynamic Column Separation Results | 62 |
| 4.3.4) Total Radiochemical Yields, Radionuclidic Purity, and Separation Factors | 66 |
| 4.4) Conclusions | 68 |
| Chapter 5: Radiolabeling with Radiogermanium | 69 |
| 5.1) Background summary and hypothesis | 69 |
| 5.2) Materials and Methods | 71 |
| 5.2.1) Labeling Conditions for Thiol-based Chelators | 72 |
| 5.2.2) Purification of the Labeled Complex | 74 |
| 5.2.3) Final Product Characterization by radio-HPLC | 75 |
| 5.3) Results and Discussion | 76 |
| 5.3.1) Thiol Complexation Results | 76 |
| 5.3.2) Purification and Stability | 81 |
| 5.4) Conclusions | 88 |
| Chapter 6: Conclusions and Outlook | 89 |
| Appendix A: Additional XRD Data | 91 |
| References | 93 |

List of Tables

| | |
|--|----|
| Table 1: Physical properties of copper radionuclides..... | 8 |
| Table 2: Compilation of product MAs, AMAs and nickel SFs for short and long irradiations..... | 24 |
| Table 3: Measured physical TTY_{EOB} for ARs 1:2 – 1:4..... | 44 |
| Table 4: Experimentally measured ^{69}Ge Y_{EOB} for the various target types investigated..... | 45 |
| Table 5: HPLC binary mobile phase gradient..... | 74 |

List of Figures

| | |
|---|----|
| Figure 1: 2 column separation scheme for $^{61/64}\text{Cu}$ | 18 |
| Figure 2: Photos of a representative target prepared for the investigation..... | 21 |
| Figure 3: Bar diagram presenting the normalized activity distribution of ^{58}Co and ^{61}Cu | 23 |
| Figure 4: The relevant isotopes of gallium and germanium and the nuclear reactions of interest for proton bombardment of natural enrichment gallium targets..... | 27 |
| Figure 5: Cross-section data for expected nuclear reactions in natural enrichment gallium targets..... | 28 |
| Figure 6: Stable isotopes of natural nickel and relevant copper and cobalt radioisotopes produced during proton irradiation..... | 30 |
| Figure 7: Reaction pathways to nickel and cobalt radioisotopes from proton irradiation of cobalt | 31 |
| Figure 8: Thermodynamic model of the Co-Ga system..... | 32 |
| Figure 9: Target irradiation configuration on the GE PETtrace solid target port..... | 34 |
| Figure 10: CoGa_x pellet formed by HTF of elemental cobalt and gallium..... | 36 |
| Figure 11: Measured X-ray diffraction patterns for unmilled & milled AR 1:3 Co:Ga samples..... | 37 |
| Figure 12: The hot-pressing rig with niobium crucible, CoGa_x pellet, boron nitride tamper, and bell-ended quartz glass rod for pressing and gas flow egress..... | 39 |
| Figure 13: A thick and a thin, unmilled CoGa_2 target after hot-pressing into the niobium crucible..... | 40 |
| Figure 14: Proton current applied for the various AR and target types investigated and end-of-bombardment physical yields for AR 1:2 – 1:4 targets..... | 42 |
| Figure 15: Absolute efficiency measured for CdTe detector ~2 cm from detector face versus incident photon energy in keV..... | 47 |
| Figure 16: Measured X-ray spectrum from ^{71}Ge stippled sample..... | 48 |
| Figure 17: Extraction chromatography scheme for NiGa_3 targets dissolved in concentrated HNO_3 using normal DGA Resin..... | 52 |
| Figure 18: Dissolution rig..... | 54 |
| Figure 19: Log of the distribution coefficients (K_D in mL/g) for ^{69}Ge , ^{67}Ga , and ^{58}Co on b. DGA resin in nitric acid determined by HPGe quantification of radioactivity in the solid and liquid phases for 10 or 100 min of contact time..... | 59 |

| | |
|---|----|
| Figure 20: Log of the distribution coefficients for ^{69}Ge , ^{67}Ga , and ^{58}Co on b. DGA resin in nitric acid determined by HPGe quantification of radioactivity in the solid and liquid phases and trace metal analysis data from the liquid phase pre- and post-resin contact for 10 min of contact time..... | 61 |
| Figure 21: Elution profile summary for Co-Ga dissolved in HNO_3 on normal DGA resin with the percentage of ^{69}Ge activity in each fraction..... | 62 |
| Figure 22: Elution profile from the most successful trial separation (1 M Oxalic elutions)..... | 63 |
| Figure 23: Elution profile from the optimized separation scheme..... | 65 |
| Figure 24: HPGe measured gamma spectra of the first eluted fraction from trial b. DGA column..... | 67 |
| Figure 25: Distribution curves of Ge hydroxide complexes..... | 72 |
| Figure 26: Structure of LA and the Mizzou model trithiol chelator with protecting groups for shelf-stability..... | 73 |
| Figure 27: Schematic diagram of the High Performance Liquid Chromatography (HPLC) system..... | 75 |
| Figure 28: HPLC UV-VIS traces for LA pre and post reduction with 10x TCEP..... | 77 |
| Figure 29: Unbound $^{69/71}\text{Ge}$ -oxalate buffered to pH ~5 and $^{69/71}\text{Ge}$ -oxalate after chelation with LA..... | 78 |
| Figure 30: HPLC UV-VIS traces for Mizzou model trithiol chelator pre and post reduction with 10x TCEP..... | 79 |
| Figure 31: Unbound $^{69/71}\text{Ge}$ -oxalate buffered to pH ~5 and $^{69/71}\text{Ge}$ -oxalate after chelation with the Mizzou trithiol..... | 80 |
| Figure 32: C18 cartridge purified $^{69/71}\text{Ge}$ -lipoate after 48 hours in EtOH; $^{69/71}\text{Ge}$ -lipoate immediately following dry-down and reconstitution in PBS; $^{69/71}\text{Ge}$ -lipoate after 24 hours in PBS..... | 81 |
| Figure 33: C18 cartridge purified $^{69/71}\text{Ge}$ -Mizzou C18 purification and dry-down and reconstitution in PBS+Tween 80; $^{69/71}\text{Ge}$ -Mizzou after 4 hours in PBS/Tween80 + Human Serum..... | 82 |
| Figure 34: Proof-of-concept $^{69/71}\text{Ge}$ -Mizzou semi-prep method final product stability results in PBS+Tween 80 and PBS/Tween+Human Serum after 20 hours..... | 84 |
| Figure 35: $^{69/71}\text{Ge}$ -Mizzou semi-prep method development and RT recharacterization test run injected with UV-VIS flow cell online and full reaction solution injection with UV-VIS flow cell bypassed..... | 85 |
| Figure 36: $^{69/71}\text{Ge}$ -Mizzou stability after reformulation in PBS+Tween and PBS/Tween+Human serum over 72 – 96 hours..... | 86 |

| | |
|--|----|
| Figure 37: Serum pellet radioactivity accumulation during $^{69/71}\text{Ge}$ -Mizzou PBS & PBS+Human Serum stability study..... | 87 |
| Figure A1: Measured X-ray diffraction patterns for unmilled & milled AR 1:2 Co:Ga sample..... | 91 |
| Figure A2: Measured x-ray diffraction pattern for AR 1:4 unmilled Co:Ga sample..... | 92 |

Chapter 1: Introduction

Positron-emission tomography (PET) imaging is an important clinical tool for diagnosis and staging in radiation oncology [1,2]. ^{18}F ($T_{1/2} = 109.77$ m, $I_{\beta^+} = 96.73\%$, $E_{\text{max}, \beta^+} = 633.5$ keV) labeled agents have become the PET workhorse similar to $^{99\text{m}}\text{Tc}$ ($T_{1/2} = 6.01$ h, $I_{\gamma} = 89\%$, $E_{\gamma} = 140.5$ keV) agents in conventional single photon emission computed tomography (SPECT) imaging [3]. Numerous radiotracers have been developed for PET imaging; in addition to ^{18}F , the current palette of radioisotopes for clinical PET includes ^{11}C ($T_{1/2} = 20.36$ m, $I_{\beta^+} = 99.77\%$, $E_{\text{max}, \beta^+} = 960.4$ keV), ^{13}N ($T_{1/2} = 9.97$ m, $I_{\beta^+} = 99.80\%$, $E_{\text{max}, \beta^+} = 1198.5$ keV), and ^{15}O ($T_{1/2} = 2.04$ m, $I_{\beta^+} = 99.9\%$, $E_{\text{max}, \beta^+} = 1732$ keV), and ^{68}Ga ($T_{1/2} = 67.71$ m, $I_{\beta^+} = 87.7\%$, $E_{\text{max}, \beta^+} = 1899$ keV) [4,5]. However, the short half-lives of most of these radionuclides require a direct supply (e.g. production on a local small cyclotron) and are not amenable to regional distribution. ^{18}F , with its ~2-hour half-life, is an exception to this and is regionally distributed allowing clinical PET imaging in areas without dedicated cyclotrons for radionuclide production.

^{61}Cu ($T_{1/2} = 3.34$ h, $I_{\beta^+} = 51\%$, $E_{\text{max}, \beta^+} = 1215.8$ keV) is a positron-emitter which can be produced on small cyclotrons and has sufficient half-life to enable regional distribution [6]. Additionally, ^{61}Cu is chemically identical to ^{64}Cu ($T_{1/2} = 12.7$ h, $I_{\beta^+} = 17.49\%$, $E_{\text{max}, \beta^+} = 652.6$ keV) and therefore amenable to the same radiochemical preparations. ^{64}Cu tracers have been studied extensively, from the intrinsic targeting properties of $^{64}\text{CuCl}_2$ to PET imaging vectors like ASTM, PSMA, and monoclonal antibody fragments like trastuzumab and cetuximab [7,8]. In 2020, the first ^{64}Cu -labeled radiopharmaceutical for PET/CT imaging was approved by the Food and Drug Administration (FDA), ^{64}Cu -DOTATATE (Detectnet™) [9]. ^{64}Cu can potentially be employed as a

therapeutic radionuclide due to its emission of Auger electrons and β^- particles [7,10]. Combined, $^{61/64}\text{Cu}$ represent a potential theranostic pair. As noted in the review by Yordanova et al [11], “The theranostic approach in nuclear medicine couples diagnostic imaging and therapy using the same molecule or at least very similar molecules, which are either radiolabeled differently or given in different dosages.” Current challenges in oncology treatment include the fact that elderly patients are typically unfit for conventional chemotherapy due to comorbidities and poor performance, and the occurrence of side effects may aggravate treatment compliance in young and old alike [11]. Because of these, the combination of targeted cancer imaging and therapy represents an important advance in personalized medicine [11].

Another potential therapeutic radionuclide of copper is ^{67}Cu ($T_{1/2} = 61.83$ h, 100% β^-) which emits energetic betas, Auger electrons, and a 184.6 keV photon (48.7%). However, direct production of ^{67}Cu is limited due to the lack of a dedicated network of nuclear reactors and high-energy cyclotrons to supply the radionuclide [10]. On the other hand, the International Atomic Energy Agency (IAEA) Database of Cyclotrons for Radionuclide Production reports nearly 250 small cyclotrons in the US alone, and the production of ^{64}Cu on small cyclotrons is established [12]. Production of radionuclides by charged particle bombardment (i.e. on small cyclotrons) yields carrier-free radionuclides transmuted from the bombarded target material which is comprised of a different chemical element. Thus, the only stable isotopes of the element being produced are those present as trace impurities in the target material which are not chemically separable from the produced radionuclides. Carrier-free tracers are rarely obtained in radionuclide production, so carrier-free specific activity represents a theoretical maximum purity. On the other hand, no-carrier-added indicates that no deliberate addition of stable isotopes to the

produced radioactivity has occurred and that the radioactive product is essentially free from stable isotopes of the same element [13] which indicates a high purity but not necessarily the theoretical maximum.

With its longer half-life, ^{64}Cu can be distributed coast-to-coast in the continental United States. Automated production of $^{61/64}\text{Cu}$ on small medical cyclotrons has the potential to shorten production times and minimize dose to the operators. For these reasons, automated $^{61/64}\text{Cu}$ production using a variety of target transfer systems and automated chemistry modules has been reported [14,15]. Currently, the GE FASTlab™ (FASTlab) chemistry module is widely distributed and used for the automated production of good manufacturing process (GMP) compliant radiotracers, with more than 740 modules reported in use around the world [16]. In collaboration with GE Healthcare, we developed an automated production method using an ARTMS QiS target transfer and dissolution system in series with a FASTlab chemistry module for use at our institution. The successfully developed method will increase the availability of $^{61/64}\text{Cu}$ radiotracers by enabling seamless incorporation of the production method at facilities currently using FASTlab modules for the synthesis of other clinical radiotracers.

In addition to radioisotopes of copper, a handful of transition radiometals are emerging for PET applications. Longer lived radionuclides like ^{86}Y ($T_{1/2} = 14.74$ h, $I_{\beta^+} = 11.9\%$, $E_{\max, \beta^+} = 1221$ keV) and ^{89}Zr ($T_{1/2} = 78.41$ h, $I_{\beta^+} = 22.74\%$, $E_{\max, \beta^+} = 902$ keV) have been reported on with sufficient half-lives for long-range distribution as well as for *in vivo* applications requiring longer circulation times (e.g. monoclonal antibodies and fragments) [4,5,8,17–20]. With the aim of broadening the palette of available PET radioisotopes, ^{69}Ge ($T_{1/2} = 39.05$ h, $I_{\beta^+} = 21\%$, $E_{\max, \beta^+} = 1205.1$ keV) is worthy of investigation. Its relatively long half-life enables long-range distribution or use of

tracers with long circulation times *in vivo*. Additionally, many potential *in vivo* roles for naturally occurring germanium have been identified, including antitumoral activities related to cell killing, as well as antimicrobial effects [21]. However, the mechanisms underlying these activities are not well understood, and ^{69}Ge PET could confirm and elucidate some of these findings.

Furthermore, there is a growing interest in Auger-electron emitting nuclides (e.g. ^{161}Tb and ^{111}In [22], ^{135}La [23], and $^{58\text{m}}\text{Co}$ [24]) in targeted radiotherapy (TRT) due to their high linear energy transfer (LET), short-range emissions. Because of its longer half-life and emission of four to seven 0.005 – 10 keV Auger electrons per decay [25,26], ^{71}Ge is an interesting model radionuclide for TRT, especially for agents with longer circulation times. Its only other emissions are relatively low intensity 9 – 10 keV X-rays (~44%, combined), which make ^{71}Ge unique as a probe of low energy electrons' microdosimetric effects absent confounding photon dose. So-called "perfect Auger emitters" emit the majority of their decay energy via <50 keV Auger electrons [27]. Together, $^{69/71}\text{Ge}$ also represent a potential theranostic pair meriting investigation into their efficient production and isolation. Few descriptions of germanium radioisotopes' production ($^{69/71}\text{Ge}$) are found in literature and none that might enable *in vitro* or *in vivo* applications [5,28,29].

For both $^{61/64}\text{Cu}$ and $^{69/71}\text{Ge}$, theoretical thick-target yields (TTYs) at end-of-bombardment (EoB) were calculated using the formalism recommended by the IAEA [30], given below:

$$Y_{\text{EoB}}[\text{Bq}] = \frac{N_A}{A_T} * I * (1 - e^{-\lambda_D * t_{\text{irrad}}}) \int_{E_E}^{E_I} \frac{\sigma_T(E)}{S_T(E)} dE$$

N_A is Avogadro's number (atoms per mole), A_T is the molar mass of the target (grams per mole), I is the number of protons per second incident on the target, λ_D is the decay constant of the

produced radionuclide (s^{-1}), t_{irrad} is the duration of the irradiation (in seconds), $\sigma_T(E)$ is the nuclear reaction cross-section (in cm^2), $S_T(E)$ is the total stopping power of the target medium ($\text{MeV}\cdot\text{cm}^2$ per gram), and dE is the incremental change in energy (MeV) integrated over the incident (E_i) to exit (E_E) proton energies. The stopping powers were obtained from the SRIM program [31]. Experimentally measured cross-section data were used wherever possible. However, the cross-section data for $^{71}\text{Ga}(p,n)^{71}\text{Ge}$ has not been measured above 7 MeV, so theoretically predicted cross-section data were utilized in this case.

This work reports an automated $^{61/64}\text{Cu}$ production using existing infrastructure in our lab which has not previously been employed for this task. Additionally, the first report on the use of an intermetallic cobalt/gallium target for $^{69/71}\text{Ge}$ production is presented along with the radiochemical isolation method developed around extraction chromatography. A detailed review of copper radionuclide production and radiochemical isolation is included in the introduction of Chapter 2. Similarly, detailed reviews of germanium radionuclide production, radiochemical isolation, and germanium radiolabeling/chelation are included in the introductions of Chapters 3, 4, and 5, respectively.

1.1) Organization of the Dissertation

Chapter 2 describes the development of an automated production and radiochemical isolation process for $^{61/64}\text{Cu}$. An electrodeposition process for the nickel target material was adapted to deposit the material on silver backings. Modification of the ARTMS QiS target transfer dissolution unit's fluid pathways is discussed along with the enabling of target material recycling with the

process. And finally, the characterization of the radionuclidic and chemical purity of the copper product is evaluated.

Chapter 3 details the development of a novel intermetallic target material for accelerator production of $^{69/71}\text{Ge}$. Most notably, the development of a durable material in beam is described. A method for quantification of ^{71}Ge by low-energy X-ray spectrometry was developed, and the $^{69/71}\text{Ge}$ end-of-bombardment yields were measured. Characterization of the new target material was attempted by X-ray diffractometry (XRD).

Chapter 4 covers the development of the radiochemical isolation of $^{69/71}\text{Ge}$ from the irradiated bulk target. To avoid the formation of volatile and radioactive $^{69/71}\text{GeCl}_4$ and mitigate the associated hazards, extraction chromatography was investigated for targets dissolved in concentrated nitric acid. Distribution coefficients were measured for the extraction chromatography resin, and a dynamic column separation technique was developed. The final product was characterized by high-purity germanium (HPGe) and microwave plasma atomic emission spectrometry to assess radionuclidic and chemical purity.

Chapter 5 presents the investigation of radiolabeling of thiol-based chelators with $^{69/71}\text{Ge}$. Inspired by reports in the literature on the complexation of stable germanium with thiol compounds, lipoic acid and a model trithiol chelator developed by the Jurrison group at the University of Missouri (Mizzou) were explored for their ability to chelate the $^{69/71}\text{Ge}$ product. Attempts were made to purify labeled compounds by C18 cartridge and semi-preparatory high-performance liquid chromatography (HPLC). And finally, the stability of the labeled compounds

in phosphate-buffered saline (PBS) and PBS/Human serum mixture was assessed by analytical HPLC.

Appendix A contains additional XRD data collected during the characterization of the target material (chapter 3).

Chapter 2: Automated production of no-carrier-added $^{61/64}\text{Cu}$

2.1) Background summary and hypothesis

Copper radioisotope production has been studied extensively over the past 3 decades for radiolabeling of diagnostic imaging tracers and targeted radiotherapy agents. There are 5 relevant radioisotopes of copper for diagnostic imaging and therapy applications. The table below summarizes the properties of the copper radionuclides used in nuclear medicine:

| Radionuclide | $T_{1/2}$ (hours) | Decay Mode | β^+_{max} keV (%) | β^-_{max} keV (%) | γ keV (%) | Source |
|------------------|----------------------|-------------------------------------|-----------------------------------|-----------------------------------|--|---------------------|
| ^{60}Cu | 0.40 | 100 % ϵ | 3774 (93) | | 826 (22) 1333 (88) 1792 (45) | cyclotron |
| ^{61}Cu | 3.34 | 100 % ϵ | 1216 (61) | | 283 (13) 656 (10) | cyclotron |
| ^{62}Cu | 0.16 | 100 % ϵ | 2937 (98) | | | cyclotron/generator |
| ^{64}Cu | 12.7 | 61.5% ϵ 38.5% β^- | 653 (18) | 580 (39) | | cyclotron |
| ^{67}Cu | 61.8 | 100 % β^- | | 377 (57) 468 (22) 562 (20) | 93 (16) 185 (49) | cyclotron/reactor |

Table 1: Physical properties of copper radionuclides: half-life in hours, decay modes, maximum positron energy with total positron intensity, beta minus energies and intensities, prominent gamma emissions and intensities, and source of production [32,33]

^{60}Cu is a positron-emitting isotope of copper that can be produced on small cyclotrons and is suitable for diagnostic imaging with its high positron branching ratio, but its relatively high positron energy, as compared to ^{18}F and ^{64}Cu , leads to poorer spatial resolution for diagnostic PET imaging. The high-energy, high-intensity gammas from ^{60}Cu and associated radiation dose make ^{60}Cu -based radiotracers less attractive for *in vivo* applications. ^{62}Cu is another positron-emitting isotope of copper that can be produced on small cyclotrons or obtained from a radionuclide generator (RNG), $^{62}\text{Zn}/^{62}\text{Cu}$. Like ^{60}Cu , ^{62}Cu is also suitable for diagnostic imaging with its high positron branching ratio but also suffers from poorer spatial resolution due to the relatively high positron energy. However, ^{62}Cu lacks appreciable gamma emissions making it more attractive for diagnostic imaging. ^{61}Cu has a high positron branching ratio and relatively low positron energy, compared to ^{60}Cu and ^{62}Cu , which makes it an attractive candidate for radiotracer applications. Additionally, its relatively long half-life comparable to ^{18}F make it suitable for regional distribution in addition to local cyclotron production. Although, ^{61}Cu does emit a few energetic gammas with low intensity. ^{64}Cu has the most attractive positron energy of the positron-emitting isotopes of copper. In general, the lower the positron energy, the better the spatial resolution in PET scanners due to shorter positron ranges for the annihilation events. In addition, ^{64}Cu has been described as a theranostic isotope [7,10] due to its positron emission suitable for PET imaging and beta minus + auger electron emissions suitable for targeted radiotherapy applications, and no gamma emissions with intensities above 1%. Last on the list, ^{67}Cu is an ideal candidate for targeted radiotherapy with its longer half-life and emission of multiple energetic betas. Its low-energy gammas are potentially useful for SPECT imaging.

^{60}Cu is easily produced on small cyclotrons at 11 MeV through the $^{60}\text{Ni}(p,n)^{60}\text{Cu}$ nuclear reaction pathway [33–35]. The enriched nickel material is recycled for subsequent productions. ^{61}Cu is also easily produced on small cyclotrons, both through the $^{60}\text{Ni}(d,n)^{61}\text{Cu}$ or $^{\text{Nat}}\text{Ni}(p,n)^{61}\text{Cu}$ nuclear reaction pathways [6,33] where the latter also yields short-lived isotopes of copper which decay rapidly during the separation and formulation chemistries and also some trace amounts of stable copper. ^{61}Cu can also be produced using enriched ^{61}Ni targets and proton bombardment at 11 MeV [33], proton bombardment of ^{64}Zn at 11 MeV [35], proton bombardment of $^{\text{Nat}}\text{Zn}$ at 30 MeV [36], or alpha bombardment of $^{\text{Nat}}\text{Ni}$ at 21 MeV or $^{\text{Nat}}\text{Co}$ at 40 MeV [37]. But, the cost of the enriched ^{61}Ni is quite high, demanding careful recycling of the enriched target material, making the natural enrichment targets more attractive for production. ^{62}Cu can be produced on small cyclotrons using enriched ^{62}Ni targets and proton bombardment at 10 – 14 MeV [33,35,36,38] or obtained from a generator using the parent radionuclide ^{62}Zn ($T_{1/2} = 9.186$ h, 100% ϵ) [33,36,38]. The use of the RNGs enables PET imaging at sites lacking a dedicated cyclotron for radionuclide production.

^{64}Cu production has been extensively studied and reported in several publications [12,33,36,37,39–42]. The production uses enriched ^{64}Ni and the p,n nuclear reaction, capitalizing on the peak of the cross-section through 9 – 12 MeV and yielding the product in high specific activity [33,35,36,41]. At these energies, the p, α nuclear reaction pathway also yields high-purity ^{61}Co , as reported by [12] which must be separated from the final product along with the bulk target material. ^{64}Ni is the costliest of the enriched nickel isotopes for copper radionuclide production (\$40-50 USD/mg), necessitating a high recycling efficiency for the production method to be cost-effective. ^{64}Cu can also be produced by neutron bombardment through the

$^{63}\text{Cu}(n,\gamma)^{64}\text{Cu}$ nuclear reaction pathway, yielding primarily ^{64}Cu and some ^{66}Cu which decays rapidly ($T_{1/2} = 5.1$ min) [36,37]. This method does suffer the drawback of low specific activity due to the large amount of stable copper which is not chemically separable from the final product. Another neutron production pathway for ^{64}Cu does yield a final product with high specific activity through the $^{64}\text{Zn}(n,p)^{64}\text{Cu}$ pathway, where the zinc target material is chemically separable from the final product [36,37]. However, unless using isotopically enriched target material, the final product contains appreciable ^{67}Cu , limiting the utility of the final product. And finally, ^{67}Cu production is accomplished either by high-flux neutron irradiation of ^{67}Zn to access the n,p nuclear reaction pathway or photonuclear reaction using the γ,p nuclear reaction on ^{68}Zn [33,36,43]. Charged particle reactions on enriched zinc targets can also be employed to produce ^{67}Cu , but suffer from high-cost enriched target material, the coproduction of undesirable radionuclidic impurities, the need for high energy particle bombardment available at few facilities, and the limited quantities produced [33,36,43].

Radiochemical isolation of ^{64}Cu depends greatly on the target material employed for the production and falls generally into 2 cases: nickel or zinc targets. For the nickel targets, the primary method for radiochemical isolation is liquid chromatography using anion exchange resin (AG-1x8) with targets dissolved in HCl [12,33,39,42,44]. Other radioisotopes of copper ($^{60,61,62}\text{Cu}$) produced using nickel targets can be separated in the same way. The use of zinc target material and additional coproduced radiochemical impurities using this approach require a different isolation strategy. The zinc targets are also dissolved in HCl, followed by liquid-liquid extraction of the gallium radionuclides in solution, and finally separation of the copper radioactivity from the zinc target material on AG-1x8 anion exchange chromatography resin [40]. Another approach

uses a 2-column separation scheme, where the zinc target is dissolved in HCl and passed through a cation exchange chromatography resin (AG 50W H⁺) to remove radiogallium followed by anion exchange chromatography on AG-1x8 to isolate the desired copper product [36]. ⁶¹Cu, when produced from zinc targets, can also be isolated in these ways.

Radiochemical isolation of ⁶⁷Cu from the bulk zinc target material is more challenging due to the large amounts of zinc necessary to achieve relevant yields, and is accomplished in 1 of 4 ways after HCl dissolution of the irradiated target: ion exchange liquid chromatography, electrodeposition, liquid-liquid extraction, and sublimation [43]. The ion exchange chromatography approach uses an anion exchange column either as the only separation technique or in combination with a chelation column (i.e. Chelex-100) and/or a cation exchange column (Bio-Rad AG-50W). The electrodeposition method involves the use of platinum mesh electrodes on which the ⁶⁷Cu is deposited and subsequently off which the copper product is dissolved. The liquid-liquid extraction is cumbersome: 0.01% dithizone in carbon tetrachloride is contacted with the HCl-dissolved, irradiated target, the copper activity is back extracted into ~7 M HCl mixed with hydrogen peroxide, the copper product is separated from radiogallium impurities by contacting with isopropyl ether, and finally the ~7 M HCl solution is passed through an anion exchange column to remove nickel, manganese, chromium, and cobalt radioimpurities. Sublimation under vacuum at 800 °C removes the bulk zinc, while some pure tin added prior to heating prevents entrainment of the copper product with the zinc vapor. The remaining tin-copper pellet is dissolved in HCl and separated on an ion exchange column.

Seeking to reduce the dose to operators and overall radiochemical isolation process time while increasing the availability of copper radiotracers, automated production of ⁶⁴Cu has been

developed and reported in several publications [14,15,45–47]. One such fully automated method uses the Alceo system (Comecer S.p.A., Italy) to electroplate a nickel target on a gold backing, transfer the plated target to and from the cyclotron irradiation port, dissolve the irradiated target and separate it using ion exchange chromatography, and to label ASTM with the copper activity, all under computer control [47]. Unfortunately, in our lab and labs of our collaborators, the Alceo system's reliability and compatibility of the process with downstream radiochemistry pose significant operational challenges. Another approach, reported by [45], describes a semi-automated method using the Pinctada Metal system (IBA, Belgium) for automatic electroplating and dissolution of the nickel target on silver backings and separation of the dissolved target by anion exchange. Target transfer to and from the cyclotron, as well as any radiolabeling, were accomplished manually following this method. Another automated production method reported by [15] used the COSTIS target transfer station and a home-made separation module to process the irradiated target after dissolution using anion exchange resin. In this method, transfer of the irradiated target to the dissolution unit and transfer of the dissolved target solution to the separation module were accomplished manually, resulting in a semi-automated approach. The semi-automated approach described by [14] uses home-made target transfer and separation modules for the automated steps, while electrodeposition of the target and transfer of the irradiated target from the transfer module to the separation module are the manual steps in the process. This method also uses anion exchange resin to separate the dissolved target. Last, the method from [46] also used home-made target transfer and separation modules, and with the aid of robotic arms and manipulators all steps in the production were automated except for the electrodeposition of the nickel target material. The method uses ion exchange chromatography

to effect the separation of the copper activity from the dissolved target solution. None of these methods are well disseminated globally, so there is clear room for improvement to increase the appeal and use of Cu radiotracers.

Another commercial radiosynthesis platform is available for separation and labeling chemistry and is widely proliferated with more than 740 units in operation around the world: the GE FASTlab. The module is cassette-based, meaning that resins and reagents are preloaded for each production. Cassette-based methods are easily introduced into GMP environments [6]. Over the past decade the module has been used extensively for automated production of numerous ^{18}F -labeled tracers: [^{18}F]FET- β AG-TOCA [48], [^{18}F]FDOPA [49,50] & F-tyrosine [49], [^{18}F]FDG [51], [^{18}F]DCFPyL [52], [^{18}F]FSPG [53], [^{18}F]SFB [54], [^{18}F]fluoropropoxybenzene [55], and [^{18}F]molecules for TSPO targeting [56]. In addition, many ^{68}Ga -labeled tracers have also been synthesized on the module: [^{68}Ga]-DOTA and NODAGA conjugated peptides [57], [^{68}Ga]-DOTATOC, DOTANOC, and DOTATATE [58], and [^{68}Ga]-PSMA-11 and DOTATATE [59]. The module has also been used to synthesize OncoFAP-based radiopharmaceuticals with ^{18}F , ^{68}Ga , and ^{177}Lu [60].

High purity ^{64}Cu is routinely produced in our lab following the method of [12]. Weekly, several hundred mCi are produced and shipped to customers across the continental US for radiopharmaceutical preparation and investigation, with demand continuing to rise as more copper-based radiopharmaceuticals are translated into clinical application [7,9]. The manual production process requires an operator to transport the irradiated target to the chemistry station, perform the separation, and reformulate the final product for distribution. Automation of this process has the obvious benefit of reducing the dose to the operator as production is

scaled up. Automation could also shorten the processing time. Further, the use of kit and cassette-based methods makes GMP compliance easier to achieve [61].

A few reports are available from the literature on successfully automated processes developed and implemented at other institutions in the US and Europe [14,15]. Inspired by their successes, we hypothesized that production could be automated using available infrastructure in our lab (the ARTMS QiS target transfer and dissolution system and the FASTlab chemistry module) to yield radiopharmaceutical quality $^{61/64}\text{Cu}$. Herein, automated production of ^{61}Cu was investigated to achieve this goal.

2.2) Materials and Methods

Natural Ni powder (99.8%, 325 mesh) was purchased from Alfa Aesar. Concentrated HNO_3 (Optima Grade) was purchased from Fisher Chemical. Concentrated H_2SO_4 (Optima Grade) and NH_4OH (28%, Optima Grade) were purchased from Fisher Scientific. 18 $\text{M}\Omega\cdot\text{cm}$ D.I. water (hereafter referred to as D.I. water) was obtained from a Millipore Synergy UV in-lab water supply. $(\text{NH}_4)_2\text{SO}_4$ (99.9999%, Puratronic) was purchased from Alfa Aesar. Concentrated HCl (Ultrapur) and H_2O_2 (30%, ultratrace analysis) were purchased from Merck. TBP resin (tributyl-phosphate, particle size 50–100 μm , pre-packed) and TK201 resin (tertiary-amine-based weak ionic exchange resin containing a small amount of a long-chained alcohol, particle size 50–100 μm , pre-packed) were purchased from Triskem International. NaCl (ACS Grade), sodium acetate (anhydrous, 99% pure), Whatman pH strips, and aluminum-backed silica thin-layer chromatography (TLC) plates were purchased from Fisher Scientific. Trace metal standards for

Co, Cu, Fe, Ni, and Zn (1000 mg/L) were purchased from Sigma Aldrich. NOTA (1,4,7-triazacyclononane-1,4,7-triacetic acid) was purchased from Sigma Aldrich.

2.2.1) Target Fabrication

Adapting the method of [38], natural enrichment nickel targets were electrodeposited onto silver backings. Nickel powder was dissolved in 2 mL of concentrated HNO₃ and taken to dryness at 85 °C under N₂ gas flow. The dried nickel was reconstituted in 2.3 mL of 2.4 M H₂SO₄, and the solution pH was adjusted to ~9.1 with ~2.5 mL of concentrated NH₄OH. Then, 250 – 300 mg of ammonium sulfate salt was added to the mixture, which was quantitatively transferred to the electrochemical cell. Using a platinum wire cathode and laboratory DC power supply, optimum electroplating conditions were investigated by applying 40 – 90 mA of constant current and voltages ranging from 6 – 7.5 V to the static cell for 1 – 4 days. The same setup and plating process were used to recycle nickel target material after irradiation and target processing, with an additional first step of drying down the nickel solution from the separation chemistry. For the proof-of-concept ⁶⁴Ni run, enriched nickel was electrodeposited on a gold backing following the method of [38] directly.

2.2.2) Target Irradiation

Following electrodeposition, the natural enrichment nickel targets were irradiated on our GE PETtrace 800 cyclotron with 8.4 MeV deuterons on the target port outfitted with the ARTMS QiS automated target transfer system. Beam currents of 20 – 30 μA were applied for 30 min during initial testing. One target was irradiated for one half-life of ⁶¹Cu (3.3 h) to investigate the scale-up potential for the production process. 1x- and 2x-recycled targets were irradiated to investigate the efficacy of the recycling process. To aid in method optimization, natural enrichment targets

were also irradiated for 1 min with 1 μA of proton current to produce additional cobalt radioisotopes for tracer in the separation process. For the proof-of-concept ^{64}Ni run, the enriched target was irradiated with 20 μA of 13.1 MeV protons for 1 hour.

2.2.3) Target Dissolution

After irradiation, targets were automatically recalled to the hot cell from the cyclotron target port and manually transferred to the ARTMS QiS dissolution unit using 1 m tongs. Informed by benchtop studies performed by our collaborators [6], dissolution was achieved using 3 mL of a 1:1 mixture of 7 M HCl :: 30% H_2O_2 and heat. Based on a set point of 111 $^\circ\text{C}$ for the heater sleeve and measurements with an external thermal probe, the dissolution temperature was ~ 60 $^\circ\text{C}$. The acid/peroxide mixture was recirculated across the target face at 2 mL/min for 20 minutes, then mixed with 3 mL of 11.1 M HCl with 90 s of air bubbling through the solution. Before transfer to the FASTlab for separation, the sequence was paused and ~ 200 μL aliquots of the dissolved target solutions were removed for analysis. For the proof-of-concept ^{64}Ni run, the irradiated target was dissolved manually on a benchtop dissolution block and transferred to the FASTlab using the ARTMS QiS dissolution unit pump. All dissolved target solutions were transferred at 1 mL/min.

2.2.4) Target Separation

Dissolved, irradiated targets were separated using the FASTlab module and cassettes preloaded with 1 mL TBP and 2 mL TK201 resin cartridges and reagent vials containing 5 M NaCl in 0.05 M HCl and 6 M HCl. The resins were automatically equilibrated in series with 7 mL of D.I. water followed by 6 mL of 11.1 M HCl. The separation scheme is illustrated in the figure below:

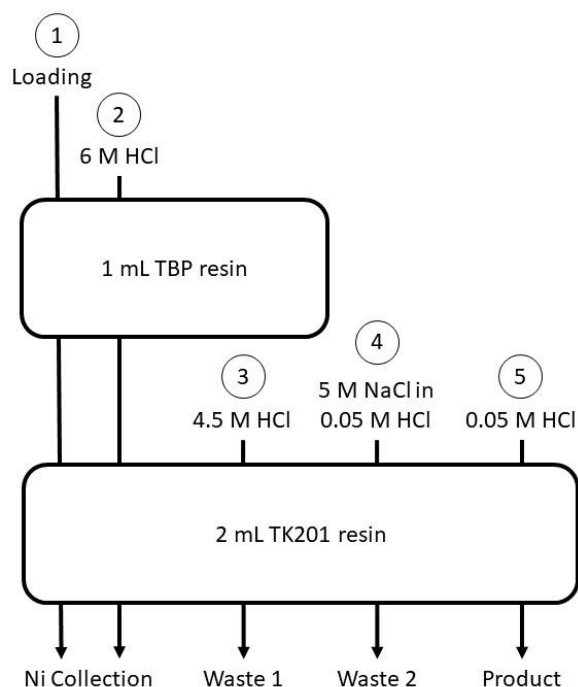


Figure 1: 2 column separation scheme for $^{61/64}\text{Cu}$ [6]

The ~6 mL dissolved target solution was loaded onto both columns in series, and the nickel target material which remained in the solution was diverted to the designated collection vial for recycling. The TBP resin served to remove trace iron impurities from the solution (oxidized to Fe^{3+} by the H_2O_2), while the TK201 resin trapped the produced copper and cobalt radioisotopes. Both columns were washed with 6 M HCl to maximize the nickel recovery for recycling, again diverted to the designated collection vial. The remaining separation chemistry was performed on the TK201 resin alone. First, the column was rinsed with 4.5 M HCl to elute the cobalt radioisotopic impurities to waste. Then, the column was washed with the 5 M NaCl solution to further remove cobalt radioisotopes, and to decrease the residual acidity on the column. Finally, the copper product was eluted in 2 mL of 0.05 M HCl.

2.2.5) HPGe and MP-AES Analysis

After target irradiation, produced radioactivity was quantified by HPGe spectrometry using an Al-windowed Canberra Model GC1519 (15% relative efficiency, full-width at half-maximum at 1173 keV = 1.8 keV). HPGe spectrometry was also used to determine the radiotracer distribution across the chemistry fractions and collected samples. For ^{61}Cu , the primary gammas used for quantification and analysis were 283 and 656 keV ($I_\gamma = 12.2\%$ and 10.8% , respectively). For ^{58}Co , the primary gamma was 811 keV ($I_\gamma = 99.5\%$). Samples were counted between 1 – 400 cm from the detector face, keeping the detector dead time less than 15%. Energy and efficiency calibration of the detector was performed at these distances using standard laboratory check sources (Amersham): ^{241}Am , ^{133}Ba , ^{137}Cs , ^{152}Eu , and ^{60}Co .

Trace metals analysis was performed using an Agilent Model 4200 microwave plasma atomic emission spectrometer (MP-AES). To do this, 100 μL aliquots from the chemistry fractions were taken and the concentration of HCl in each analyzed sample aliquot was diluted to 0.5 M yielding 1 mL samples for analysis. Calibration standards from 10 ppb to 50 ppm were prepared with Co, Cu, Fe, Ni, and Zn in 0.5 M HCl. Quantification was performed using 2 emission wavelengths for each analyte in solution. Molar activities (MAs) and separation factors (SFs) for the copper product were calculated from the measured results using the standard methods [62,63]:

$$MA = \frac{\text{Activity}_{\text{Cu}}}{n_{\text{Cu}}} \quad , \quad SF = \frac{\left(\frac{C_{\text{Ni},i}}{A_{\text{Cu},i}}\right)}{\left(\frac{C_{\text{Ni},f}}{A_{\text{Cu},f}}\right)}$$

where $\text{Activity}_{\text{Cu}}$ is the amount of $^{61/64}\text{Cu}$ activity present in solution, n_{Cu} is the mass of stable copper in the same solution, $C_{\text{Ni},i}$ is the measured concentration of the stable nickel before the

separation, $A_{Cu,i}$ is the measured activity of $^{61/64}Cu$ before the separation, $C_{Ni,f}$ is the measured concentration of stable nickel after separation, and $A_{Cu,f}$ is the measured activity of the $^{61/64}Cu$ after separation. In cases where the nickel concentration was below the method limit of detection, the lowest concentration from the measured calibration curve (10 ppb) was used, thus these values represent a conservative minimum value; actual MAs and SFs may be higher but obscured by our limited sensitivity during analysis.

2.2.6) AMA and Product Acidity Titrations

Adapting the method of [39], the apparent molar activity (AMA) of the copper product was measured by NOTA titration. 500 μ L of the copper product was diluted to 1.1 mL with 0.25 M NaOAc, and the final solution pH of \sim 4.5 was verified using pH strips. The buffered activity was vortexed, and 100 μ L aliquots were combined with an additional 40 μ L of NaOAc and 100 μ L of NOTA (0.001 – 10 nmol) in centrifuge vials. During 15 minutes of reacting at room temperature, the ^{61}Cu activity in each vial was measured by Capintec. Radio-TLC was performed by spotting from each vial onto the TLC plates, developed in 1:1 MeOH : NH_4OAc (10% w/v) mobile phase. TLC plates were scanned using an OptiQuant autoradiography system (Perkin Elmer Cyclone Plus Storage Phosphor System). From the measured results, sigmoidal curves were generated and used to determine the NOTA mass required for 50% binding. The AMA was then calculated using the average sample activity (decay corrected to EoB) divided by two times the 50% NOTA mass. The final product acidity burden was determined by acid-base titration using phenolphthalein indicator and 5.8 mM NaOH. To accomplish this, 500 μ L final product solution was added to \sim 10 mL of D.I. water with the indicator and a magnetic stir bar in an Erlenmeyer flask and titrated dropwise using a burette until the faint pink color persisted in the solution.

2.3) Results and Discussion

Adaptation of the electroplating method was successful. Plated targets were irradiated, dissolved, and separated using the automated process developed. Target material recycling was successful across 2 rounds of processing, and the final product was found to be suitable for radiolabeling applications. The results below motivate future work to produce a radiolabeled compound using the automated method.

2.3.1) Target Fabrication and Irradiation

The electroplating deposited $96.0 \pm 0.9\%$ ($n = 3$) of the natural enrichment nickel on the silver backings. Recycling of the target material netted 88% and 92% of the nickel, recovered and re-plated in the first and second rounds of recycling, respectively. Representative images of the electrodeposited targets are shown below:

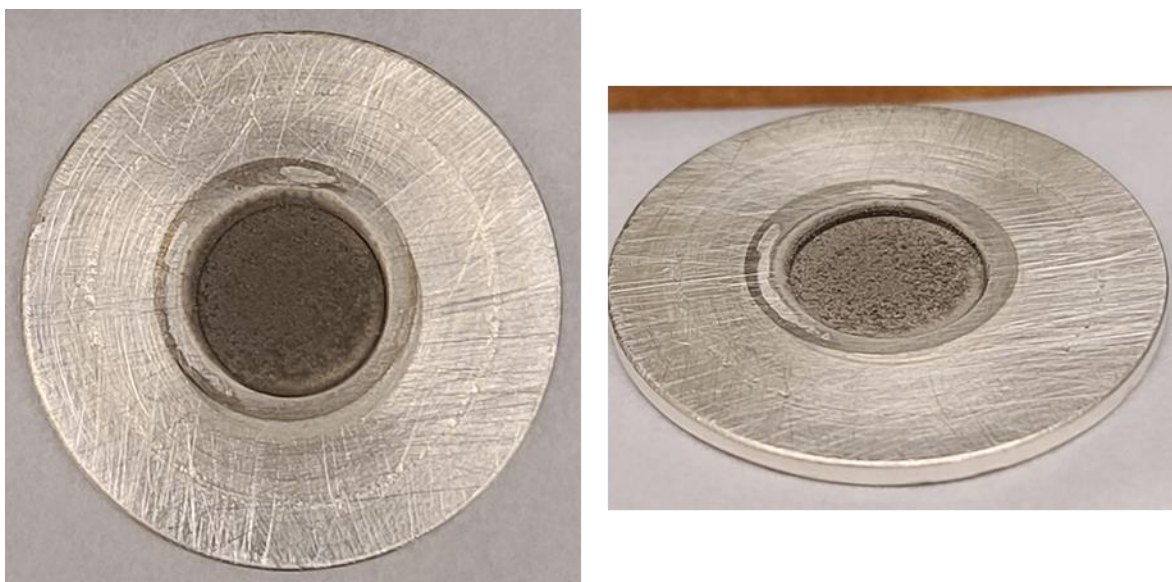


Figure 2: Photos of a representative, electrodeposited nickel target used for production and separation experiments

After irradiation, ^{61}Cu yields were measured by HPGe (section 2.2.5). Activities quantified by HPGe assays of the product, waste, and recovery vials, as well as the resin cartridges and target backing post-dissolution, were summed to determine the yields. From these measurements, the calculated ^{61}Cu saturation yield was 5.6 ± 0.7 mCi/ μA ($n = 3$) for the freshly plated targets irradiated with a low current and used for method optimization, and 5.1 ± 0.9 mCi/ μA ($n = 5$) for the recycled targets. The consistency in yields demonstrated effective recovery of the nickel target material. Due to residual activity in the lines and manifold of the ARTMS QiS dissolution unit and FASTlab chemistry module not being quantified, as well as the fractional intercept of the deuteron beam spot by the plated target (~ 10 mm diameter), the reported yields are conservative.

2.3.2) Irradiated Target Dissolution and Separation

The ARTMS QiS dissolution unit was designed with single-use, disposable fluid paths in the spirit of GMP-compliant kits. The provided fluid paths were not resistant to the concentrated reagents so appropriate tubing material was obtained and installed. Once modified, the activity-based dissolution efficiency was $97.5 \pm 1.4\%$ ($n = 5$). Following dissolution, the target was automatically separated on the FASTlab module. The final product was delivered in 65 ± 3 min ($n = 5$) for application and analysis. ^{58}Co and ^{61}Cu in the separation chemistry fractions were quantified by HPGe (figure 3):

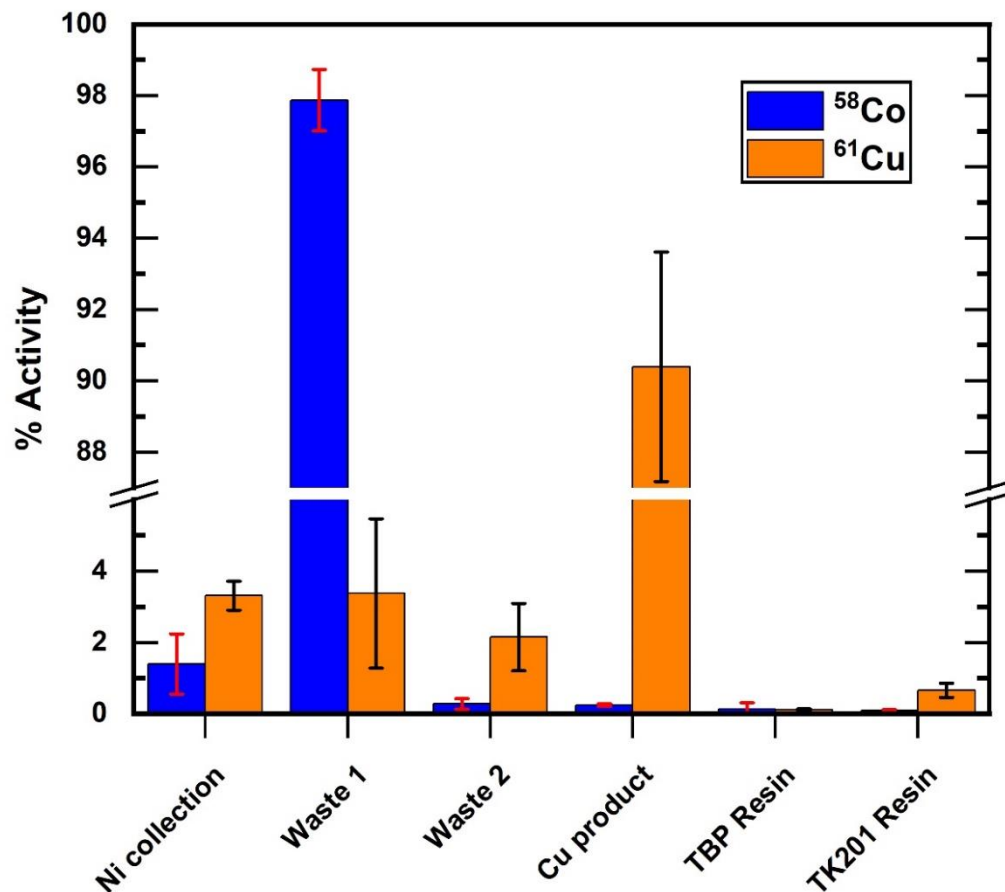


Figure 3: Bar diagram presenting the normalized activity distribution of ^{58}Co and ^{61}Cu . Note that the ^{58}Co and ^{61}Cu have been normalized individually [6]

As intended, $98 \pm 1\%$ ($n = 5$) of the coproduced cobalt radioimpurities were separated from the final product and sent to waste, yielding $90 \pm 3\%$ ($n = 5$) of the ^{61}Cu in the final 2 mL product.

2.3.3) Final Product Characterization

Trace metals analysis of the final product revealed the average copper concentration was 180 ± 40 ng/mL ($n = 5$). The cobalt, zinc, and iron concentrations were all below the limit of detection (100, 100, and 500 ppb, respectively). From the trace metals analysis and HPGe measurements,

MAs, AMAs, and SFs for the ^{61}Cu from the nickel target material were calculated and are tabulated below:

| | ^{61}Cu Short irradiations (0.5 h) n = 5 | ^{61}Cu Long irradiation (3.3 h) n = 1 | ^{64}Cu Test irradiation (1 h) n = 1 |
|--|--|--|--|
| MA (Ci/ μmol) | 2.31 ± 0.62^a | Not measured | Not measured |
| NOTA AMA (Ci/ μmol) | 0.85 ± 0.22^a | 5.43^a | 4.8^a |
| Ni separation factors | $\geq (2.2 \pm 1.8) \times 10^6$ | - | - |

^a at EoB

Table 2: Compilation of product MAs, AMAs and nickel SFs for short and long irradiations [6].

These results are encouraging, and the MA is expected to increase with longer irradiations (as the amount of stable copper in the target material should not change significantly). If similar stable copper mass were present during the long irradiation the expected MA would be about 13 Ci/ μmol (n = 1); this was not measured directly, however. Further, assuming similar levels of impurities in the natural enrichment nickel and enriched ^{60}Ni , the MA would increase approximately 4-fold. In such targets, MAs approaching 50 Ci/ μmol are not unrealistic and may be even higher with proton irradiation of ^{61}Ni . The theoretical maximum MA for ^{61}Cu is about 940 Ci/ μmol . High MAs are desirable but do not guarantee the final product is suitable for radiolabeling applications as other contaminants present may compete with the ^{61}Cu for the chelator.

Another metric describes the purity of the final product in this light, the AMA, which was measured for the final product by titration with NOTA. Still, the AMA depends on the chelator and labeling conditions employed, so a direct comparison of the AMA between different

experimental conditions is not straightforward [6]. The NOTA AMA for ^{61}Cu from the long irradiation was $\sim 5.4 \text{ Ci}/\mu\text{mol}$. From the proof-of-concept ^{64}Cu production, the NOTA AMA was $4.8 \text{ Ci}/\mu\text{mol}$ and is in reasonable agreement with the productions using natural enrichment targets. The radiochemical yield of ^{64}Cu was 93% after 65 minutes of total processing time, and the ^{64}Ni recycling efficiency was 95%, on par with the natural enrichment target recycling results obtained in this work.

While the final product was eluted from the resin column using 0.05 M HCl, residual acidity on the resin column can increase the molarity of the eluent. For this reason, the final product HCl concentration was titrated and found to be $0.057 \pm 0.002 \text{ M}$ ($n = 5$). Such dilute acidic conditions should enable downstream radiolabeling without additional buffering. Considering this, future work is planned to explore cassette-based radiolabeling to yield a radiotracer product suitable for direct application. Finally, the European Pharmacopoeia 2020 states a radionuclidic impurity limit of 0.1% by activity for direct accelerator-produced ^{68}Ga [6]. Applying this same criterion to the final product from this work and considering the $(8.3 \pm 0.6) \times 10^{-5}\%$ ($n = 5$) ^{58}Co present in the eluate at end-of-chemistry (EoC), the ^{61}Cu product is acceptable to this standard.

2.4) Conclusions

In conclusion, the automated method developed and implemented at our facility produced high purity $^{61/64}\text{Cu}$ from natural and enriched, electrodeposited nickel targets. The final product is delivered in 2 mL of dilute ($< 0.06 \text{ M}$) HCl in approximately 65 minutes from EoB to EoC. The average radiochemical yield was 94%, with NOTA AMAs $> 5 \text{ Ci}/\mu\text{mol}$ for 30 μA irradiations of 3.3 hours. The SF for the nickel target material from the final product was $> 2 \times 10^6$. The cobalt

radionuclidic impurities in the final product amounted to $< 0.0001\%$ at EoC. The developed method is suitable for ^{64}Cu production from enriched targets (demonstrated by the proof-of-concept run). The single-use, cassette-based method is repeatable and facile to incorporate into a GMP environment, with radiochemical yield and HCl concentration standard deviations of 3.2% and 3.6% ($n = 5$), respectively. The FASTlab module is equipped to perform radiolabeling reactions online and will be the subject of future investigations.

Chapter 3: Gallium-based Targetry for Cyclotron/Accelerator Production of Radiogermanium

3.1) Background summary and hypothesis

With recent FDA approval of many ^{68}Ga -based radiotracers for clinical application, there is high demand for ^{68}Ge ($T_{1/2} = 270.95$ d, 100% ϵ) as the parent radionuclide in $^{68}\text{Ge}/^{68}\text{Ga}$ generators [4,9,64]. Because of this important relationship, the production of germanium radioisotopes focuses almost exclusively on ^{68}Ge production, usually by medium-energy proton irradiation of niobium encapsulated gallium metal [65–70]. Data from [32] is presented in figure 4 (below) for natural gallium and relevant isotopes of germanium:

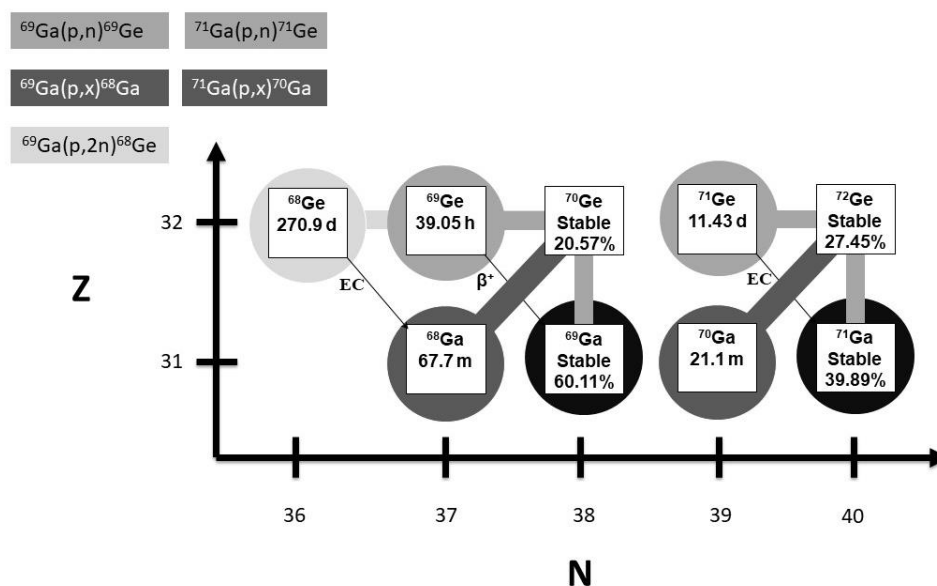


Figure 4: The relevant isotopes of gallium and germanium and the nuclear reactions of interest for proton bombardment of natural enrichment gallium targets.

In addition to ^{68}Ge production, the combination of positron-emitting ^{69}Ge ($T_{1/2} = 39.05$ h, $I_{\beta^+} \approx 25\%$, $E_{\beta^+ \text{avg}} = 522.1$ keV) and Auger-electron-emitting ^{71}Ge ($T_{1/2} = 11.4$ d, 100% ϵ) potentially

presents a theranostic pair of radionuclides and merits further investigation. For investigation of the potential theranostic pair, it is possible to maximize $^{69/71}\text{Ge}$ production while minimizing ^{68}Ge coproduction through the proper selection of incident proton energy (visually evident ~ 12 MeV in the cross-section figure below):

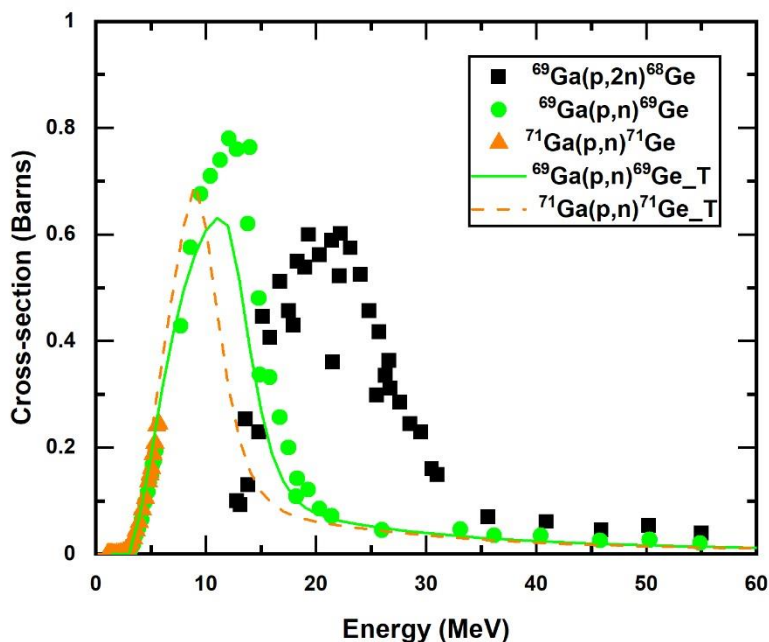


Figure 5: Cross-section data for expected nuclear reactions in natural enrichment gallium targets: black squares [71,72], green circles [71–74], and orange triangles [75,76] are experimentally measured, while the solid green and dashed orange lines are theoretical predictions [77]

The $^{69}\text{Ga}(p,n)^{69}\text{Ge}$ and $^{71}\text{Ga}(p,n)^{71}\text{Ge}$ nuclear reactions ($E_{\text{threshold}} = 3.1$ and 1.0 MeV, respectively) produce the germanium radionuclides of interest. ^{68}Ge coproduction from the $p,2n$ nuclear reaction on ^{69}Ga ($E_{\text{threshold}} = 11.4$ MeV) is undesirable in the context of this work. To produce mainly $^{69/71}\text{Ge}$, with the threshold for the ^{68}Ge reaction at 11.4 MeV, irradiation with protons of

approximately 12 MeV is desired to capitalize on the peak of the cross-section for the ^{69}Ge reaction. For incident protons of this energy, the theoretical TTY in natural gallium at EoB is calculated according to the formalism recommended by the IAEA [30], presented in chapter 1. The stopping power is obtained from SRIM [31] and in addition to calculating the yields is also used to determine the thickness of a target required to fully stop the proton beam. For natural gallium, the TTY for ^{69}Ge is approximately 1.4 mCi/ μAh with a thickness of 420 μm [28].

The primary drawback to niobium encapsulated gallium metal targets is the potential for rupture of the encapsulation and subsequent loss of target material and radioactive product. Additionally, molten gallium is a danger to many of the structural and mechanical components of the accelerator because of gallium's reactivity with commonly used metals (especially aluminum). As an improvement on encapsulated gallium metal targets, alloy targets of nickel and gallium have been investigated for $^{68/69}\text{Ge}$ production [28,78]. This combination prevents the formation of molten gallium during irradiation and obviates the gallium attack hazard. These targets tolerate 30-45 μA of proton beam without melting and contain 75% of the target atoms (NiGa_3) compared to elemental gallium, thus affording comparable yields of germanium radioisotopes. However, the inclusion of natural, polyisotopic nickel presents a different challenge with the coproduction of several short and intermediate-lived radioisotopes of copper and several long-lived isotopes of cobalt from proton reactions with the nickel. The data from [32] for stable isotopes of natural nickel and the various copper and cobalt radioisotopes coproduced in this way are presented in figure 6:

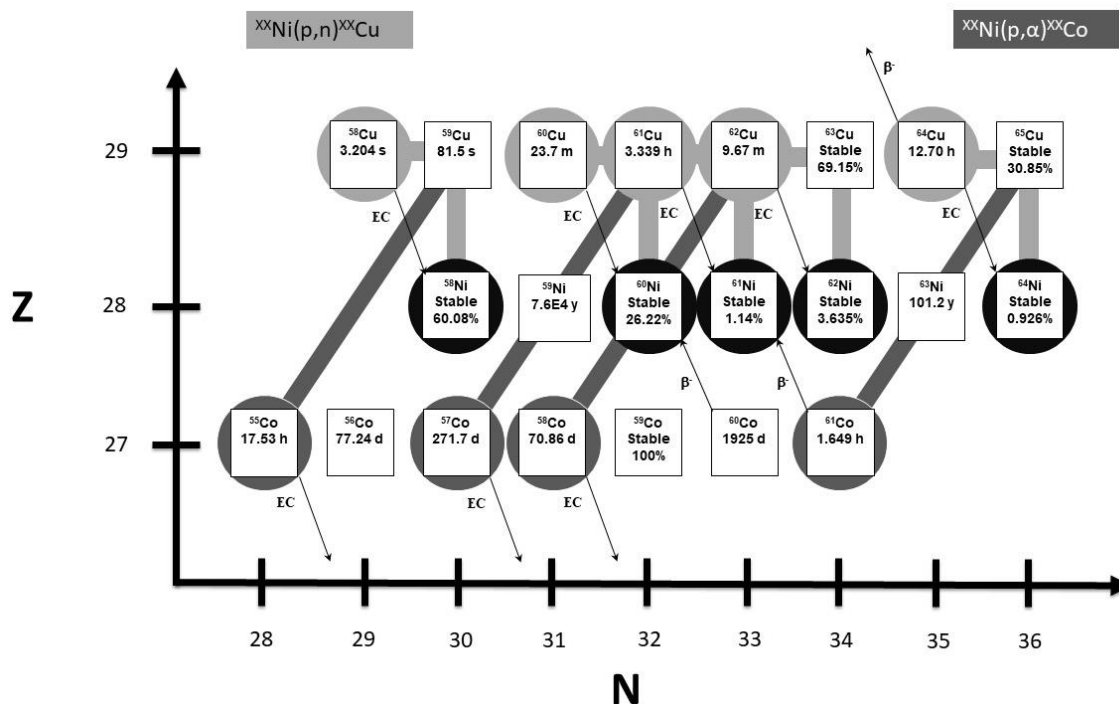


Figure 6: Stable isotopes of natural nickel and relevant copper and cobalt radioisotopes produced during proton irradiation.

Because of the additional radioisotopes produced in the nickel-gallium targets a cooling down period of at least 1 day is necessary before these targets can be safely handled and processed [28,78]. Furthermore, when these targets are prepared by electrodeposition the thickness and mass of target material that can be deposited are limited and the preparation of thick targets can take up to 12 days to complete. The theoretical TTY for ^{69}Ge in these targets is ~ 1 mCi/ μAh for 11 MeV proton bombardment [28].

Inspired by the Ni-Ga approach [28,78] and by recent work on the high-temperature fusion (HTF) of cobalt with selenium [79], we chose to investigate intermetallic compounds of cobalt and gallium. We hypothesized that this combination could overcome the challenges associated with existing target materials without compromising $^{69/71}\text{Ge}$ yield. Data from [32] for the stable

isotope of cobalt and various radioisotopes coproduced during proton irradiation are presented in figure 7:

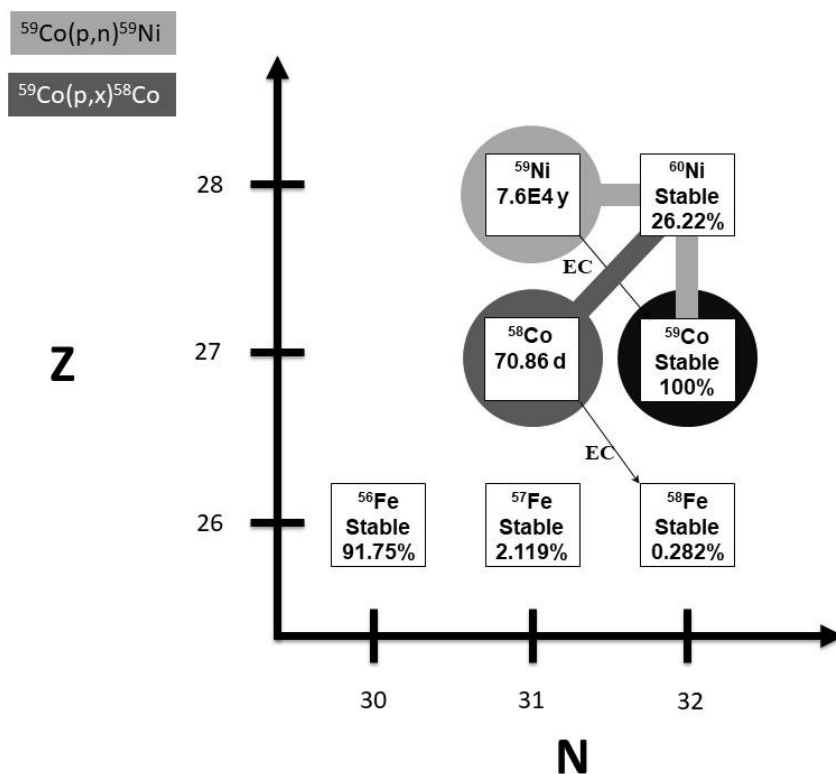


Figure 7: Reaction pathways to nickel and cobalt radioisotopes from proton irradiation of cobalt.

The cobalt-gallium target constituents are cheap, commercially available products, and in their natural enrichment enable simultaneous production of ^{69}Ge and ^{71}Ge with minimal radioisotopic impurities; yields of $^{69/71}\text{Ge}$ in these targets are expected to be high. The primary activity in such targets immediately after production is ^{69}Ge , useful for diagnostic imaging. By contrast, after a decay period of 21 days, the ^{69}Ge would have decayed by a factor of >8000 while ^{71}Ge would

have undergone less than 2 half-lives. This reversal yields primarily ^{71}Ge for other nuclear medicine applications.

3.2) Materials and Methods

Cobalt powder (1.9-micron, 99.8% metals basis) and gallium pellets (6 mm diameter, 99.9999% metals basis) were purchased from Alfa Aesar. Quartz glass tubing (10 mm inner diameter [ID] x 12 mm outer diameter [OD]) was purchased from QSI Scientific. Niobium and boron nitride rod stock (19 mm OD) were purchased from Grainger.

3.2.1) Target Fabrication

The phase diagram (figure 8) for the cobalt-gallium binary system [80] was used to identify known alloys and combinations possible:

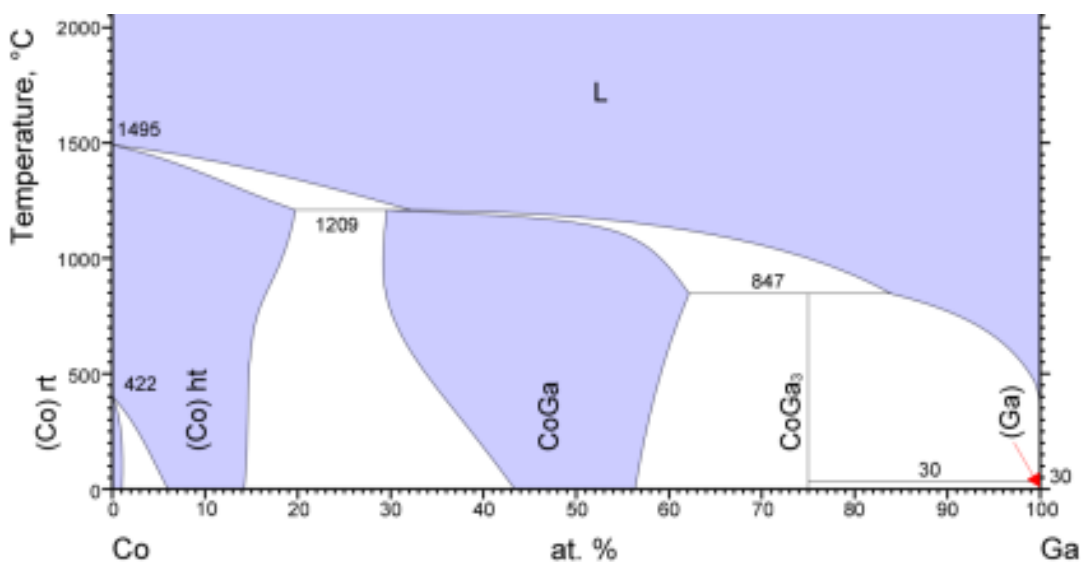


Figure 8: Thermodynamic model of the Co-Ga system plotted as atom percent of gallium (horizontal axis) versus temperature in Celsius (vertical axis).

Seeking a high gallium content and a high melting temperature, we identified atom ratio (AR) combinations of cobalt to gallium 1:1 through 1:4 with expected melting temperatures of 847 °C and above [80]. Pellets comprised of these ratios were formed for the investigation. As introduced, the target material was formed through HTF of cobalt and gallium (under a low pressure of Argon gas in quartz glass ampoules) using the method adapted from [79]. Cobalt and gallium of natural isotopic composition were weighed into 10 x 12 mm (ID x OD) round-bottom quartz tubes. The round-bottom tubes were coupled to a gas-tight rig. A vacuum pump evacuated the rig, which was backfilled with Argon gas and evacuated again. Finally, the tubes were sealed into ampoules using an oxypropane torch. The sealed ampoules were placed in a Thermolyne Model 10500 furnace and heated (1100 °C for AR 1:2, 1050 °C for AR 1:3, and 950 °C for AR 1:4) for approximately 2 hours. The heated ampoules were rapidly quenched in a room temperature water bath, breached, and the formed pellets weighed. Some pellets were ball-milled using a benchtop laboratory mill (Spex CertiPrep 8000M) with stainless steel ball bearings, reducing formed pellets to grains for reforging.

Some milled and unmilled pellets were hot-pressed into niobium crucibles using previously described methods [79]. A sample pellet was centered in the pocket of a niobium crucible (19 mm diameter, 2 mm thick niobium coin with a centered, 9.5 mm diameter, 1 mm deep pocket) at the bottom of a 20 x 22 mm (ID x OD) flat-bottom quartz tube. A boron nitride tamp was placed on top of the pellet and held in place by a bell-ended quartz tube. The assembly was sealed, flushed with argon gas, and lowered into the pre-heated, vertical tube furnace. The furnace temperature settings were the same as those used during forming. The pellets were malleable after ~5 min in the furnace, and the quartz outlet tube was depressed manually to compact the

sample into the crucible pocket. The assembly was removed from the furnace and quenched in a water bath. The masses of the empty and hot-pressed crucibles were recorded.

Following this procedure, two general types of targets were fabricated for irradiation. Energetically “thick” targets weighing ~ 460 mg and filling the entire 1 mm deep crucible pocket were sufficient to stop the incident proton beam [31]. Energetically “thin” targets, weighing ~ 185 mg and filling the crucible pocket ~ 400 μm , with a proton exit energy of 3 – 4 MeV (AR 1:2 – 1:4, respectively).

3.2.2) Irradiation Configuration and Parameters

To study radioactivity yield and the material’s durability in beam, Co-Ga targets were irradiated on a GE PETtrace cyclotron for 10 – 120 min with 5 – 50 μA of protons and water jet cooling on the back of the target. A 250 μm thick niobium foil was mounted in contact with the front of the target to degrade the 16 MeV proton beam to approximately 12 MeV. The degraded beam energy minimized ^{68}Ge coproduction from the $p,2n$ nuclear reaction on ^{69}Ga as desired. The configuration is depicted below (figure 9):

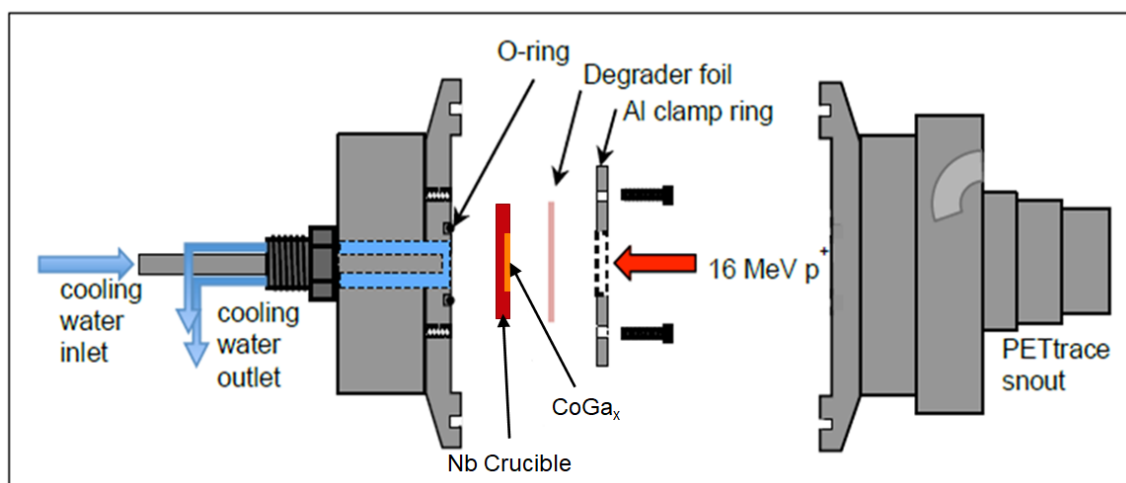


Figure 9: Target irradiation configuration on the GE PETtrace solid target port

Targets were sometimes allowed to decay overnight to reduce the dose hazard from the ^{93}Mo produced in the niobium from the p,n reaction.

3.2.3) HPGe and CdTe Spectrometry

HPGe gamma spectrometry was performed as described in 2.2.5. The ^{69}Ge Y_{EOB} was measured from the thick, irradiated targets 400 cm from the detector face after decay to detector dead times <7.5%. The ^{58}Co ($T_{1/2} = 70.9$ d, 100% ϵ) Y_{EOB} was measured from 100 μL aliquots of the dissolved targets approximately 1 cm from the detector face after >10 half-lives of ^{69}Ge .

CdTe X-ray spectrometry with a 100 μm thick Be-windowed Amptek Model X-123 (5x5x1 mm³, FWHM at 59.54 keV = 0.83 keV) quantified ^{71}Ge directly. The instrument was calibrated for efficiency from 5 – 60 keV using an ^{241}Am ($T_{1/2} = 432.6$ y, 100% α) check source and HPGe-cross-calibrated sources of ^{64}Cu ($T_{1/2} = 12.701$ h, 61.5% ϵ , 38.5% β^-) and ^{68}Ga ($T_{1/2} = 67.71$ m, 100% ϵ) spotted onto glass slides in the sample measurement geometry. Dissolved target and $^{69/71}\text{Ge}$ product aliquots were spotted in 2 μL drops onto glass slides and dried using a heat gun before CdTe assay. The HPGe-quantified ^{69}Ge activity on each slide was normalized to the ^{69}Ge activity measured in the Co-Ga target post-irradiation. This scaling factor was used to calculate the ^{71}Ge produced in the target from the ^{71}Ge activity measured on the slide via CdTe spectrometry after a 21-day decay period.

3.3) Results and Discussion

The current standard target for germanium radioisotope production (primarily ^{68}Ge for ^{68}Ga radionuclide generators) uses niobium to encapsulate gallium metal. Elemental gallium melts at

~30 °C, and molten gallium easily dissolves most metals commonly found in accelerator infrastructure (i.e. aluminum). These properties make gallium a problematic accelerator target material, challenging to contain during irradiation [81]. To overcome this challenge without encapsulation, an alloy of Ni + Ga has been investigated for germanium radioisotope production [28,78]. These targets can prevent the formation of molten gallium and subsequent attack, but the inclusion of natural, polyisotopic nickel in the target material leads to coproduced radioisotopic impurities from the nickel activation. Because of this, Ni-Ga targets require a decay period of at least 1 day before handling, and the remaining impurities must be separated during radiochemical isolation [28,78]. The results from the experiments with Co-Ga targets that follow are encouraging that this combination can overcome challenges associated with conventional gallium-based targetry.

3.3.1) Target Fabrication

The HTF method produced pellets of the CoGa_x material from chunks of gallium metal and cobalt powder (figure 10):

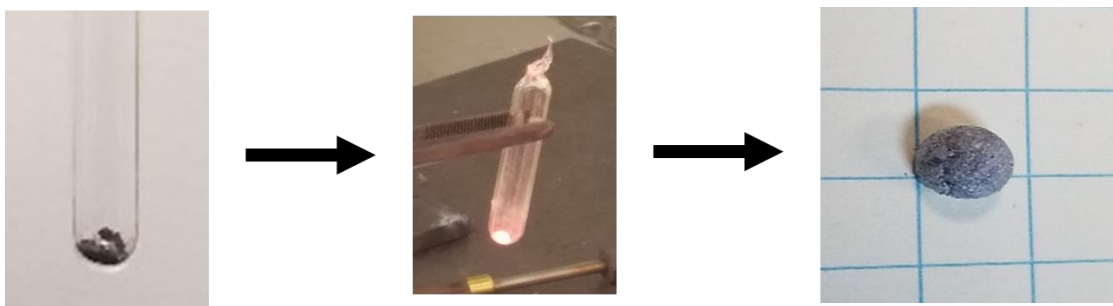


Figure 10: CoGa_x pellet (**right**) formed by HTF of elemental cobalt and gallium (**left**)

Pellets formed this way had a rough outer surface, occasionally cracked, with a dull gray luster, and were brittle like ceramic, crumbling under applied pressure. Ball milling and reforging did not

improve the visible appearance or brittleness of the material. Mass losses of cobalt and gallium during target synthesis (forging, hot pressing, and milling) were tolerable, especially given the low cost of these materials. The average mass loss of Co-Ga was $5.4 \pm 5.5\%$ ($n = 54$) during pellet forging and $2.6 \pm 3.4\%$ ($n = 31$) during hot-pressing. For previously milled pellets, the average mass loss was $4.1 \pm 5.0\%$ ($n = 41$) during pellet forging and $3.0 \pm 2.9\%$ ($n = 16$) during hot-pressing. Additionally, $4.6 \pm 4.7\%$ ($n = 7$) mass was lost to the ball mill during milling. XRD results from unmilled and milled AR 1:3 targets showed predominantly characteristic signal from CoGa_3 (Figure 11):

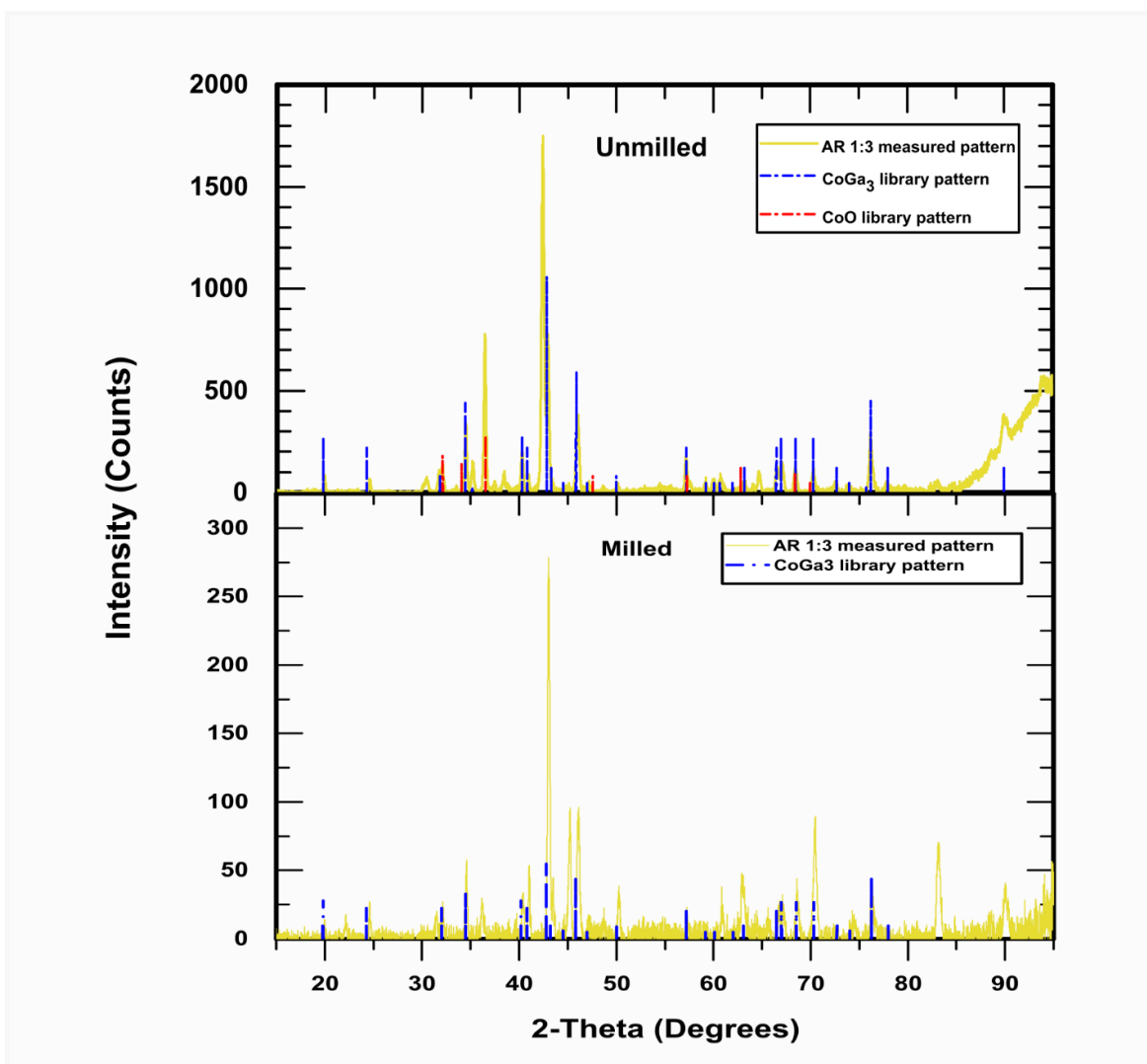


Figure 11: Measured X-ray diffraction patterns for **upper**) unmilled AR 1:3 Co:Ga sample & **lower**) milled AR 1:3 Co:Ga sample shown in gold with analysis software library matches shown in blue and red.

The measured diffraction patterns match well with library patterns in angle and intensity for the samples. Peaks associated with cobalt oxide (CoO) were observed in the unmilled target material, as well as a few unexplained peaks likely due to trace contaminants but were unable to be identified. Additional XRD data from the other AR target types is shown in Appendix A. The multiple chemical species present in the unmilled XRD data are indicative of a lack of homogeneity in the target material.

The final step in target fabrication was hot-pressing the formed pellets into the niobium crucibles (section 3.2.1) using our in-house rig built for hot-pressing the targets (figure 12):



Figure 12: The hot-pressing rig with niobium crucible, CoGa_x pellet, boron nitride tamper, and bell-ended quartz glass rod for pressing and gas flow egress (bottom to top)

AR 1:1 pellets cannot be hot-pressed using this setup. Pellets of this type have an expected melting temperature above $1200\text{ }^\circ\text{C}$, as evident from the phase diagram (figure 8). The vertical tube furnace used in this work was only able to achieve a steady-state temperature of $\sim 1100\text{ }^\circ\text{C}$ at the sample stage (measured by an external thermal probe). Even after 5-10 minutes in the

furnace at this temperature the AR 1:1 pellets were not malleable. Because of this, AR 1:1 was rejected as a suitable target material candidate. For the other ARs, the average change in mass from the hot-pressing was $-2.6 \pm 3.4\%$ ($n = 31$) for unmilled and $-3.0 \pm 2.9\%$ ($n = 16$) for the milled targets, respectively. Representative pressed-target photos show the filling of the niobium crucible target with the CoGa_x material (figure 13):



Figure 13: A thick (~ 460 mg, **left**) and a thin (~ 185 mg, **right**), unmilled CoGa_2 target after hot-pressing into the niobium crucible.

Thick targets filled the entire crucible pocket and were partially in contact with the containment foil during irradiation. Thin targets were recessed farther from the containment foil. However, filling the crucible pocket with a uniform layer of the pressed pellet was challenging using this setup (figure 13, right).

3.3.2) Irradiated Target Performance

An incremental approach was employed to probe the beam current tolerated by the targets to minimize the danger to the cyclotron from molten gallium formation. Initially, targets were irradiated with $5\ \mu\text{A}$ of protons for 30 minutes. The target's tolerance was assessed from the

change in target mass pre- and post-irradiation, the physical appearance of the target material, and containment foil, and any adherence of the target material to the containment foil or breach/failure of the containment foil post-irradiation. Unmelted targets had a negligible change in mass pre- and post-irradiation (less than 1%) and no visible change in appearance or adherence to the containment foil. Targets considered unmelted motivated increased proton current application to subsequent targets of the same type. This incremental process was repeated until melting was observed. Melted targets lost nearly all their mass onto the containment foil, with some gallium residue evident on the aluminum retainer ring. In the case of failed/melted targets, some germanium radioactivity was recovered by nitric acid etching of the foil and crucible residues for subsequent experimentation.

The effect on beam power tolerance due to target AR composition and reforging was investigated. Three high-level results are apparent: first, milling appears to increase tolerated beam intensity but is incompatible with AR 1:4 Co:Ga. Second, both milled and unmilled AR 1:3 Co:Ga tolerated higher beam intensity. Finally, depositing the final 3 – 4 MeV of proton energy in the niobium crucible substantially improves target durability without decreasing the yields appreciably (Figure 14, below):

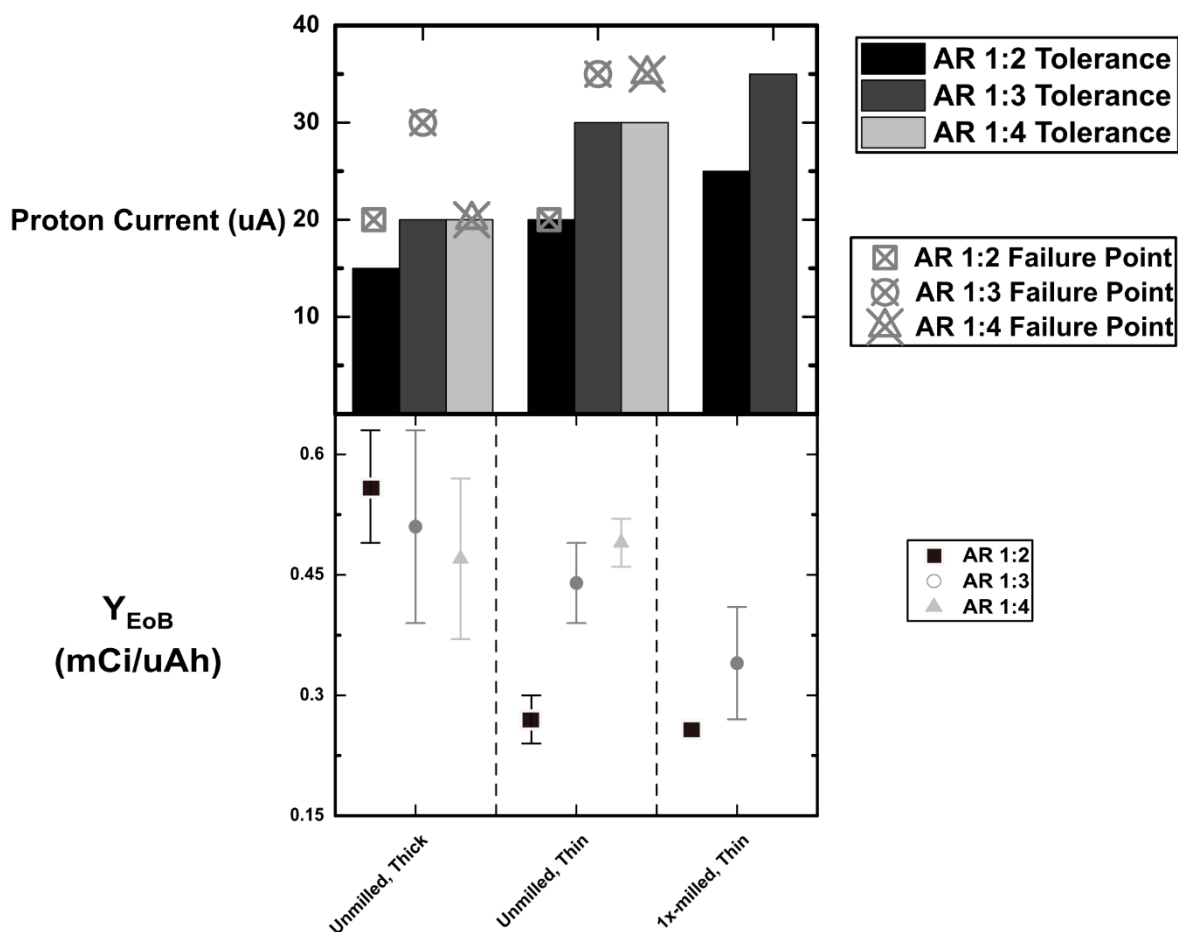


Figure 14: **upper**) Proton current applied (vertical axis) for the various AR and target types investigated. Failure points are plotted with the red symbols for each AR. **lower**) ^{69}Ge End-of-bombardment physical yields (vertical axis) for AR 1:2 – 1:4 targets.

Thick, unmilled targets performed worst overall. The AR 1:2 targets tolerated 15 μA of proton current for 120 min ($n = 2$). At 20 μA , one of two targets melted in less than 60 min of irradiation. For the AR 1:3 targets, the maximum proton current tolerated was 20 μA for 30 min ($n = 2$), though melting and interaction with the containment foil occurred with proton currents of 30 μA for 30 min ($n = 1$). For the 1:4 AR targets, the maximum tolerated current was 20 μA delivered for 60 min ($n = 4$), while 1 such target did melt. In the irradiated configuration, the niobium

containment foil faced the vacuum and was poorly cooled. For this reason, the foil reached elevated temperatures and was believed to be the primary cause of target melting during bombardment. Melting of the target on the side facing the containment foil was visibly evident in those cases, as was residue on the foil. Some melted targets breached the foil containment and mass loss occurred.

To probe whether the proximity to the containment foil caused the melting, thinner Co-Ga targets were produced to fill the niobium crucible less and avoid direct thermal contact with the containment foil (figures 9 and 13). Thin target (proton exit energy ~ 3 MeV) results were decidedly more encouraging. Unmilled, thin AR 1:2 targets survived 20 μA for up to 60 min ($n = 4$), while 1 such target did melt. AR 1:3 ($n = 3$) and 1:4 ($n = 2$) targets survived 30 μA for up to 45 min. Melting did not occur until 35 μA for AR 1:3 & 1:4 ($n = 1$, each). Despite this improvement, target inhomogeneity was suspected as a cause of melting. During fabrication, as Co-Ga intermetallic targets were cooled from above their liquidus temperatures (1090 $^{\circ}\text{C}$ for AR 1:2, 1000 $^{\circ}\text{C}$ for 1:3, 940 $^{\circ}\text{C}$ for 1:4) they passed through a mixed liquid/solid phase and partitioned into multiple phases, including CoGa, CoGa₃, and elemental gallium upon solidification below the solidus temperature (847 $^{\circ}\text{C}$ for all). The AR 1:2 targets were fabricated at a higher temperature and therefore spent more time in this mixed phase, likely resulting in greater heterogeneity, which we suspect was impacting their thermal durability. New batches of targets were sequentially milled, reformed, and tested in beam. Unfortunately, AR 1:4 Co:Ga does not tolerate milling. The high gallium content causes the pellets to elastically deform (instead of fragmenting) inside the ball mill, coating equipment with chunks of soft material. As a result, milling experiments were restricted to ARs 1:2 and 1:3 Co:Ga.

Thin, milled AR 1:2 targets tolerated 25 μA for up to 45 min ($n = 6$), nearly double the tolerance for thick, unmilled targets of the same type. Thin, milled AR 1:3 targets showed the greatest promise, tolerating 35 μA for up to 30 min ($n = 3$). A single, thin, unmilled AR 1:3 target tolerated 50 μA for 10 min without melting, and the beam current tolerance for these targets continues to be investigated. These results suggest that one round of milling is sufficient to improve the target durability without appreciably increasing target fabrication time or loss of radioactivity yield.

The physical TTY at EoB (TTY_{EoB}) [82] of ^{69}Ge was measured as described in section 3.2.3 for each of the ARs, and the results are tabulated below (Table 3):

| Target Atom Ratio | ^{69}Ge Physical Yield (mCi/ μAh @ EoB) | Corrected Yield (mCi/ μAh @ EoB) | Calculated TTY (mCi/ μAh @ EoB) | % of TTY |
|-------------------|---|---|--|----------|
| 1:2 | 0.56 ± 0.07 ($n = 3$) | 0.90 ± 0.1 | 1.2 | 75 |
| 1:3 | 0.54 ± 0.11 ($n = 10$) | 0.90 ± 0.2 | 1.3 | 69 |
| 1:4 | 0.47 ± 0.10 ($n = 6$) | 0.8 ± 0.2 | 1.4 | 57 |

Table 3: Measured physical TTY_{EoB} for ARs 1:2 – 1:4, the values corrected for the fractional beam spot intercept, the calculated TTY_{EoB} , and the percent of theoretical values achieved.

The measured values were lower than expected (30-50% of the theoretical values). Some of the departure of the measured physical yields from the theoretical predictions is attributed to the mismatch between the beam spot size and the Co-Ga targets. Previous reports using this PETtrace cyclotron measured the target intercept of the proton beam and found this to be $\sim 60\%$ [12,79,83–85]. This factor of ~ 2 from the fractional beam intercept explains much of the departure between the calculated and measured physical yields. The remaining discrepancy is

likely due to inhomogeneity in the formed target material. The TTYs were calculated using the experimental cross-section data available for ^{69}Ge (Figure 5).

For the thin Co-Ga targets, experimental EoB yields were measured from the dissolved target activity for milled and unmilled targets. The measured thin target yields are tabulated with the measured TTYs for comparison:

| Target Atom Ratio | Target Type | Target Milled? | ^{69}Ge Physical Y_{EoB} (mCi/ μAh) |
|-------------------|-----------------|----------------|---|
| 1::2 | Thick (~460 mg) | No | 0.56 ± 0.07 (n = 3) |
| | Thin (~185 mg) | No | 0.27 ± 0.03 (n = 6) |
| | | Once | 0.26 (n = 1) |
| | | Twice | 0.31 ± 0.07 (n = 3) |
| | | Thrice | 0.29 ± 0.09 (n = 3) |
| 1::3 | Thick (~460 mg) | No | 0.51 ± 0.12 (n = 6) |
| | Thin (~185 mg) | No | 0.44 ± 0.05 (n = 3) |
| | | Once | 0.34 ± 0.07 (n = 2) |
| | | Twice | 0.33 ± 0.05 (n = 2) |
| | | Thrice | 0.49 ± 0.05 (n = 3) |
| 1::4 | Thick (~460 mg) | No | 0.47 ± 0.10 (n = 6) |
| | Thin (~185 mg) | No | 0.49 ± 0.03 (n = 3) |
| | | Once | N/A |
| | | Twice | N/A |
| | | Thrice | N/A |

Table 4: Experimentally measured ^{69}Ge Y_{EoB} for the various target types investigated

Unmilled and milled thin Co-Ga targets yielded ~ 0.3 mCi/ μAh of ^{69}Ge , consistent across successive milling and refoing, suggesting that minimal gallium was lost during the entire target fabrication process. As expected, thin target ^{69}Ge yields trended upwards with AR (due to increasing gallium content in the target material).

A set of thick unmilled AR 1:3 targets was irradiated, then dissolved and separated following the devised method (chapter 4). From these targets, samples from the dissolved target solution and

eluted $^{69/71}\text{Ge}$ product were prepared for analysis on the CdTe X-ray detector as described in section 3.2.3. The physical TTY_{EoB} of ^{71}Ge was $20 \pm 3 \mu\text{Ci}/\mu\text{Ah}$ ($n = 3$). Applying the same beam spot correction as above, the corrected, physical TTY_{EoB} of ^{71}Ge is $40 \mu\text{Ci}/\mu\text{Ah}$. The theoretical TTY for the ^{71}Ge , estimated from theoretical cross-section data obtained from the TALYS simulation code [86], was approximately $140 \mu\text{Ci}/\mu\text{Ah}$. The actual cross-section values for the $^{71}\text{Ga}(p,n)^{71}\text{Ge}$ nuclear reaction are not available from the literature above 7 MeV, and the theoretical data obtained from TALYS may overestimate the height of the peak in the cross-section (figure 5), leading to an overprediction in the TTY. This may help to explain the discrepancy between our measured value and the predicted TTY.

Analysis of the irradiated targets by HPGe also revealed $^{93\text{m}}\text{Mo}$ and ^{92}Nb in the niobium crucible and containment foil, but neither were detected in any dissolved target or radiochemistry samples. Measurements taken after 10 half-lives of ^{69}Ge confirmed the presence and coproduction of small amounts of ^{58}Co in the target from the $^{59}\text{Co}(p,pn)$ and $^{59}\text{Co}(p,d)$ nuclear reactions ($E_{\text{threshold}} = 10.6$ and 8.4 MeV, respectively). The corrected, physical TTY_{EoB} for ^{58}Co in thin milled CoGa_3 targets was $3 \pm 1 \text{ nCi}/\mu\text{Ah}$ ($n = 3$). The theoretical TTY for ^{58}Co in CoGa_3 targets was $2.5 \text{ nCi}/\mu\text{Ah}$. Even thin CoGa_3 targets (degrading the proton energy to ~ 3.3 MeV upon exiting the target) were sufficiently thick to the $^{59}\text{Co}(p,x)^{58}\text{Co}$ reactions, so the measured physical yield is in good agreement with the theoretical prediction.

As described in section 3.2.3, the CdTe detector was calibrated for efficiency across 5 – 60 keV at ~ 2 cm from the detector face adapting reported methods [87–89]. The measured absolute efficiencies (figure 15) were used to quantify the ^{71}Ge activity from the low energy x-ray emissions:

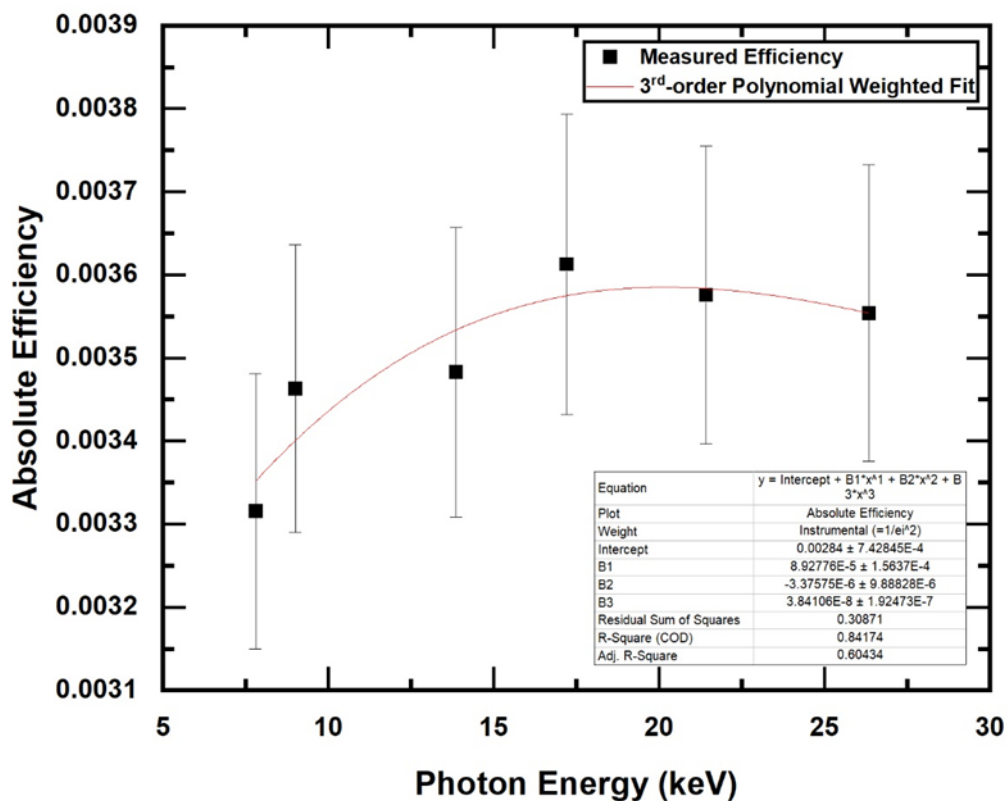


Figure 15: Absolute efficiency measured for CdTe detector ~ 2 cm from detector face versus incident photon energy in keV. The 7.5 – 8.3 keV X-rays from ^{64}Cu and 8.6 – 9.6 keV X-rays from ^{68}Ga were used with intensities tabulated by [32] to calculate detector efficiency. The ~ 14 – 26 keV X-rays from ^{241}Am were used with intensities reported by [90].

^{71}Ge activity was quantified using these results. A representative spectrum obtained from a stippled ^{71}Ge source is shown here:

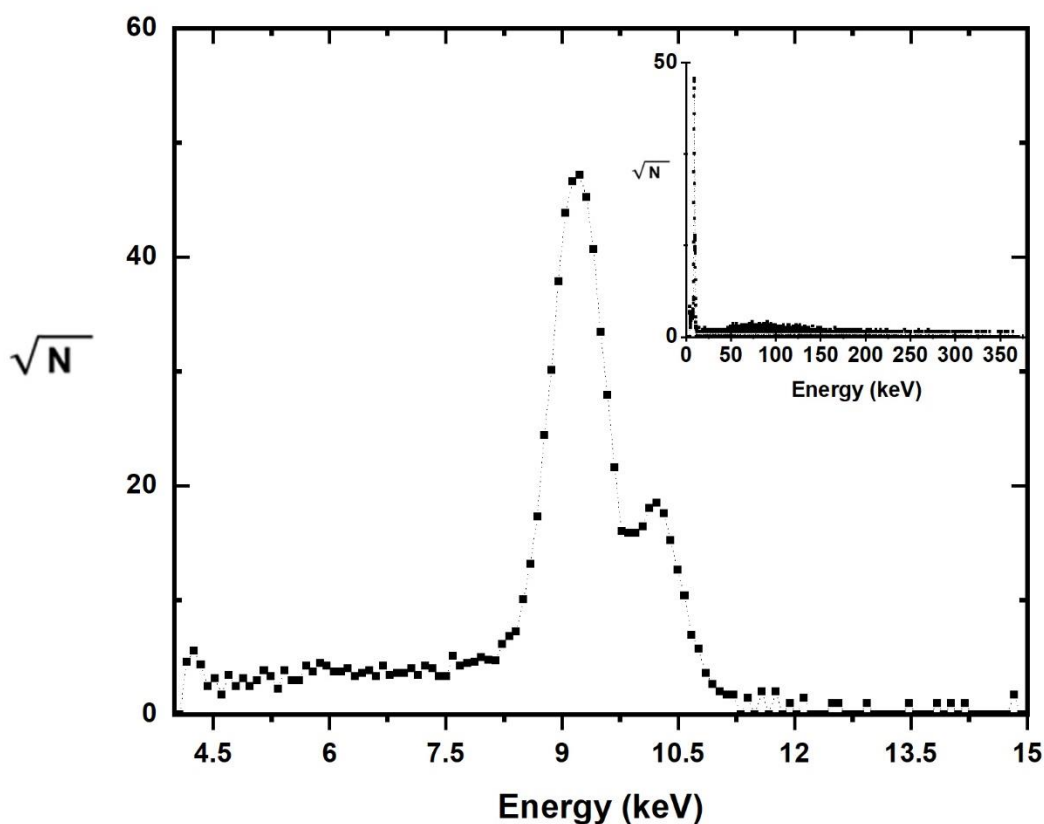


Figure 16: Measured X-ray spectrum from ^{71}Ge stippled sample.

The ~ 9.2 and 10.3 keV X-rays (9.225 keV [13.3%], 9.252 keV [26.1%], 10.26 keV [1.66%], and 10.264 keV [3.24%]) were easily resolved from samples measured at ~ 2 cm from the CdTe detector face; no other low energy X-ray peaks were observed.

3.3.3) Comparison to previous methods

Previous methods for producing germanium radionuclides focused on proton irradiation of encapsulated gallium metal or electroplated nickel-gallium alloys. Encapsulated targets withstand 10^2 μA proton intensities and 10^4 μAh fluences, yielding $0.4 - 0.5$ Ci of ^{68}Ge , though the ^{69}Ge is solely a short-lived contaminant in this context, so its yields are often unreported [91].

Electroplated NiGa₃ targets require 2-12 days to make, withstand a maximum proton current of 40 μA for 1 hour, and yield 0.7 mCi/ μAh of ⁶⁹Ge [28]. This TTY was achieved with 16 MeV protons, while the targets in this work received 12 MeV protons. The thin, milled, AR 1:3 Co:Ga targets investigated in this work were fabricated in \sim 8 hours, withstood 35 μA of proton irradiation for 30 min without damage, and yielded 340 $\mu\text{Ci}/\mu\text{Ah}$ ⁶⁹Ge ($n = 2$). The cobalt in the Co-Ga targets does not appreciably activate, and care is needed only in handling the niobium crucible which can contain appreciable levels of ⁹³Mo ($T_{1/2} = 6.9$ h) in thinner Co-Ga targets. With these targets, the desired germanium isotopes are formed at scale for application-oriented radionuclide research, motivating the application for a patent on intermetallic cobalt compounds for theranostic radionuclide production [92].

3.4) Conclusions

The reported results are convincing that Co-Ga targets minimize coproduced radioisotopic impurities, tolerate production-scale charged particle beam intensities, and achieve ^{69/71}Ge yields that will support exploration of *in vitro* and *in vivo* applications. Future work will focus on further optimization of the production scheme.

Chapter 4: Isolation and Purification of Radiogermanium from Irradiated Targets

4.1) Background summary and hypothesis

A few techniques for separating radioisotopes of germanium from gallium-based targets have been investigated. Detailed investigation results were reported [93] for the distillation of trace, volatile, radioactive $^{68}\text{GeCl}_4$ from concentrated HCl solutions (>6 M). This was based on a previous work [94] which focused on elemental germanium isolation from other elements in hydrochloric acid. The dissolution of irradiated gallium metal is facile with concentrated HCl and heat. Once dissolved, the radiogermanium is distilled out of solution as $^{68/69/71}\text{GeCl}_4$. Using a gas-tight distillation apparatus, recovery of the radiogermanium by condensation of the gaseous product downstream is quantitative (>99%) in 5-15 mL of acidic solution [93]. This technique is considered the gold standard for radiogermanium purification. Production of ^{68}Ge for RNGs at iThemba Labs in South Africa uses 2 – 12 g of encapsulated gallium metal with the distillation method and demonstrates the scalability of this separation method, with some modification [70].

The relatively large volume of final product solution from the distillation method has an HCl concentration of ~2 M under the best of conditions [93] and requires additional buffering and pH adjustment if application other than adsorption onto a column matrix is desired. For applications requiring higher activity concentrations, typically, the radioactive solution would be dried-down and the radioactivity reconstituted in a more suitable solvent. But, due to the azeotrope of HCl at ~6 M and the high volatility of GeCl_4 at this concentration, it is not feasible to dry-down and reconstitute this product. The adsorption of the radiogermanium onto a column matrix of some metal oxides (e.g. iron, aluminum, tin, or zirconium) is rapid and irreversible under acidic,

aqueous conditions [29,95], so the final distillate from this separation method is suitable for RNG production [70].

Another approach, reported in a review of germanium radiochemistry [29], involves the liquid-liquid extraction of $^{68/69/71}\text{GeCl}_4$ into an organic solvent with subsequent back-extraction into dilute HCl, based on previous work [96]. With this method, the irradiated gallium metal or NiGa_3 target (2-12 grams) is dissolved in concentrated HCl. The dissolved target solution is combined with the organic solvent in a separatory funnel and agitated for several minutes. Upon phase separation, manual operation of the separatory funnel stopcock isolates the aqueous phase, which must undergo several rounds of contacting with and separating from the organic phase to achieve quantitative separation of the GeCl_4 from the target material. The relatively large volume of the organic phase (10's of mL) containing the radiogermanium (GeCl_4) is then back-extracted with a similar volume of dilute HCl (0.1-1 M). The final product is available in a large volume of dilute HCl, where again dry-down and reconstitution are not feasible, but the final acid concentration is lower and requires less modification for subsequent application. The final product is suitable for RNG production [30,68,69,78,91,97]. The process also creates a large volume of hazardous organic solvent waste (e.g. CCl_4) with residual radioactivity and is difficult to automate.

More recent investigation [28] focused on a liquid chromatography scheme to separate radiogermanium from irradiated, electrodeposited NiGa_3 targets (~100 mg) dissolved in concentrated HNO_3 . They report that an extraction chromatography resin functionalized with diglycolamide (normal DGA resin) could be used to obtain $60 \pm 10\%$ of the radiogermanium from dissolved targets. The dissolved target is loaded onto the resin column using a peristaltic pump,

the resin is rinsed with concentrated HNO_3 and HCl to remove residual impurities/target material, and the resin is subsequently eluted with 0.5 - 2.5 mL of D.I. water to obtain the radiogermanium in the eluent. The separation scheme is illustrated below:

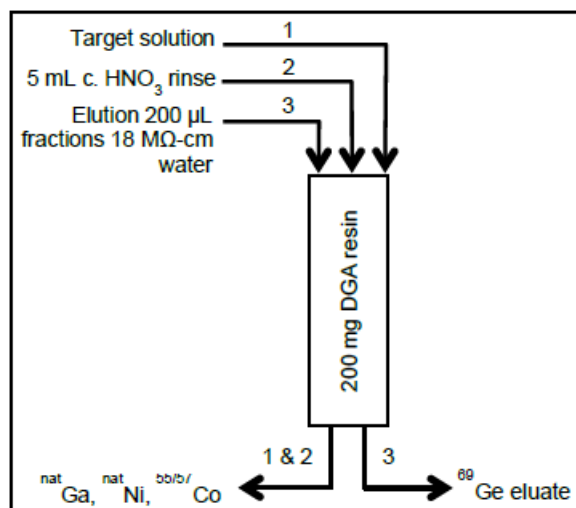


Figure 17: Extraction chromatography scheme for NiGa_3 targets dissolved in concentrated HNO_3 using normal DGA resin [28]

This method gives good separation of the radiogermanium from the target material, is potentially automatable, and the final product solution is suitable for subsequent radiolabeling of superparamagnetic iron oxide nanoparticles (SPIONs) with some buffering and pH adjustment.

Inspired by the column chromatography method, we chose to investigate the suitability of extraction chromatography resin for use with the Co-Ga target material. We hypothesized that the use of extraction chromatography resin would yield at least 50% of the radiogermanium in a small volume and with high separation factors and that the final product solution would be suitable for radiolabeling.

4.2) Materials & Methods

Normal and branched DGA resins were purchased from Triskem Int. (50-100 μm). Reagent grade concentrated HNO_3 was purchased from Fisher Chemical. Oxalic acid powder (99.999% trace metals pure) was purchased from Sigma Aldrich. 1- & 2-mL solid-phase extraction (SPE) plastic fritted columns were purchased from Supelco. Threaded borosilicate glass tubes with threaded Teflon plugs were purchased from Ace Glass Incorporated. 3" OD aluminum rod stock was purchased from Grainger. 18 $\text{M}\Omega\cdot\text{cm}$ D.I. water was obtained from a Millipore Synergy UV in-lab water supply.

4.2.1) Target Dissolution

Initially, 1 pellet of each atom ratio (AR) 1:2-1:4 Co:Ga was forged (as in section 3.2.1) and each pellet was placed in 1 mL of concentrated HNO_3 at room temperature and observed over 24 hours. A dissolution rig was fabricated in-house to dissolve the pressed targets. A 1" section of 3" OD aluminum rod stock was cut to produce a right-cylindrical disc (~1" thick with a 3" diameter). Into the middle of the curved surface (side), a $\frac{1}{4}$ " pilot hole was drilled most of the way through the aluminum block, and a Thunderbolt® style resistive heating unit was installed using thermal paste. Onto the flat surface of and centered on the disc, a 19.5 mm diameter depression was made with a lathe, 1 mm deep. This pocket aligns the pressed target on the heated dissolution block to the fluid column. Using threaded $\frac{1}{4}$ " rod stock, threaded into the Aluminum base, a plastic retaining bracket (Ultem®, ~1 cm thick, 3x3") with knurled Teflon nuts compressed the threaded borosilicate glass tube, threaded onto a cylindrical Teflon base (outfitted with an o-ring and groove), making a liquid-tight seal on the front face of the pressed targets. Photos of the dissolution rig are shown below:

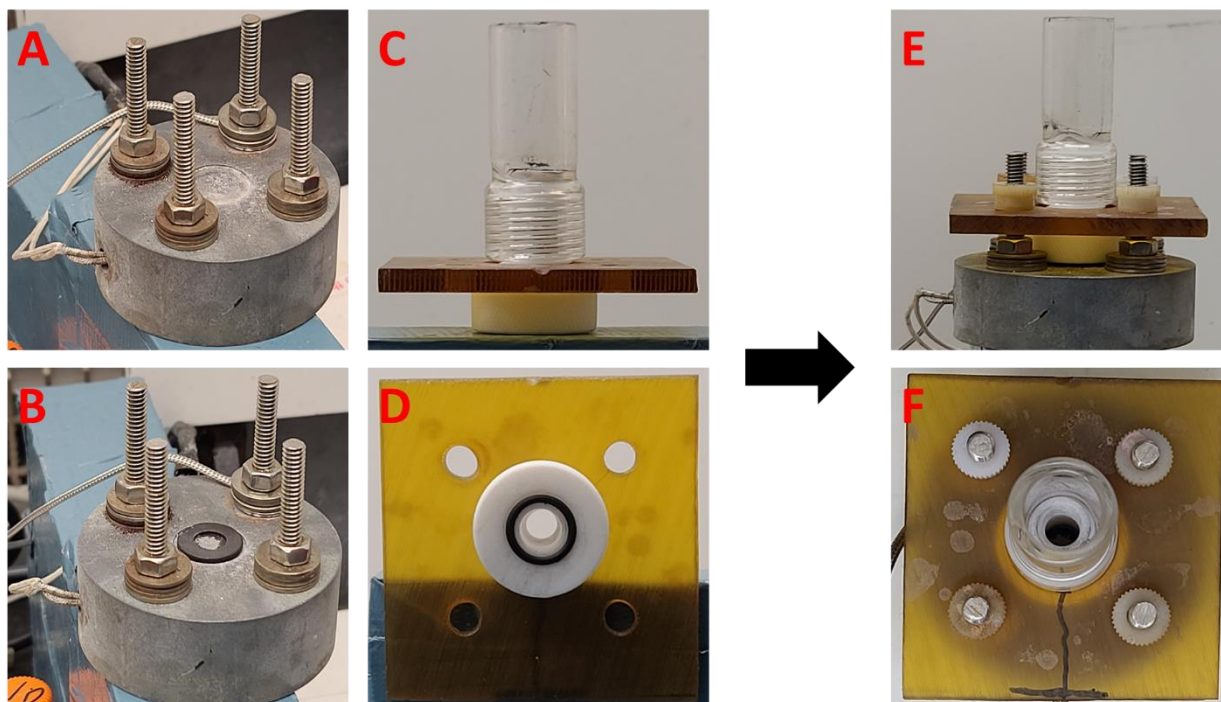


Figure 18: Dissolution rig base with threaded rods, thermocouple attached to the top, Thunderbolt® heater installed in the side, and alignment groove empty (**A**); niobium crucible with Co-Ga target placed in the alignment groove (**B**); Side view (**C**) and bottom view (**D**), threaded Teflon base mated to the Ace Glass column with Ultem® retainer seated on the base, Viton o-ring in the groove and alignment holes in the Ultem®; Side view (**E**) and top view (**F**), fully assembled dissolution rig ready to dissolve target.

A PID controller and a thermocouple attached to the top of the dissolution block base controlled the dissolution temperature. Approximately 5 mL of liquid in the threaded borosilicate tube and Teflon base comprise the fluid column which was in direct contact with the front surface of the pressed Co-Ga targets in the niobium crucible. Dissolution of the target was accomplished using 3.5-5 mL of concentrated HNO₃ at 70-80 °C for 1-4 hours.

4.2.2) Resin Affinity Studies

Distribution coefficients (K_D 's) for b. DGA and the cobalt and gallium target material, as well as the germanium product, were not available from the literature [98], so they were measured experimentally to identify possible conditions that effect chromatographic separation. Measurements of the K_D values across a range of HNO_3 concentrations were performed to probe the resin affinity for the analytes. No-carrier-added ^{67}Ga ($T_{1/2} = 3.26$ d, 100% ϵ) tracer was prepared using published methods [99], dried under N_2 flow in a glass reaction vial at 85 °C and rehydrated twice with c. HNO_3 . Irradiated CoGa_3 targets were dissolved as above (4.2.1) and transferred to the glass reaction vial containing dried ^{67}Ga , and the mixture was taken to dryness at 85 °C under N_2 flow.

The combined materials were dissolved again in 2-4 mL of 1 M HNO_3 . From this solution 100 μL aliquots were taken containing about 5% of the dissolved target and diluted to 1 mL with final HNO_3 concentrations ranging from 0.1-11 M. At first, using 1 mL SPE tubes with bottoms frits and home-made endcaps, sample aliquots were combined with approximately 50 mg of b. DGA and mixed for 10 or 100 minutes on a benchtop mixing plate. At the end of each time point, the liquid phase was separated from the solid phase. To do this, the caps were removed, and the liquid was expelled into 1.5 mL centrifuge tubes using an air-filled syringe. HPGe assay of both phases at each concentration of HNO_3 was performed. Quantification of the ^{58}Co , $^{66/67}\text{Ga}$, and ^{69}Ge by HPGe in each of the phases, plus the known volumes of liquid and masses of resin, enabled the calculation of the K_D values at each HNO_3 concentration and time point, following the formalism [98]:

$$K_D = \frac{\left(\frac{A_{solid}}{m}\right)}{\left(\frac{A_{liquid}}{v}\right)}, \text{ or, } \frac{\left(\frac{M_{pre-resin} - M_{post-resin}}{m}\right)}{\left(\frac{M_{post-resin}}{v}\right)}$$

where A_{solid} is the activity of the analyte on the solid phase, $M_{pre-resin}$ and $M_{post-resin}$ are the masses of the analyte in solution before and after contact with the resin, respectively, m is the mass of the resin in grams, A_{liquid} is the activity of the analyte in the liquid phase, and v is the volume of the solution in mL.

These results informed on the optimal conditions to achieve chromatographic separation in the dynamic column experiments. The affinity study was repeated using approximately 250 mg of b. DGA. This time, 2 mL SPE tubes with Luer caps and plugs for endcaps were used following the same procedure as before but forgoing the 100-minute contact time measurement. Then, the gallium and cobalt K_D values were estimated using trace metal analysis results obtained by MP-AES performed on sample aliquots pre- and post-resin contact.

4.2.3) Dynamic Column Separation

An initial radiochemical isolation experiment used an irradiated Co-Ga target (AR 1:3, ~180 mg) dissolved in c. HNO_3 to probe the suitability of the radiochemical separation method from [28]. The dissolved target solution was diluted with c. HNO_3 to 30 mL and split into 3 fractions. Each fraction was loaded onto 200 ± 50 mg of normal DGA resin equilibrated with c. HNO_3 . Columns were rinsed with 5 mL of c. HNO_3 and eluted with $5 \times 200 \mu\text{L}$ of D.I. water.

Informed by the results of the resin affinity studies, an optimal loading condition for the $^{69/71}\text{Ge}$ on the b. DGA resin was identified where the affinity was high for $^{69/71}\text{Ge}$ and correspondingly low for the cobalt and gallium. Dynamic column experiments were performed with b. DGA under

the identified conditions to investigate the separation of the $^{69/71}\text{Ge}$ from the bulk target material. For these experiments, irradiated targets were dissolved as above (4.2.1) in 3.5-5 mL of c. HNO_3 . Theoretical calculations estimate the final concentration of nitric acid to be approximately 11 M after dissolution. For each separation experiment, 150-400 mg of b. DGA was equilibrated using 5 mL of D.I. water, 5 mL of 0.1 or 1 M oxalic acid, and 10-20 mL of 11 M HNO_3 . The entire dissolved target solution was then passed through the equilibrated resin column at 1 mL/min using a peristaltic pump (Welco WPW2). The loaded resin column was rinsed with 10-40 mL of 11 M HNO_3 . And finally, 2.5 – 5 mL of 0.1 M HNO_3 , 0.1 or 1 M oxalic acid, or D.I. water was passed through the column to elute the radiogermanium in 0.5 – 1 mL fractions. All fractions were measured by HPGe spectrometry to characterize the cobalt and germanium radionuclides' distribution and subjected to trace metal analysis. The residual ^{69}Ge on the column was also quantified by HPGe.

4.2.4) Final Product Characterization

HPGe assay was performed as described in section 2.2.5. Trace metals were quantified by MP-AES following the protocol in 2.2.5. Here, however, calibration standards of 10 ppb to 100 ppm cobalt, copper, iron, gallium, and zinc were made in 0.5 M HNO_3 . The detection limits for each analyte were determined from calibration curves (~30 ppb for cobalt and gallium in diluted samples). The HPGe quantification of the ^{69}Ge and the MP-AES quantification of the cobalt and gallium in the dissolved target and eluted product fractions were used to calculate the SFs for $^{69/71}\text{Ge}$ with respect to the cobalt and gallium bulk target material using the formalism presented in 2.2.5.

4.3) Results and Discussion

Current methods for separating isotopes of germanium from gallium-based targets revolve around liquid-liquid extraction of volatile, radioactive germanium tetrachloride [91]. Large volumes of organic solvents are necessary to achieve the high radiochemical yield (>90%) with this method, which is not well suited to automation and requires an operator's presence; this is dosimetrically undesirable. Liquid chromatographic separation was investigated to overcome some of these challenges. The method from [28] using normal DGA resin was unable to yield more than 20% of the $^{69/71}\text{Ge}$ from the dissolved Co-Ga target material, which motivated the investigation of b. DGA resin. The results below are encouraging that the b. DGA method is suitable for radiochemical isolation of $^{69/71}\text{Ge}$ from the dissolved Co-Ga targets.

4.3.1) Target Dissolution

From theory, an estimated 1.5 mL of c. HNO_3 is needed to fully dissolve 500 mg of CoGa_3 . Since only 1 mL was used, target solubility in c. HNO_3 was investigated. The AR 1:2 pellet seemed to dissolve partially, darkening the solution slightly and leaving large chunks of residue in the bottom of the plastic 1.5 mL centrifuge tube. AR's 1:3 and 1:4 seemed to dissolve readily at room temperature with gas bubbles evolving and darkening of the solutions and ultimately little to no silty residue in the bottom of the tubes by the end of 24 hours. Referring to the Co-Ga phase diagram (section 3.2.1), there are 2 known alloys of Co+Ga in the AR range investigated: CoGa and CoGa_3 . AR 1:2 targets had limited solubility in the c. HNO_3 , suggesting that the formation of the CoGa phase inhibits dissolution in c. HNO_3 . By contrast, in the AR 1:3 & 1:4 pellets, the primary phases present were CoGa_3 and elemental gallium, and these pellets dissolved more rapidly. Hot-pressed targets were dissolved at 80 °C to accelerate the dissolution process. After irradiation

and 2 hours of dissolution in 15 mL c. HNO₃ at 80 °C, 84 ± 3% (n = 3) of the ⁶⁹Ge activity was reclaimed from thick unmilled AR 1:3 targets. Dissolution volume was reduced to 5 mL, yielding ~70% of the ⁶⁹Ge from thick and thin (milled and unmilled) targets. Residual, undissolved target material was cleaned from the niobium crucibles after a decay period using aqua regia, and the cleaned crucibles were then recycled for further target pressing and processing.

4.3.2) Distribution Coefficients (K_d's)

Following the procedure outlined in section 4.2.2, the initial b. DGA resin affinities were measured using the 1 mL SPE tubes and ~50 mg of resin with the dissolved target aliquots. These results are shown in the plot below:

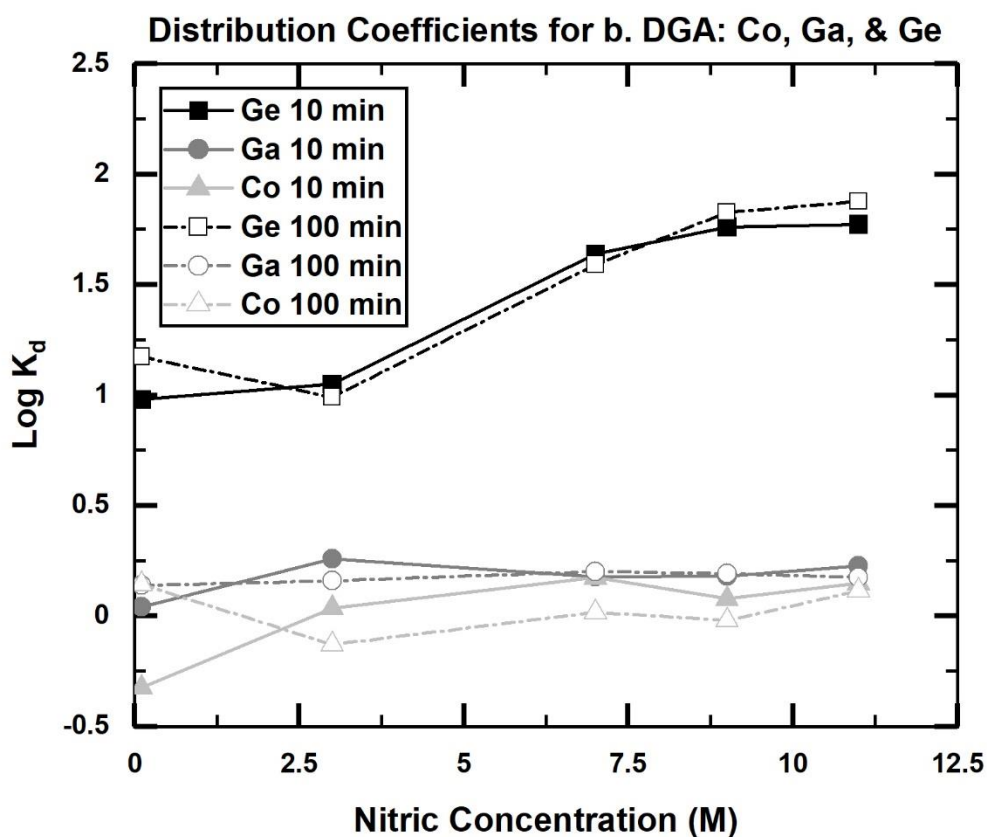


Figure 19: Log of the distribution coefficients (K_D in mL/g) for ^{69}Ge , ^{67}Ga , and ^{58}Co on b. DGA resin in nitric acid determined by HPGe quantification of radioactivity in the solid and liquid phases for 10 (solid) or 100 (dashed) min of contact time.

A separation scheme for the dynamic columns was devised and implemented: the dissolved target was loaded onto the equilibrated resin in >11 M nitric, the column was rinsed with >11 M HNO_3 , and the $^{69/71}\text{Ge}$ was eluted in dilute acid. 11 M was selected for the loading conditions in case the dissolved target solution HNO_3 concentration was lower than calculated from theory (~11 M, as noted in section 4.2.3). However, in performing the initial batch resin study, about 50 mg of b. DGA resin was contacted with each sample aliquot (about $1/40^{\text{th}}$ of the dissolved, spiked target) containing 12 mg Co + Ga. The resin capacity reported by Triskem Int. is 15 mg Eu^{2+} per mL of resin. For 50 mg of resin, the capacity would be about 1.5 mg of $\text{Co}^{2+,3+} + \text{Ga}^{3+}$; much lower than the 12 mg of Co + Ga present in those aliquots. Because of this, the preliminary measurements may have been skewed by mass effects, so the batch resin study was repeated using ~1 mg of Co + Ga in solution and increasing the resin mass to ~250 mg. This required the use of the larger volume (2 mL) SPE tubes to accommodate the increased resin volume. Only 10 minutes of resin contact time was measured since the residence time on the resin in the dynamic columns was less than 10 minutes, but certainly less than 100 minutes. The results from this measurement are plotted below for comparison:

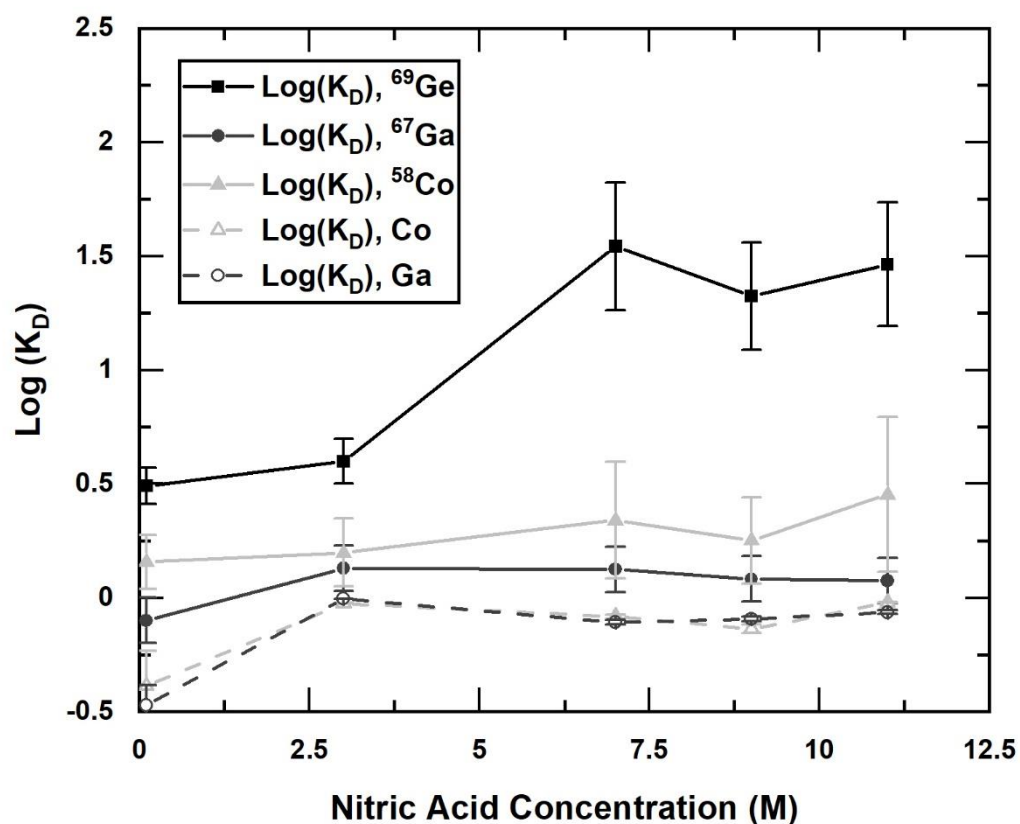


Figure 20: Log of the distribution coefficients (K_D in mL/g) for ^{69}Ge , ^{67}Ga , and ^{58}Co on b. DGA resin in nitric acid determined by HPGe quantification of radioactivity in the solid and liquid phases (solid lines and symbols) and trace metal analysis data from the liquid phase pre- and post-resin contact (dashed lines, hollow symbols) for 10 min of contact time.

Despite concerns about mass effects on the initial resin affinity measurements, the improved batch resin study produced comparable results. Encouraged by this, the devised separation scheme was employed for the dynamic column experiments.

4.3.3) Dynamic Column Separation Results

The Co-Ga target separation following the method employed by [28] had a poor ^{69}Ge radiochemical yield (figure 21):

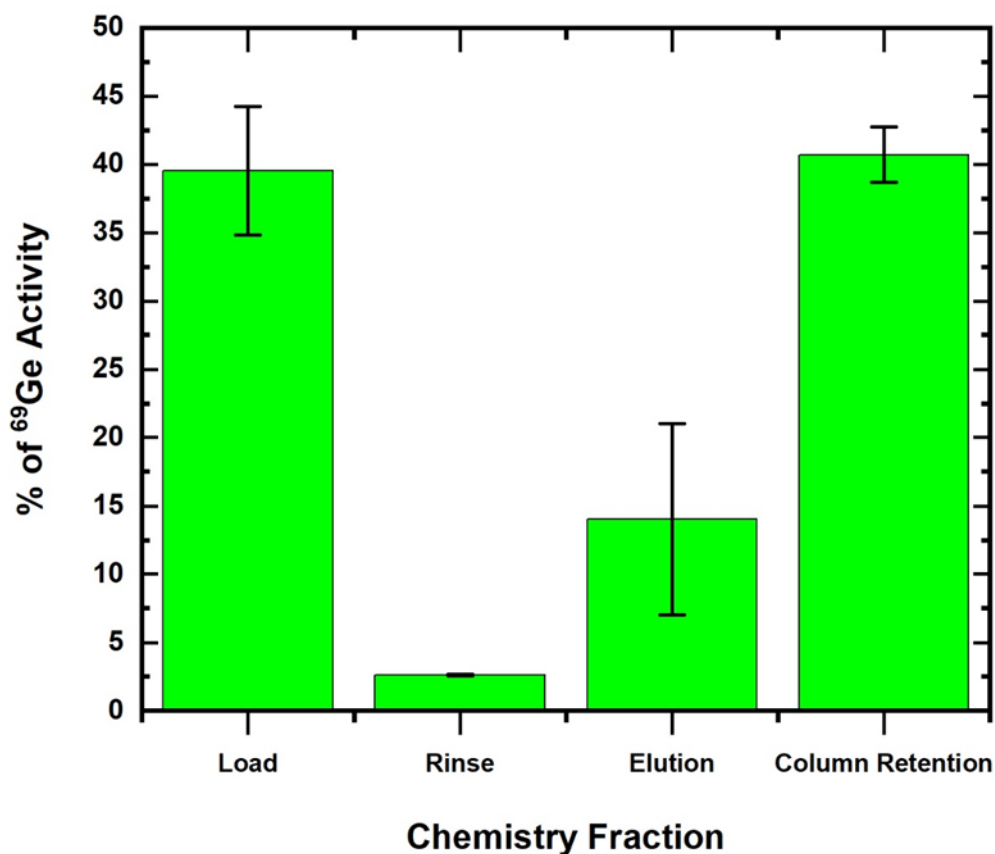


Figure 21: Elution profile summary for Co-Ga dissolved in HNO_3 on normal DGA resin with the percentage of ^{69}Ge activity in each fraction on the vertical axis

For the Co-Ga targets on the normal DGA resin, $42.2 \pm 4.8\%$ ($n = 3$) of the ^{69}Ge activity was lost to breakthrough in the load and rinse steps. $14 \pm 7\%$ ($n = 3$) of the ^{69}Ge activity was eluted from the column in the combined 1 mL of D.I. water eluent, and $40.7 \pm 2.0\%$ ($n = 3$) of the ^{69}Ge activity

remained trapped on the normal DGA columns. The poor radiochemical yield from the normal DGA method motivated the investigation of the b. DGA resin's suitability for the task.

Informed by the first batch resin study, initial dynamic column separation experiments with the b. DGA resin investigated the suitability of the separation scheme on the resin columns. Despite the low measured affinity for the ^{69}Ge on the b. DGA across the range of 0.1 – 3 M HNO_3 (figures 19 & 20), a small fraction of the total ^{69}Ge activity eluted off the b. DGA resin columns using 0.1 M HNO_3 or just D.I. water. Near quantitative elution of the ^{69}Ge was obtained using 1 M oxalic acid. The results from this column experiment are plotted here below for a visual summary:

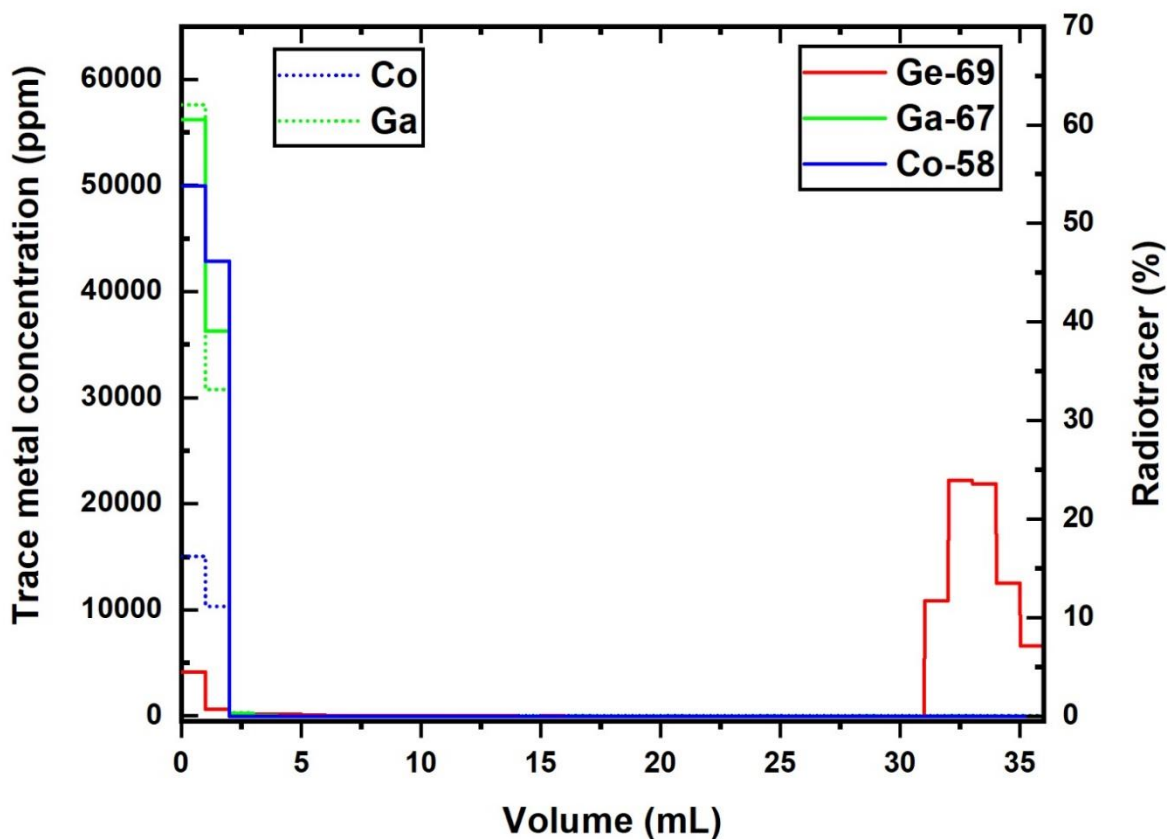


Figure 22: Elution profile from the most successful trial separation (1 M Oxalic elutions). Trace metal concentration is plotted in the dashed blue and green lines for cobalt and gallium (left axis). Normalized radiotracer distributions are plotted as blue and green symbols for cobalt and gallium, with a red line for the ^{69}Ge (right axis).

This result was obtained using ~ 150 mg ($1/3^{\text{rd}}$) of a dissolved CoGa_3 target in 1 mL of 11 M HNO_3 loaded onto ~ 250 mg of equilibrated b. DGA resin. $99.0 \pm 0.3\%$ ($n = 3$) of the cobalt and gallium target material eluted with the load and the first mL of rinse in each of the initial columns. In the load and full 30 mL rinse, $10.3 \pm 4.4\%$ of the ^{69}Ge activity broke through the columns. 13% of the germanium activity remained on the columns after elution. For the successfully eluted column, 1 M oxalic acid eluted $\sim 80\%$ of the ^{69}Ge in 5 mL (collected in 1 mL fractions for analysis). In most of the eluted fractions, the cobalt was below the limit of detection (~ 300 ng). The gallium was measured at about 10 μg in each eluted fraction.

Encouraged by this initial success, further separation experiments varied the rinse and eluent volumes and concentrations, looking at the effect on ^{69}Ge breakthrough and radiochemical yield (RCY). For CoGa_3 targets, the optimized separation scheme loaded ~ 200 mg of the dissolved, irradiated target in 5 mL of approximately 11 M nitric acid onto the resin column. This was followed by two 10 mL rinses with 11 M HNO_3 , 5 mL of 9 M HNO_3 , and finally 2.5 mL of 6 M HNO_3 . Then, five 500 μL fractions of 0.1 M Oxalic acid eluted the ^{69}Ge activity. A representative elution profile using the improved method is provided here:

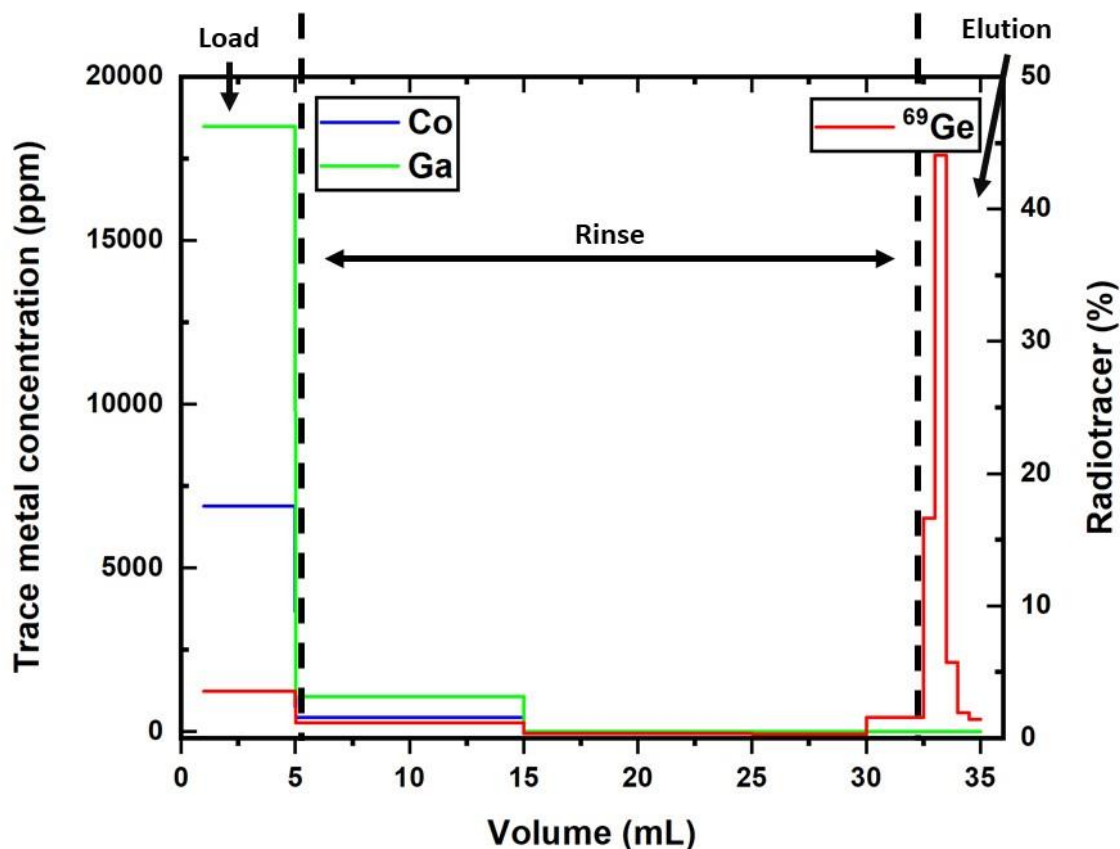


Figure 23: Elution profile from the optimized separation scheme (step-down HNO₃ rinse concentrations, 0.1 M oxalic acid elution). Trace metal concentration data is plotted in the green and blue lines (left axis), the normalized radiotracer distribution is plotted as the red line (right axis). Labels and arrows denote the load, rinse, and elution fractions.

Whole Co-Ga targets (~200 mg, thin, milled) dissolved in 3.5 – 5 mL of c. HNO₃ were loaded onto ~250 mg of equilibrated b. DGA resin. >99.0 % (n = 2) of the cobalt and gallium target material eluted with the load and first 10 mL rinse. In the load and combined rinse fractions, $7.0 \pm 0.6\%$ of the ⁶⁹Ge activity broke through the resin. In the 0.1 M Oxalic acid elution fractions combined, $69.8 \pm 12.9\%$ (n = 2) was recovered from the resin. With the full targets now processed on the

resin columns, $26.9 \pm 2.5\%$ ($n = 2$) of the germanium activity remained on the column after elution, compared to the 13% during the initial separations. And, as with the initial separations, cobalt was below the limit of detection (~ 300 ng) in most eluted fractions, and $1 - 3$ μg of gallium was detected in each eluted fraction, constituting about a factor of 10 decrease compared to the initial separation results.

4.3.4) Total Radiochemical Yields, Radionuclidic Purity, and Separation Factors

For the initial separation scheme (figure 22), the total RCY of ^{69}Ge was $\sim 60\%$ in the eluted product (decay corrected to EoB) and the radiochemical purity (RCP) was $>99\%$. The radionuclidic purity (RNP) was $>95\%$ ^{69}Ge at EoC, and the SFs for ^{69}Ge were $\geq 1 \times 10^4$ relative to gallium and cobalt. The optimized separation scheme RCY was $\sim 50\%$ of the ^{69}Ge in the eluted product (at EoB) and again the RCP was $>99\%$. The RNP was still $>95\%$ for ^{69}Ge at EoC, and the SFs still at least 1×10^4 . A plot of the gamma spectrum obtained by HPGe for eluted ^{69}Ge shows results obtained at EoC and 18 days post-EoC such that the ^{69}Ge activity would be sufficiently decayed (by a factor >2000) and trace radioimpurities might be observed and quantified:

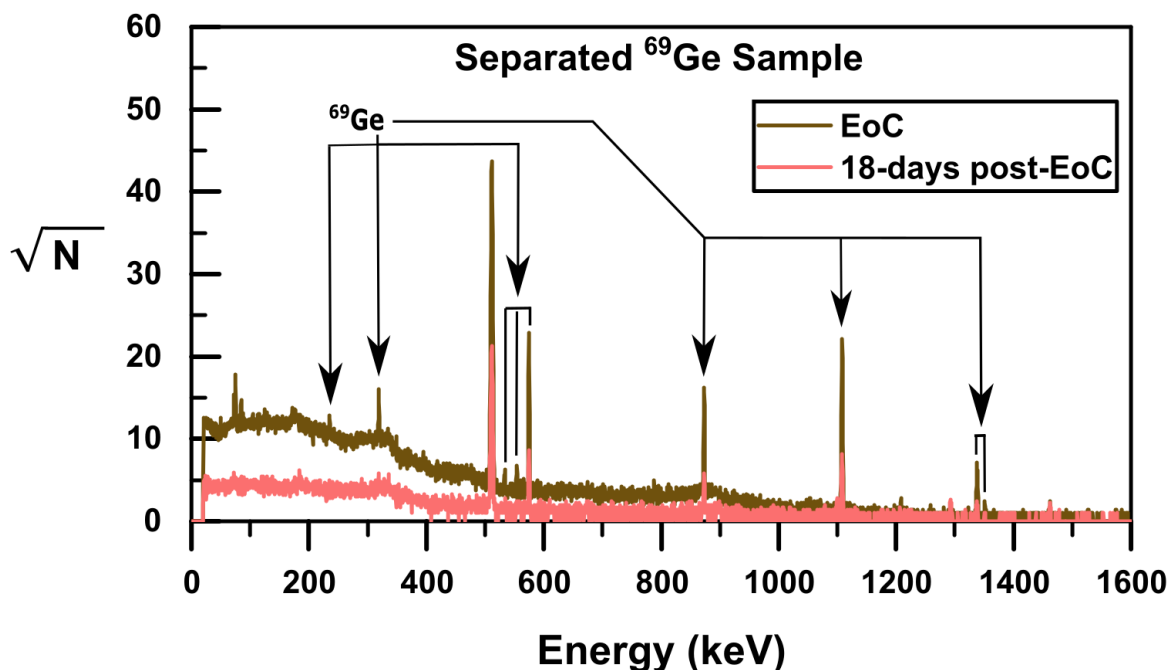


Figure 24: HPGe measured gamma spectra of the first eluted fraction from trial b. DGA column **brown**) at EoC and **coral**) ~18 days post-EoC. Arrows and brackets indicate the ^{69}Ge peaks.

The large 511 keV peak is primarily attributed to the positron emission of ^{69}Ge ($I_{\beta^+} \approx 25\%$). The other photopeaks observed are those of ^{69}Ge : 234.8 keV (0.4%), 318.6 keV (1.6%), 532.7 keV (0.3%), 553.4 keV (0.7%), 574.1 keV (13.3%), 872 keV (11.9%), 1106.8 keV (36%), 1336.6 keV (4.5%), and 1349.8 keV (0.3%). The final RNP of the ^{69}Ge in the eluted fractions from this column is >95%, with no identified radioactivity other than ^{71}Ge . The decay period, greater than 10 half-lives of ^{69}Ge and reducing the eluted fraction's activity from $\sim 20 \mu\text{Ci}$ to less than 10 nCi, did not reveal the presence of any co-produced ^{58}Co contaminant peaks above the limit of detection, determined to be 0.2 nCi following published methods [100].

4.4) Conclusions

The final RCP of the product from this work is comparable to that of the other methods, >99% at EoC. The separation factors for the bulk target material are conservative, as they were estimated from the minimum detection limit in some cases (mostly for the cobalt). The SFs were calculated and found to be greater than 1×10^4 for both the cobalt and gallium, relative to the $^{69/71}\text{Ge}$ product, comparable to the $\sim 10^6$ reported for the Ni-Ga targets. The overall radiochemical yield for the improved b. DGA resin separation method was found to be $\sim 50\%$. Careful optimization of the target dissolution and transfer of the liquid phase is expected to increase this overall efficiency, and optimization of the column separation method continues.

Chapter 5: Radiolabeling with Radiogermanium

5.1) Background summary and hypothesis

Multiple studies of germanium biodistribution and kinetics in animals found that GeCl_4 [101], GeO_2 , or sodium germanate [102–104] exhibited little organ-specific uptake following parenteral injection or ingestion. One investigation [105] found long-term tissue uptake using Ge(OH)_4 , observed in the spleen and kidneys. The development of a germanium-based radiotracer could enable studies to elucidate the biodistribution and pharmacokinetics of germanium previously missed by ex-vivo examination. While inorganic germanium (i.e. GeO_2 or germanium lactate-citrate) inhibited tumor promotion in rat liver cells in vitro [106], it is also nephrotoxic, and its import is banned in the U.S. [107]. Organic forms of germanium (i.e. spirogermanium, germanium yeast, or Ge-132) are reportedly involved in a whole host of biological activities, among them potential antitumoral and antimicrobial effects which could be therapeutically useful: inhibiting DNA, RNA, and protein synthesis [108], inducing γ -interferon production [109], inhibiting the growth of bacteria and yeasts [110] and fungi [111], and inhibiting growth and maturation of chloroquine-resistant strains of malaria [112].

Analysis of dietary intake and baseline levels in humans found that 400 - 3500 μg per day of germanates are ingested in food and drink, with comparable amounts excreted in the urine [113]. Several patients developed fatal lactic acidosis and germanium-induced nephropathy after taking germanium supplements [114–116]. Overexposure to germanium compounds also causes neuropathy or neurotoxicity [108,117,118]. Possible pulmonary toxicity from organic forms of germanium has been reported [119]. Because of the reported safety risks associated with organic

germanium compounds, the FDA discourages their production and usage [120]. And while germanium is present in trace amounts in the diet of humans, with the increased use of germanium-based, growth-promoting methods in parts of southeast Asia applied to livestock [21], the average daily intake for humans may be increasing and so a more thorough understanding of germanium biodistribution in humans is highly desirable.

Synthesizing a germanium-based compound that may have inherent antitumorigenic properties with radiogermanium presents a somewhat unique opportunity among radiometals as this could be achieved chelator-free. Only one other example of this intrinsic labeling possibility for radiometals has been explored in any detail, on the synergistic effect of $^{191/195m}$ platinum-labeled cisplatin in glioblastoma treatment *in vitro* [121]. By contrast, the more typical radiometal labeling process, as with clinically approved ^{68}Ga -PSMA compounds, involves significant chemical modification to radiolabel the PSMA targeting vector and these modifications have a dramatic effect on the pharmacokinetics of the PSMA compounds [122]. This chelating ligand paradigm is widely applied to radiometal theranostics currently being explored, including but not limited to the ^{68}Ga example presented here.

To date, the chelation/coordination of germanium radioisotopes has only been investigated as far as successful methods for RNG production: the selective and permanent adsorption/retention of the germanium on a column matrix [123–127]. Building on this chemical property of germanium, previous investigation [128] reported successful radiolabeling of superparamagnetic iron oxide nanoparticles (SPIONs) with ^{69}Ge for PET/MR applications. The RNG production method is not targeted at *in vivo* application of the radiogermanium, and the nanoparticle approach is hindered greatly by a lack of ability to be specifically targeted *in vivo* (its behavior *in*

vivo is dominated largely by the size of the nanoparticles and the body's pathways for molecules of this size). So, chelation of radiogermanium with a potentially modifiable ligand, whose biodistribution and pharmacokinetics can subsequently be tailored to a particular application, is an important objective.

Since the 1950s, the antitumor and antimicrobial properties of thiosemicarbazones (TSCs) have been observed and reported on in the literature [129–131]. Stable germanium complexation has been achieved using the TSCs [132–134]. Stable germanium has also been successfully coordinated with the tetrathiolate active site of rubredoxin proteins [135]. Inspired by these reports, we hypothesized that a thiol-based chelator for radiogermanium would be stable *in vivo* and possible to bifunctionalize (conjugate with a targeting moiety) for diagnostic imaging and targeted radiotherapy research. Radiolabeling of germanium complexes with reported intrinsic targeting properties (i.e. the TSCs) also merits exploration. We investigated the coordination of our no-carrier-added radiogermanium product with various thiol-based chelating/complexing agents.

5.2) Materials and Methods

Trace metal free sodium acetate was purchased from Sigma Aldrich. Reagent grade sodium hydroxide was purchased from Fisher Scientific. HPLC grade acetonitrile and D.I. water were purchased from Sigma Aldrich. Reagent grade methanol and ethanol were purchased from Sigma Aldrich. Reagent grade HCl, C18 purification cartridges, and TCEP were purchased from Fisher Scientific. Lipoic acid (LA) was purchased from Sigma Aldrich. A model trithiol chelator was

generously provided through collaboration with the Jurrison group at the University of Missouri (referred to hereafter as the “Mizzou trithiol chelator”).

5.2.1) Labeling Conditions for Thiol-based Chelators

The eluted radiogermanium product (following the method detailed in Chapter 4) was acidic, with a pH of ~ 1 , eluted in oxalic acid. From the literature we found theoretical speciation diagrams for germanium in aqueous medium with oxalic acid [136]:

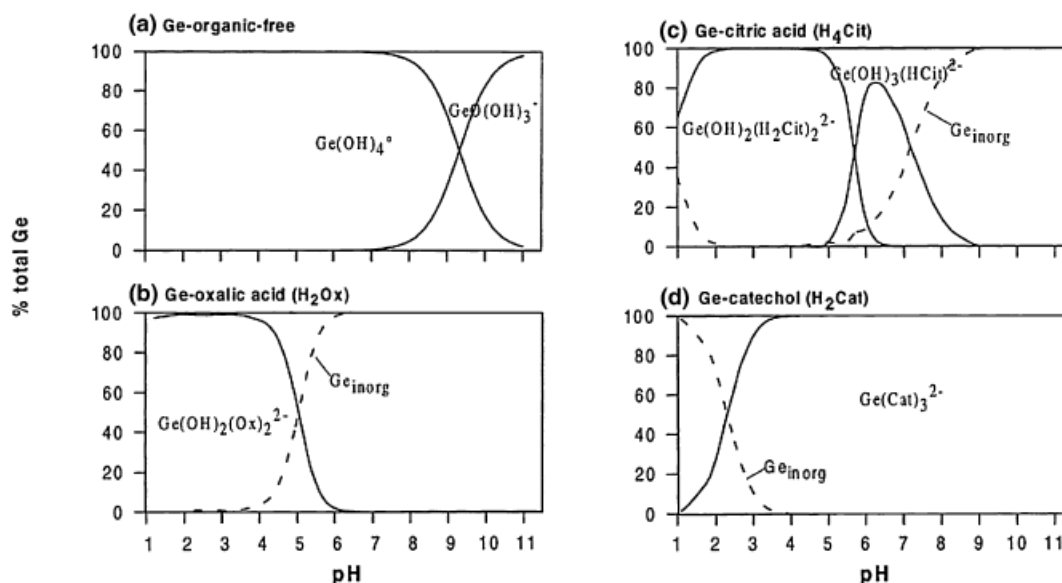


Figure 25: Distribution curves of Ge hydroxide complexes (a) and Ge complexes with oxalic acid (b), citric acid (c), and catechol (d) as a function of pH at 25 °C in aqueous solutions containing 0.02 M of Ge and 0.1 M of corresponding organic compound. The dashed lines represent the percentage of the free inorganic germanium, $\text{Ge}_{\text{inorg}} = [\text{Ge}(\text{OH})_4]^0 + \text{GeO}(\text{OH})_3^-$, in the presence of the organic ligands. All curves were generated using the stability constants for Ge species reported by Pokrovski and Schott (1998b) (reproduced by permission of Elsevier from

Pokrovski et al. (2000)) [137]

Informed by this report, we selected pHs of ~1 and 4-5 for our radiolabeling investigation. Commercially available, high purity LA was obtained for investigation and the Mizzou trithiol chelator was provided through collaboration with the Jurrison group. The chelator's structures are shown below for reference:

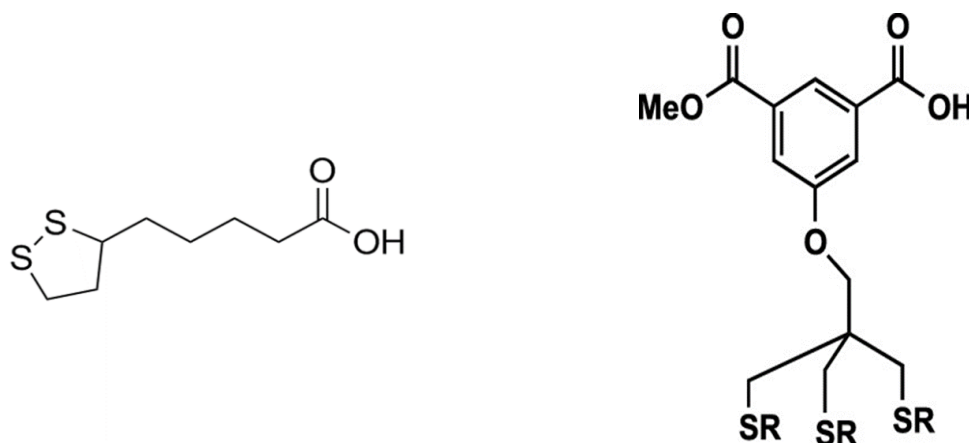


Figure 26: Structure of (**left**) unreacted LA and (**right**) the Mizzou model trithiol chelator with protecting groups for shelf-stability, where R = CN [138]

Before labeling, the thiol-based chelators must have their disulfide bridges reduced, and in the case of the Mizzou trithiol, have the cyanate protecting groups removed (deprotected). This was accomplished using a 10x molar excess of TCEP and heating the mixture for 2 hours on a benchtop mixing plate. The thiol-based chelators were dissolved in acetonitrile (due to their hydrophobicity) and combined with TCEP dissolved in D.I. water to yield the 10x molar ratio in 1.5 mL plastic centrifuge tubes. The tubes were placed on the heated mixing plate at 55 °C for 2 hours. 100 μ L of the deprotected/reduced chelator solution was added to the radiogermanium product either as eluted (at pH ~1) or buffered with 100 μ L of 1 M NaOAc and adjusted to pH 4-

5 with NaOH. The reaction mixture was set on the mixing plate at 55 °C for 2 hours. The results of the labeling reaction were assessed by radio-HPLC, described later in section 5.2.3.

5.2.2) Purification of the Labeled Complex

Purification of the labeled complex was investigated with C18 purification cartridges as well as by semi-preparatory HPLC (semi prep HPLC). The C18 cartridges were rinsed with 2.5 mL of EtOH and equilibrated with 5 mL of D.I. water. The labeling reaction solution was diluted to 5 mL with D.I. water and loaded onto the C18 cartridge. The cartridge was rinsed with an additional 2.5 mL of D.I. water, and the radiolabeled complex was eluted in 1 mL of EtOH. The EtOH eluent containing the radiolabeled complex was dried down under N₂ gas flow and reconstituted in PBS for stability experiments.

For the semi prep HPLC purification method, an UltiMate Model 3000 HPLC system with a Phenomenex C18 (5 μ , 100Å, 250 x 10 mm) reverse-phase preparatory HPLC column, built-in UV-VIS absorbance detectors and an in-line, downstream radiation detector was used to purify samples. A 2 mL sample injection loop was installed on the system, and a 30-minute method was used with a binary mobile phase. The 2 mobile phase constituents were A) HPLC grade D.I. water with 0.1% TFA and B) HPLC grade acetonitrile:

| Time (min) | % A (D.I. w/ 0.1% TFA) | % B (Acetonitrile) |
|-------------------|-------------------------------|---------------------------|
| 0 | 95 | 5 |
| 2 | 95 | 5 |
| 5 | 40 | 60 |
| 20 | 10 | 90 |
| 25 | 10 | 90 |
| 28 | 95 | 5 |
| 30 | 95 | 5 |

Table 5: HPLC binary mobile phase gradient

A simplified diagram of an HPLC system is shown here:

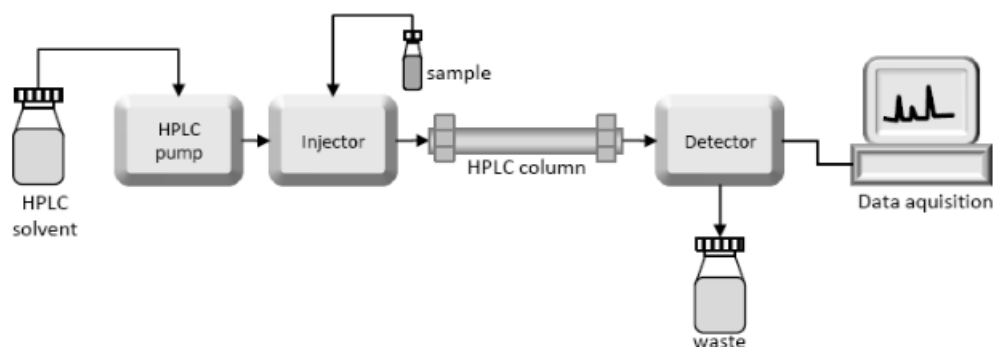


Figure 27: Schematic of an HPLC system [139]

On our HPLC system, the UV-VIS detector is followed downstream by the radiation detector. Radiolabeling reaction solutions were diluted to 2 mL using HPLC mobile phase (95% A, 5% B) and injected into the sample loop. The radiopeak corresponding to the radiolabeled complex was isolated from the waste stream in a 15 mL falcon tube for formulation and stability experiments.

5.2.3) Final Product Characterization by radio-HPLC

The HPLC system described in 5.2.2 was used to perform analytical HPLC on radiolabeling reaction solutions and purified/formulated products. A 20 μ L sample injection loop and Phenomenex C18 reverse-phase column (5 μ , 100 \AA , 250 x 10 mm) were installed on the system and, samples were analyzed with the same 30-minute method detailed above. Additionally, HPLC analysis of all the labeling reagents aided in the interpretation of the HPLC traces obtained from the labeling reactions.

5.3) Results and Discussion

With the exception of the ^{69}Ge -labeled SPIONs [128], no other reports of ^{69}Ge -labeled compounds were found searching the literature. Both the LA and the Mizzou chelators have been reported on for successful radiolabeling with ^{77}As [138,140]. As and Ge are adjacent to one another on the periodic table and are both metalloids, so potential similarities in their coordination chemistry were investigated. We found that the complexation of $^{69/71}\text{Ge}$ with both chelators was possible, but the complexes were unstable at neutral pH or in simulated physiological conditions.

5.3.1) Thiol Complexation Results

The disulfide bridges between the thiol functional groups on LA were reduced using 10x TCEP (as described in section 5.2.1). Plotted UV-VIS HPLC results show the change in retention time (218 nm trace) and peak height (254 – 330 nm traces) for the characteristic LA peak at retention time (RT) ~9.5 min, which are effects of the reduction of the chelator:

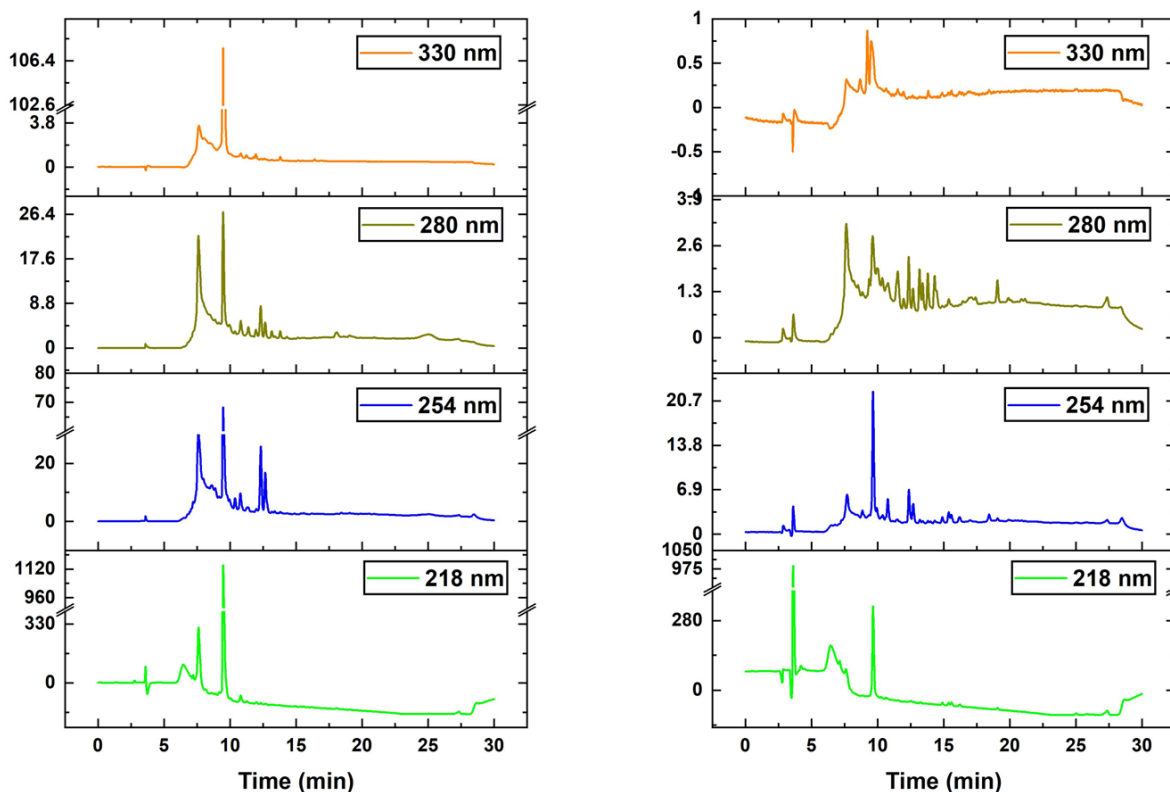


Figure 28: HPLC UV-VIS traces for LA pre (**left**) and post (**right**) reduction with 10x TCEP

The TCEP reducing agent and NaOAc buffering solution were also analyzed by UV-VIS HPLC. These results were used to analyze and interpret the radio-HPLC results obtained from analysis of the various reaction conditions. $^{69/71}\text{Ge}$ -oxalate (as eluted from the b. DGA column, 0.1 M Oxalic Acid, pH \sim 1) was buffered with NaOAc (1 M, 100 μL) and pH-adjusted to \sim 5 using 1 M NaOH. The buffered $^{69/71}\text{Ge}$ -oxalate was combined with reduced LA (as described in section 5.2.1), and both solutions were analyzed by radio-HPLC (section 5.2.3) to determine the RT of the $^{69/71}\text{Ge}$ -oxalate and observe differences in behavior which could indicate a successful reaction with the chelator. Figure 29 shows the plotted results:

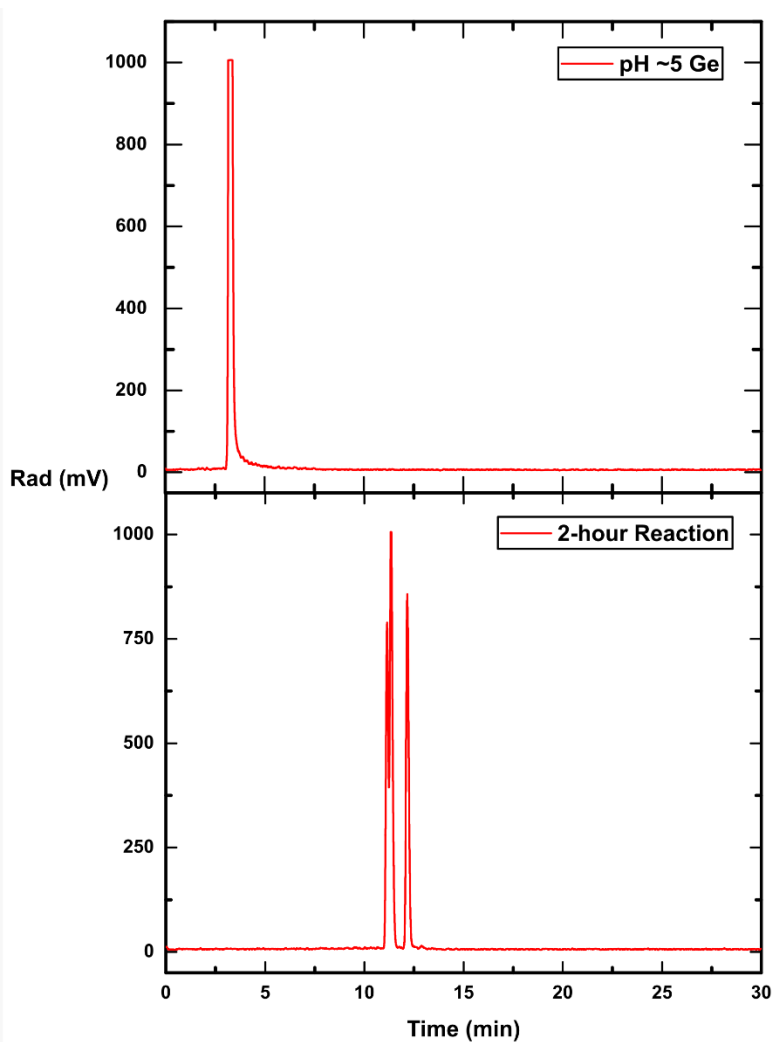


Figure 29: **upper)** Unbound $^{69/71}\text{Ge}$ -oxalate buffered to pH ~ 5 and **lower)** $^{69/71}\text{Ge}$ -oxalate after chelation with LA

The $^{69/71}\text{Ge}$ -oxalate eluted from the HPLC column with a RT of ~ 3.5 min, coincident with the solvent front. This behavior is characteristic of soluble molecules in aqueous solution, as expected with $^{69/71}\text{Ge}$ -oxalate. After the 2-hour reaction at 55°C without pH-buffering, no indications of chemical reaction were evident from the radio-HPLC trace; all the $^{69/71}\text{Ge}$ eluted with a RT of ~ 3.5 min and no other radiopeaks were observed. However, after the 2-hour reaction at pH ~ 5 , no $^{69/71}\text{Ge}$ -oxalate peak at RT ~ 3.5 min was observed. Instead, 3 new radiopeaks were

observed at RT ~ 10.5 and ~ 12 min. These are likely $^{69/71}\text{Ge}$ coordinated with 1 LA molecule (RT ~ 10.5 min), and 2 LA molecules (RT ~ 12 min) but have not been confirmed.

10x TCEP deprotection was carried out as described in section 5.2.1 to prepare the Mizzou trithiol chelator for reaction with our $^{69/71}\text{Ge}$ -oxalate, as with the LA. The UV-VIS HPLC results plotted (figure 30) were obtained from the Mizzou chelator pre- and post-reduction with 10x TCEP:

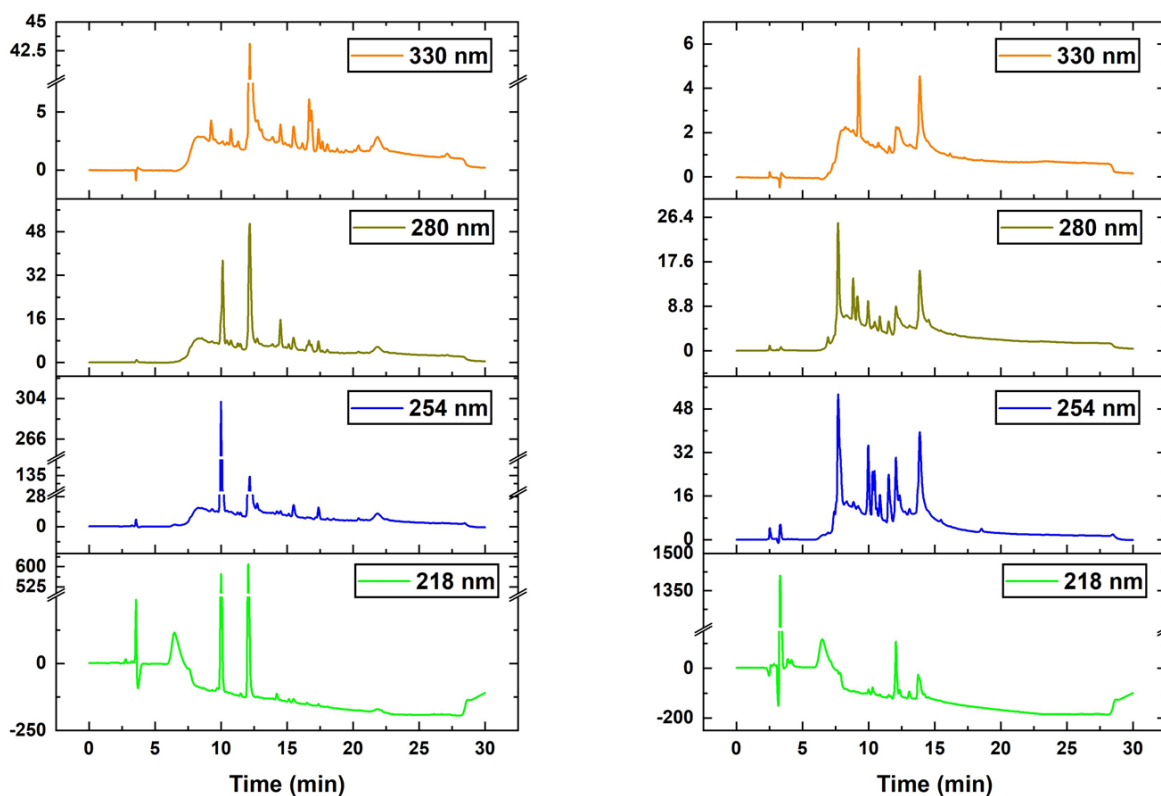


Figure 30: HPLC UV-VIS traces for Mizzou model trithiol chelator pre (**left**) and post (**right**) reduction with 10x TCEP

The characteristic peaks for the Mizzou chelator appear at RT ~ 10 & 12 min. In the 218 nm trace, both peaks were diminished after reduction with the TCEP and a new, massive UV peak was evident at the solvent front (RT ~ 3.5 min). This seems to indicate a successful reduction as the

chelator should be more soluble in the aqueous mobile phase after reduction. Again, $^{69/71}\text{Ge}$ -oxalate was buffered with NaOAc and adjusted to pH ~5 with NaOH. The buffered $^{69/71}\text{Ge}$ solution was combined with deprotected Mizzou chelator (as described in section 5.2.1) and both solutions were analyzed by radio-HPLC (as described in section 5.2.3):

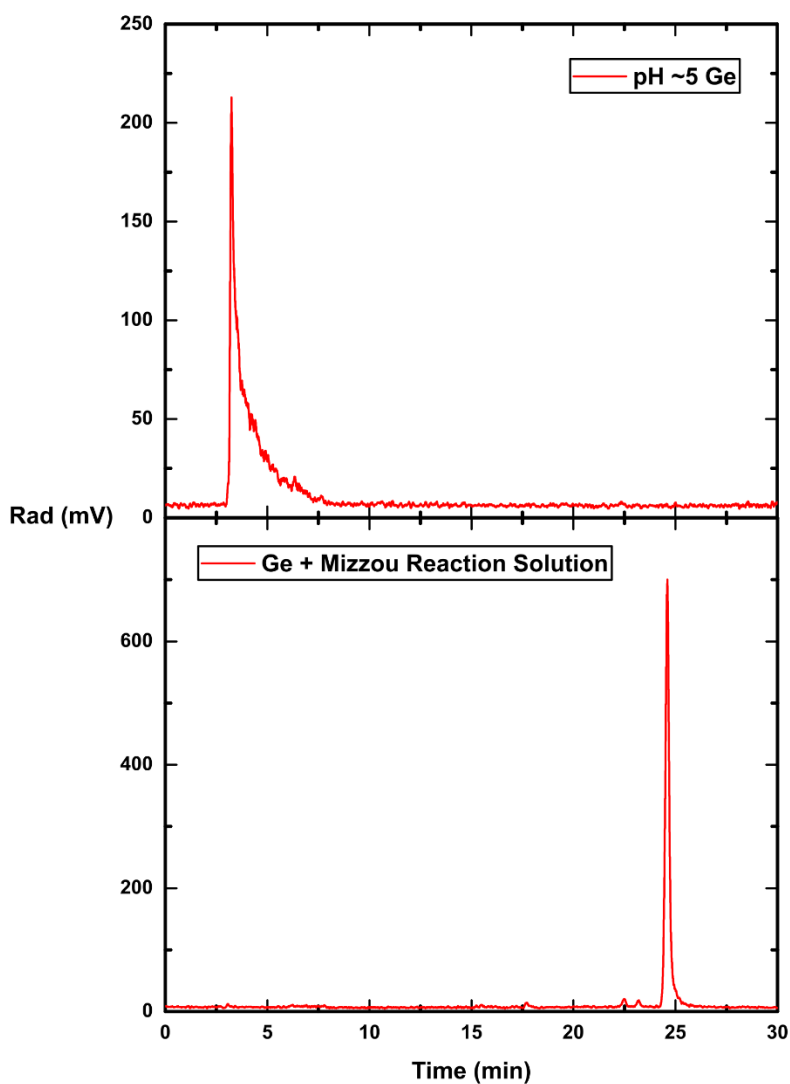


Figure 31: **upper)** Unbound $^{69/71}\text{Ge}$ -oxalate buffered to pH ~5 and **lower)** $^{69/71}\text{Ge}$ -oxalate after chelation with the Mizzou trithiol

Again, the buffered $^{69/71}\text{Ge}$ -oxalate eluted from the HPLC column with a RT of ~ 3.5 min, coincident with the solvent front. After the 2-hour reaction at $55\text{ }^\circ\text{C}$ without pH-buffering, no indications of chemical reaction were evident from the radio-HPLC trace; all the $^{69/71}\text{Ge}$ eluted at a RT of ~ 3.5 min and no other radiopeaks were observed. However, after the 2-hour reaction at pH ~ 5 , no $^{69/71}\text{Ge}$ -oxalate peak at RT ~ 3.5 min was observed. Here, 1 new radiopeak was observed at RT ~ 24 min. A few small impurity peaks were evident in the radio-HPLC trace, but by peak area amounted to $<2\%$ of the total activity, suggesting a high radiolabeling yield.

5.3.2) Purification and Stability

The LA-chelated $^{69/71}\text{Ge}$ was purified by C18 cartridge and eluted in EtOH, then dried-down and reconstituted for stability assays as described in section 5.2.2. Figure 32 shows the plotted results from radio-HPLC analysis of both solutions:

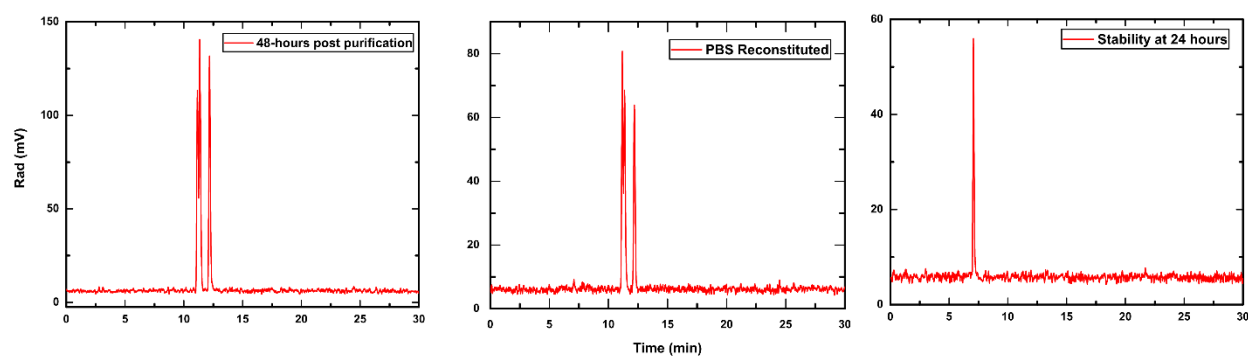


Figure 32: **left)** C18 cartridge purified $^{69/71}\text{Ge}$ -lipoate after 48 hours in EtOH; **middle)** $^{69/71}\text{Ge}$ -lipoate immediately following dry-down and reconstitution in PBS; **right)** $^{69/71}\text{Ge}$ -lipoate after 24 hours in PBS

Purification of the radiolabeled LA complex was accomplished using the C18 cartridges. The eluted product from the cartridges appeared stable for at least 48 hours post-purification in the

organic solvent. The dried-down, PBS reconstituted product also seemed stable, as the same peaks at RT ~10.5 and 12 min were the only radiopeaks present. However, after 24 hours in PBS, the $^{69/71}\text{Ge}$ -lipoate totally degraded, evidenced by a new radiopeak at RT ~7 min, corresponding neither to the $^{69/71}\text{Ge}$ -oxalate (RT ~3.5 min) nor the labeled complex (RT's ~10.5 & 12 min). Decreased LA radiolabeling yield over time was reported for radioarsenic and LA [140], though no reports in the literature are available for $^{69/71}\text{Ge}$ and LA. Because of these observations and results, $^{69/71}\text{Ge}$ -lipoate was abandoned as an ideal candidate for thiol chelation of the $^{69/71}\text{Ge}$.

The Mizzou-chelated $^{69/71}\text{Ge}$ was purified and analyzed as with the LA, and the results from those assays are plotted below (figure 33):

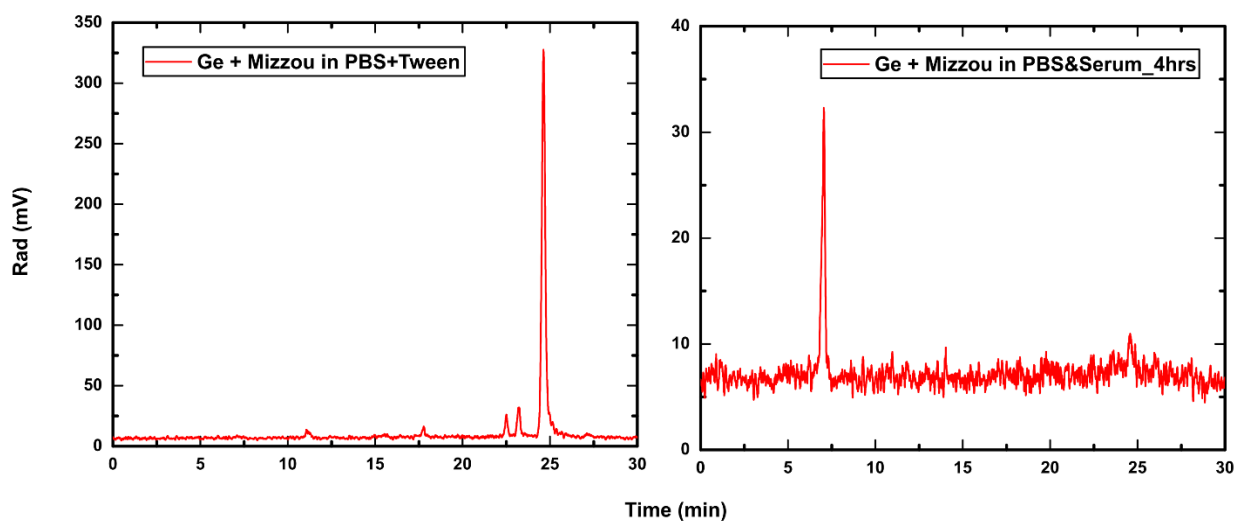


Figure 33: **left)** C18 cartridge purified $^{69/71}\text{Ge}$ -Mizzou C18 purification and dry-down and reconstitution in PBS+Tween 80; **right)** $^{69/71}\text{Ge}$ -Mizzou after 4 hours in PBS/Tween80 + Human Serum

Purification of the radiolabeled Mizzou complex was also attempted using the C18 cartridges. The dried-down complex was reconstituted in PBS but the solubility of the labeled complex in this solution was poor, leaving 30-50% of the radioactivity stuck to the vial walls after reconstitution and transfer to a fresh vial. Further reconstitutions used PBS and a biocompatible surfactant (Tween 80) to combat the challenges presented by the very hydrophobic labeled complex. In these cases, residual activity stuck to the vessel walls was negligible (<5%). The $^{69/71}\text{Ge}$ -Mizzou complex in the PBS/Tween solution seemed stable, as the same radiopeak at RT ~ 24 min was present. However, the impurity peaks were more evident, amounting to closer to 5% of the total peak area. And, after as little as 4 hours in PBS+Tween, the $^{69/71}\text{Ge}$ -Mizzou appeared to have totally degraded, as a new radiopeak at RT ~ 7 min was observed, neither corresponding to the $^{69/71}\text{Ge}$ -oxalate (RT ~ 3.5 min) nor the labeled complex (RT ~ 24 min).

The developers of the chelator reported that excess, unlabeled chelator in solution contributes to colloid formation and lack of stability for Mizzou-chelated radioarsenic, and that purification by C18 cartridge alone was insufficient to overcome this challenge, so HPLC purification is necessary [138]. Thus, a semi prep HPLC method was developed to isolate the $^{69/71}\text{Ge}$ -Mizzou complex. First, a proof-of-concept run was performed on analytical HPLC by concentrating the labeling reaction solution down to ~ 20 μL with heat and N_2 flow and injecting the entire reaction solution onto the HPLC. The labeled complex was isolated for reformulation and stability assay, and these results are plotted here:

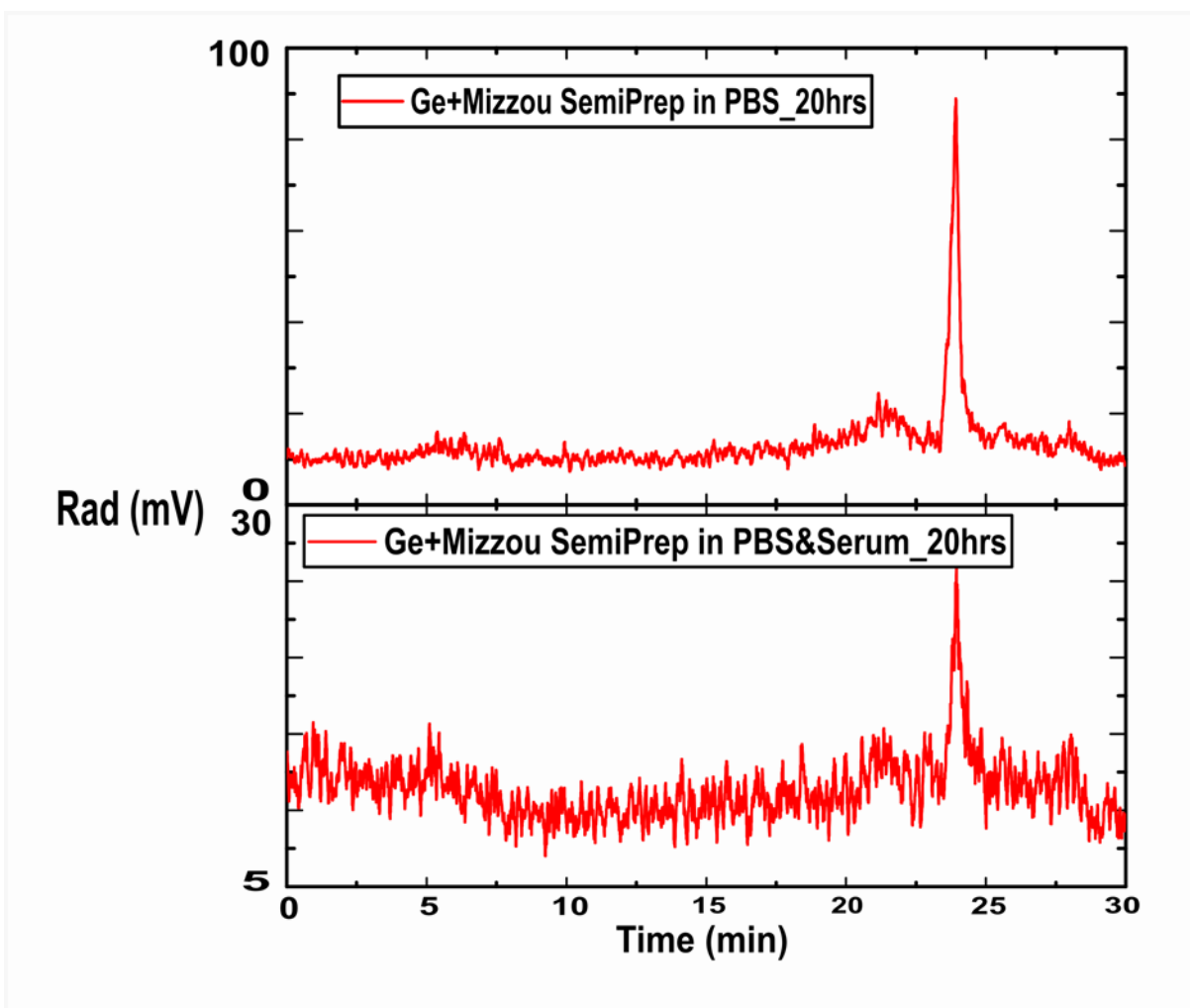


Figure 34: Proof-of-concept $^{69/71}\text{Ge}$ -Mizzou semi-prep method final product stability results in **upper)** PBS+Tween 80 and **lower)** PBS/Tween+Human Serum after 20 hours

After dry-down and reconstitution of the isolated $^{69/71}\text{Ge}$ -Mizzou complex in PBS+Tween and combining equal parts $^{69/71}\text{Ge}$ -Mizzou complex in PBS+Tween with human serum, only 1 radiopeak at RT ~ 24 min was observed in the analysis of each solution. Compared to the instability observed after just 4 hours in the PBS/Tween+Human serum (figure 33), both preparations appeared stable. Encouraged by this, the semi prep HPLC method was developed as described in section 5.2.2. The results from this method development are plotted below:

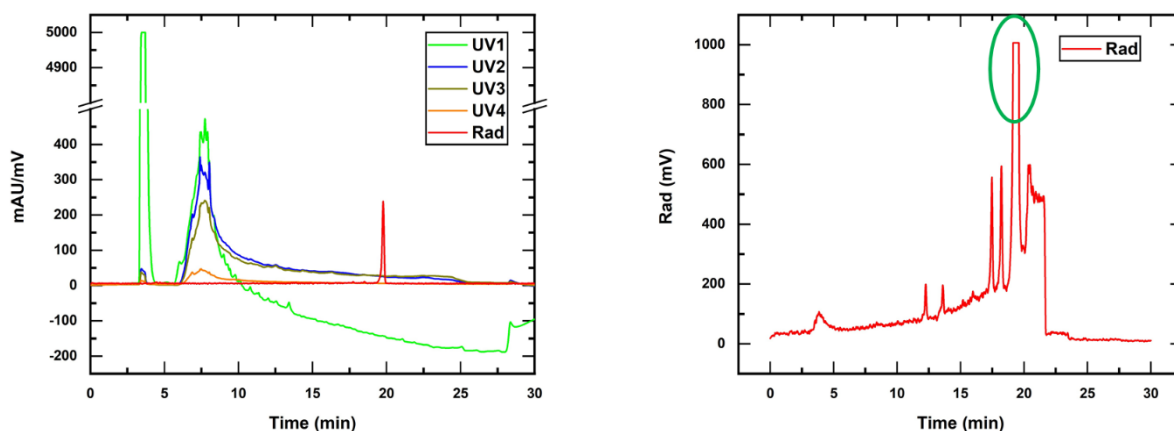


Figure 35: $^{69/71}\text{Ge}$ -Mizzou semi prep method development and RT recharacterization **left)** test run injected with UV-VIS flow cell online and **right)** full reaction solution injection with UV-VIS flow cell bypassed (peak corresponding to the labeled complex circled in green)

Because of the increased column diameter and flow rate used for semi prep, recharacterization of the RT of the $^{69/71}\text{Ge}$ -Mizzou complex was necessary. Additionally, the UV-VIS flow cell on the UltiMate 3000 HPLC system must be bypassed when large amounts of organic samples are injected to avoid clogging the small-diameter flow path and bursting liquid lines due to the subsequent back-pressure spike. So, 20 μL of the $^{69/71}\text{Ge}$ -Mizzou labeling reaction solution was diluted with the HPLC mobile phase (95% A, 5% B) to 2 mL and injected onto the system without bypassing the UV-VIS flow cell to observe the separation between the excess, unlabeled chelator, and the labeled complex. It was evident from these results that by the time the labeled complex eluted from the HPLC column (RT \sim 20 min) the bulk of the excess chelator had already been eluted to waste, and so the full run was performed with the remaining reaction solution (also diluted to 2 mL with the mobile phase). The labeled complex at the new RT was then isolated for reformulation and stability assay. These results are plotted below:

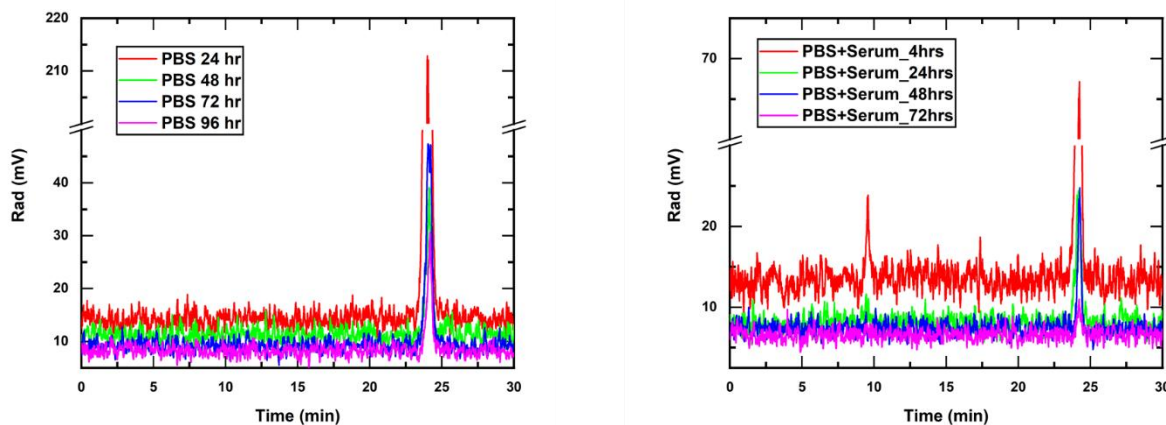


Figure 36: $^{69/71}\text{Ge}$ -Mizzou stability after reformulation in **(left) PBS+Tween** and **(right)**

PBS/Tween+Human serum over 72 – 96 hours

The overlaid radio-HPLC traces for the $^{69/71}\text{Ge}$ -Mizzou in PBS+Tween appeared stable over the 4 days observed, with no other radiopeaks observed other than the RT ~24 min peak which corresponds to the $^{69/71}\text{Ge}$ -Mizzou complex. This result was encouraging, and it was hoped that *in vitro* and *in vivo* applications could soon be enabled. The overlaid PBS + serum sample radio-HPLC traces did also appear stable, though some impurity peak was evident in the 4-hour time point (RT ~10 min). However, closer inspection of the PBS + serum samples taken for HPLC analysis using a benchtop well detector revealed that quantity of residual radioactivity in the vials was increasing over time:

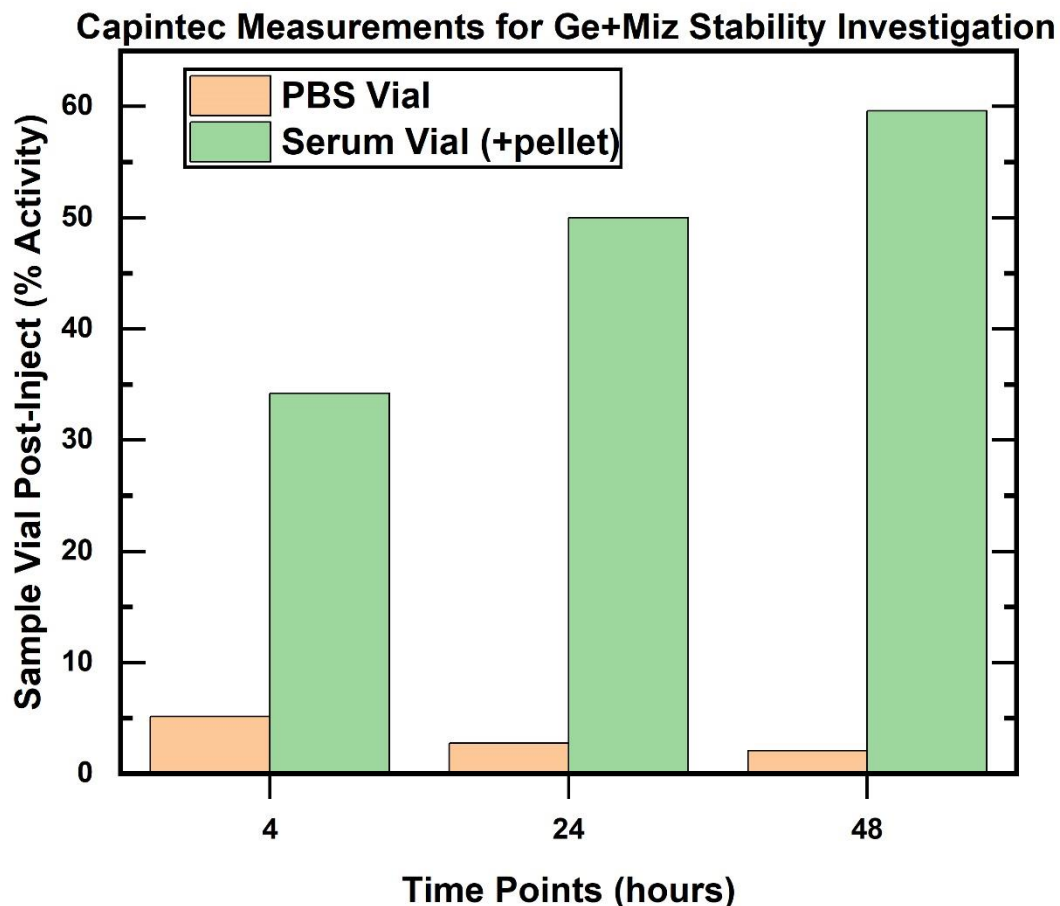


Figure 37: Serum pellet radioactivity accumulation during $^{69/71}\text{Ge}$ -Mizzou PBS & PBS+Human Serum stability study

To analyze the PBS + serum sample, aliquots were taken and combined with acetonitrile to salt out the serum proteins because they cannot be injected into the system. The aliquots were centrifuged, and the decanted supernatant was injected into the HPLC for analysis. Using a benchtop well detector to measure the samples taken for HPLC before and after injection, the residual radioactivity in the PBS and PBS+Human serum vials were quantified. For the PBS samples, the residual radioactivity in the vials was consistent with small residual liquid in the centrifuge vials. However, the activity remaining in the serum vial with the centrifuged pellet of

serum proteins increased over time. We suspect that this could be the result of trans-chelation with thiol groups on the serum proteins, albumin binding of the labeled complex, or instability of the labeled complex under simulated physiological conditions. But, because of this result, and with no obvious solution to overcome the challenge, *in vitro* and *in vivo* studies were not undertaken. However, a proposed set of future experiments would involve using a functionalized version of this chelator *in vitro* to assess cellular internalization. Hypothetically, if none of the activity was internalized, we would suspect that the complex was unstable under physiological conditions. If any activity was internalized, however, the question of instability vs transchelation/albumin binding would require further inquiry.

5.4) Conclusions

In conclusion, chelation using ligands bearing thiol functional groups shows promise. The most encouraging result was obtained using the Mizzou model trithiol chelator, but challenges with stability and formulation need further investigation before *in vitro* or *in vivo* applications can be enabled. Based on the observed complexation, the $^{69/71}\text{Ge}$ -oxalate product obtained from the developed radiochemical isolation method (chapter 4) is suitable for radiopharmaceutical preparation and investigation.

Chapter 6: Conclusions and Outlook

Immune and combination therapies for cancer show great promise [141,142]. While the need to treat cancer with ionizing radiation (both external beam and nuclear medicine) may decline, there will always be a need for diagnostic medical imaging. Therefore, efficient production of positron-emitting radionuclides for preclinical investigations, translation, and clinical applications is essential to sustain diagnostic PET imaging. The automated production of $^{61/64}\text{Cu}$ investigated in this work directly supports this goal. The production and purification of ^{69}Ge investigated here lay a rudimentary foundation upon which future successes can be built.

The automated copper production process developed and implemented at our facility can yield radiopharmaceutical quality $^{61/64}\text{Cu}$ in approximately 1 hour of processing time from natural or enriched isotopic targets of nickel and facilitates recycling of enriched target material. The application to enriched targets was demonstrated with the ^{64}Cu production. Direct radiolabeling was demonstrated with high NOTA AMAs obtained and minimal modification of the final formulation, and the radionuclidic purity of the final product met European Pharmacopoeia Standards (2020). The FASTlab chemistry module, used at more than 740 facilities worldwide to produce radiotracers for clinical application, is equipped to perform radiolabeling reactions online and deserves to be the subject of future investigations for copper-labeled radiotracers.

The results from the Co-Ga targets are convincing that the material is suitable for routine production of $^{69/71}\text{Ge}$ with minimal coproduced radioimpurities and tolerates production-scale beam intensities. The method developed in this work for radiochemical isolation of the $^{69/71}\text{Ge}$ yields ~50% of the activity at EoC, outperforming the previous method [28] for isolating the

radiogermanium from dissolved Co-Ga targets by nearly a factor of 3. The final radiochemical purity was >99% at EoC for germanium and the radionuclidic purities of the $^{69\&71}\text{Ge}$ post-processing are suitable for preclinical applications. Future work will focus on optimizing the production and separation schemes to improve the target dissolution and radiochemical yield, which is expected to increase the overall efficiency. Lastly, the results of thiol-based chelation strategies inspired by the literature are encouraging. Overcoming challenges with the stability and formulation of the radiolabeled complexes will enable *in vitro* and *in vivo* studies, thus motivating future investigations.

Appendix A: Additional XRD Data

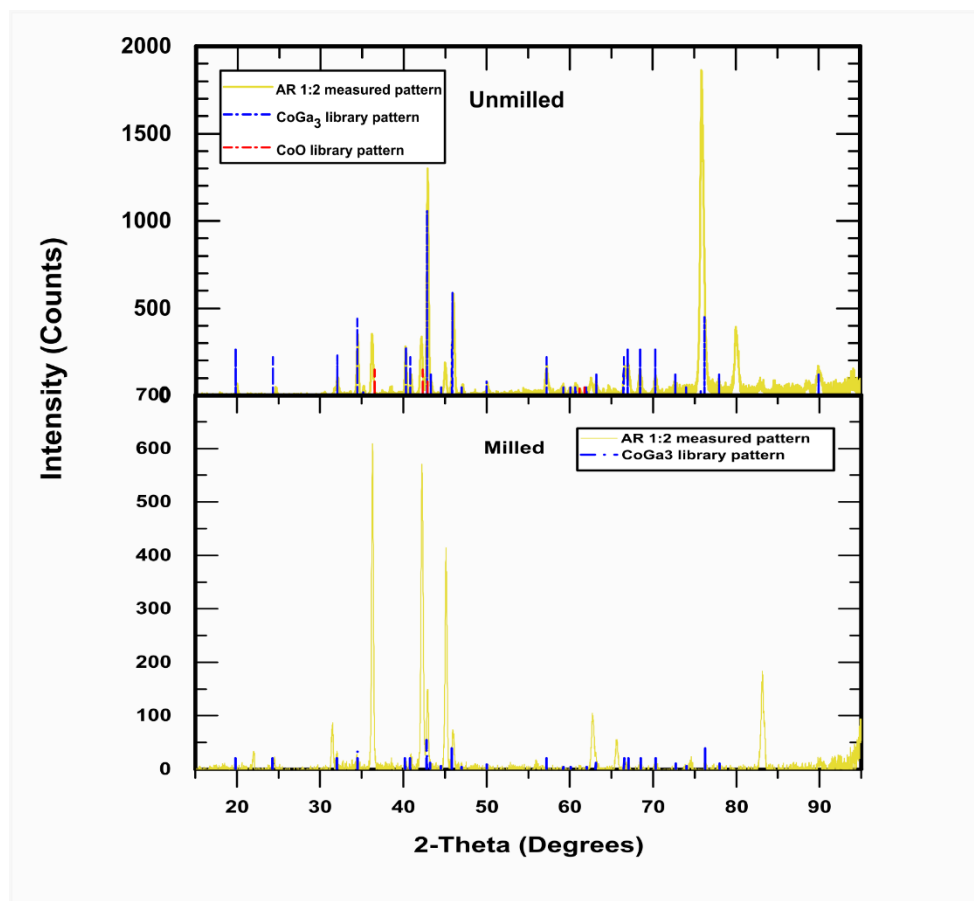


Figure A1: Measured X-ray diffraction patterns for **upper**) unmilled AR 1:2 Co:Ga sample & **lower**) milled AR 1:2 Co:Ga sample shown in gold with analysis software library matches shown in blue and red.

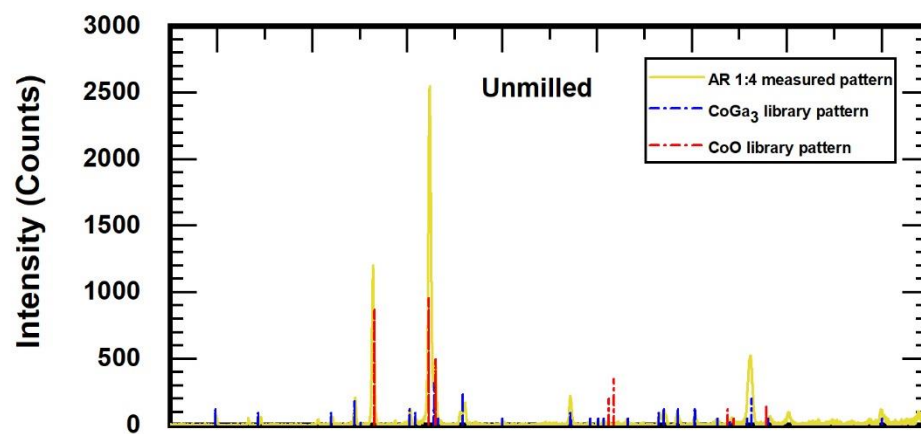


Figure A2: Measured x-ray diffraction pattern for AR 1:4 unmilled Co:Ga sample shown in gold with analysis software library matches shown in blue and red.

References

- [1] Unterrainer M, Eze C, Ilhan H, Marschner S, Roengvoraphoj O, Schmidt-Hegemann NS, et al. Recent advances of PET imaging in clinical radiation oncology. *Radiat Oncol* 2020;15:1–15. doi:10.1186/s13014-020-01519-1.
- [2] Galldiks N, Lohmann P, Albert NL, Tonn JC, Langen KJ. Current status of PET imaging in neuro-oncology. *Neuro-Oncology Adv* 2019;1:1–11. doi:10.1093/nojnl/vdz010.
- [3] Basu S, Kwee TC, Surti S, Akin EA, Yoo D, Alavi A. Fundamentals of PET and PET/CT imaging. *Ann N Y Acad Sci* 2011;1228:1–18. doi:10.1111/j.1749-6632.2011.06077.x.
- [4] Hansen SB, Bender D. Advancement in production of radiotracers. *Semin Nucl Med* 2021. doi:10.1053/j.semnuclmed.2021.10.003.
- [5] Chakravarty R, Chakraborty S. Production of a broad palette of positron emitting radioisotopes using a low-energy cyclotron: Towards a new success story in cancer imaging? *Appl Radiat Isot* 2021;176:109860. doi:10.1016/j.apradiso.2021.109860.
- [6] Svedjehed J, Kuttyreff CJ, Engle JW, Gagnon K. Automated, cassette-based isolation and formulation of high-purity $[^{61}\text{Cu}]\text{CuCl}_2$ from solid Ni targets. *EJNMMI Radiopharm Chem* 2020;5. doi:10.1186/s41181-020-00108-7.
- [7] Zhou Y, Li J, Xu X, Zhao M, Zhang B, Deng S, et al. ^{64}Cu -based radiopharmaceuticals in molecular imaging. *Technol Cancer Res Treat* 2019;18. doi:10.1177/1533033819830758.
- [8] Brandt M, Cardinale J, Aulsebrook ML, Gasser G, Mindt TL. An overview of PET radiochemistry, part 2: Radiometals. *J Nucl Med* 2018;59:1500–6. doi:10.2967/jnumed.117.190801.
- [9] de la Torre BG, Albericio F. The pharmaceutical industry in 2020. An analysis of fda drug

- approvals from the perspective of molecules. *Molecules* 2021;26:1–14.
doi:10.3390/molecules26030627.
- [10] Boschi A, Martini P, Janevik-Ivanovska E, Duatti A. The emerging role of copper-64 radiopharmaceuticals as cancer theranostics. *Drug Discov Today* 2018;23:1489–501.
doi:10.1016/j.drudis.2018.04.002.
- [11] Yordanova A, Eppard E, Kürpig S, Bundschuh RA, Schönberger S, Gonzalez-Carmona M, et al. Theranostics in nuclear medicine practice. *Onco Targets Ther* 2017;10:4821–8.
doi:10.2147/OTT.S140671.
- [12] Avila-Rodriguez MA, Nye JA, Nickles RJ. Simultaneous production of high specific activity ^{64}Cu and ^{61}Co with 11.4 MeV protons on enriched ^{64}Ni nuclei. *Appl Radiat Isot* 2007;65:1115–20.
doi:10.1016/j.apradiso.2007.05.012.
- [13] De Goeij JJM, Bonardi ML. How do we define the concepts specific activity, radioactive concentration, carrier, carrier-free and no-carrier-added? *J Radioanal Nucl Chem* 2005;263:13–8.
doi:10.1007/s10967-005-0004-6.
- [14] Kume M, Carey PC, Gaehle G, Madrid E, Voller T, Margenau W, et al. A semi-automated system for the routine production of copper-64. *Appl Radiat Isot* 2012;70:1803–6.
doi:10.1016/j.apradiso.2012.03.009.
- [15] Ometáková J, Rajec P, Csiba V, Leporis M, Štefečka M, Vlk P, et al. Automated production of ^{64}Cu prepared by 18 MeV cyclotron. *J Radioanal Nucl Chem* 2012;293:217–22. doi:10.1007/s10967-012-1757-3.
- [16] GE Healthcare. PET Radiochemistry Systems n.d.
<https://www.gehealthcare.com/products/molecular-imaging/pet-radiopharmacy/pet->

- radiochemistry?utm_medium=cpc&utm_source=google&utm_campaign=USC-PS-2021-REG-AlwaysOn&utm_term=&utm_content=12518725892&npclid=Cj0KCOjwsdiTBhD5ARIsAlpW8Cl_bHPFzrqU14FqE4Zs4QzH_g (accessed May 1, 2022).
- [17] Pagani M, Stone-Elander S, Larsson SA. Alternative positron emission tomography with non-conventional positron emitters: Effects of their physical properties on image quality and potential clinical applications. *Eur J Nucl Med* 1997;24:1301–27. doi:10.1007/s002590050156.
- [18] Boros E, Packard AB. Radioactive Transition Metals for Imaging and Therapy. *Chem Rev* 2019;119:870–901. doi:10.1021/acs.chemrev.8b00281.
- [19] Kostelnik TI, Orvig C. Radioactive Main Group and Rare Earth Metals for Imaging and Therapy. *Chem Rev* 2019;119:902–56. doi:10.1021/acs.chemrev.8b00294.
- [20] McKnight BN, Viola-Villegas NT. ⁸⁹Zr-ImmunoPET companion diagnostics and their impact in clinical drug development. *J Label Compd Radiopharm* 2018;61:727–38. doi:10.1002/jlcr.3605.
- [21] Li L, Ruan T, Lyu Y, Wu B. Advances in Effect of Germanium or Germanium Compounds on Animals—A Review. *J Biosci Med* 2017;05:56–73. doi:10.4236/jbm.2017.57006.
- [22] Kratochwil C, Haberkorn U, Giesel FL. Radionuclide Therapy of Metastatic Prostate Cancer. *Semin Nucl Med* 2019;49:313–25. doi:10.1053/j.semnuclmed.2019.02.003.
- [23] Fonslet J, Lee BQ, Tran TA, Siragusa M, Jensen M, Kibédi T, et al. ¹³⁵La as an Auger-electron emitter for targeted internal radiotherapy. *Phys Med Biol* 2018;63. doi:10.1088/1361-6560/aa9b44.
- [24] Thisgaard H, Elema DR, Jensen M. Production and dosimetric aspects of the potent Auger emitter ⁵⁸Co for targeted radionuclide therapy of small tumors. *Med Phys* 2011;38:4535–41. doi:10.1118/1.3608905.

- [25] Lee BQ, Kibédi T, Stuchbery AE. Auger yield calculations for medical radioisotopes. EPJ Web Conf 2015;91:1–6. doi:10.1051/epjconf/20159100007.
- [26] Eckerman K, Endo A. ICRP Publication 107: Nuclear Decay Data for Dosimetric Calculations 2008;38.
- [27] Filosofov D, Kurakina E, Radchenko V. Potent candidates for Targeted Auger Therapy: Production and radiochemical considerations. Nucl Med Biol 2021;94–95:1–19. doi:10.1016/j.nucmedbio.2020.12.001.
- [28] Valdovinos HF. Production , labeling and in vivo studies with the theranostic positron-emitting radiometals Sc-44, Co-55/58m/58g, Cu-61/64, Y-86 amd Ge-69. University of Wisconsin - Madison, 2017.
- [29] Mirzadeh S, Lambrecht RM. Radiochemistry of germanium. J Radioanal Nucl Chem Artic 1996;202:7–102. doi:10.1007/BF02037941.
- [30] International Atomic Energy Agency. Cyclotron Produced Radionuclides : Physical Characteristics and Production Methods. TRS-468. October 2009:279.
- [31] Ziegler JF, Ziegler MD, Biersack JP. SRIM - The stopping and range of ions in matter (2010). Nucl Instruments Methods Phys Res Sect B Beam Interact with Mater Atoms 2010;268:1818–23. doi:10.1016/j.nimb.2010.02.091.
- [32] NNDC. Chart of the Nuclides 2022. <https://www.nndc.bnl.gov/nudat3/> (accessed October 2, 2022).
- [33] Blower PJ, Lewis JS, Zweit J. Copper radionuclides and radiopharmaceuticals in nuclear medicine. Nucl Med Biol 1996;23:957–80. doi:10.1016/S0969-8051(96)00130-8.

- [34] Martin CC, Oakes TR, Nickles RJ. Small cyclotron production of [Cu-60]Cu-PTSM for PET blood flow measurements. *J Nucl Med* 1990;31:815P.
- [35] Nickles RJ. The production of a broader palette of PET tracers. *J Label Compd Radiopharm* 2003;46:1–27. doi:10.1002/jlcr.639.
- [36] Rowshanfarzad P, Sabet M, Reza Jalilian A, Kamalidehghan M. An overview of copper radionuclides and production of ^{61}Cu by proton irradiation of natZn at a medical cyclotron. *Appl Radiat Isot* 2006;64:1563–73. doi:10.1016/j.apradiso.2005.11.012.
- [37] Szelecsényi F, Blessing G, Qaim SM. Excitation functions of proton induced nuclear reactions on enriched ^{61}Ni and ^{64}Ni : Possibility of production of no-carrier-added ^{61}Cu and ^{64}Cu at a small cyclotron. *Appl Radiat Isot* 1993;44:575–80. doi:10.1016/0969-8043(93)90172-7.
- [38] Piel H, Qaim SM, Stücklin G. Excitation Functions of (p,xn)-Reactions on natNi and Highly Enriched ^{62}Ni : Possibility of Production of Medically Important Radioisotope ^{62}Cu at a Small Cyclotron. *Radiochim Acta* 1992;57:1–6. doi:10.1524/ract.1992.57.1.1.
- [39] McCarthy DW, Shefer RE, Klinkowstien RE, Bass LA, Margeneau WH, Cutler CS, et al. Efficient production of high specific activity ^{64}Cu using a biomedical cyclotron. *Nucl Med Biol* 1997;24:35–43. doi:10.1016/S0969-8051(96)00157-6.
- [40] Bonardi M. “High specific activity” radiotracers for metallotoxicological studies: Cyclotron and nuclear reactor production, radiochemical separation and “quality control”: Platinum, iridium, gold, copper and gallium 2002.
- [41] Synowiecki MA, Perk LR, Nijssen JFW. Production of novel diagnostic radionuclides in small medical cyclotrons. *EJNMMI Radiopharm Chem* 2018;3. doi:10.1186/s41181-018-0038-z.
- [42] Le VS, Howse J, Zaw M, Pellegrini P, Katsifis A, Greguric I, et al. Alternative method for ^{64}Cu

- radioisotope production. *Appl Radiat Isot* 2009;67:1324–31. doi:10.1016/j.apradiso.2009.02.069.
- [43] Smith NA, Bowers DL, Ehst DA. The production, separation, and use of ^{67}Cu for radioimmunotherapy: A review. *Appl Radiat Isot* 2012;70:2377–83. doi:10.1016/j.apradiso.2012.07.009.
- [44] Zweit J, Smith AM, Downey S, Sharma HL. Excitation functions for deuteron induced reactions in natural nickel: Production of no-carrier-added ^{64}Cu from enriched ^{64}Ni targets for positron emission tomography. *Int J Radiat Appl Instrumentation Part* 1991;42:193–7. doi:10.1016/0883-2889(91)90073-A.
- [45] Poniger SS, Tochon-Danguy HJ, Panopoulos HP, O’Keefe GJ, Peake D, Rasool R, et al. Automated production of ^{124}I and ^{64}Cu using IBA Terimo and Pinctada metal electroplating and processing modules. *AIP Conf Proc* 2012;1509:114–9. doi:10.1063/1.4773951.
- [46] Ohya T, Nagatsu K, Suzuki H, Fukada M, Minegishi K, Hanyu M, et al. Efficient preparation of high-quality ^{64}Cu for routine use. *Nucl Med Biol* 2016;43:685–91. doi:10.1016/j.nucmedbio.2016.07.007.
- [47] Matarrese M, Bedeschi P, Scardaoni R, Sudati F, Savi A, Pepe A, et al. Automated production of copper radioisotopes and preparation of high specific activity [^{64}Cu]Cu-ATSM for PET studies. *Appl Radiat Isot* 2010;68:5–13. doi:10.1016/j.apradiso.2009.08.010.
- [48] Allott L, Barnes C, Brickute D, Aboagye EO. An improved automated radiosynthesis of [^{18}F]FET- β AG-TOCA. *React Chem Eng* 2019;4:569–74. doi:10.1039/c8re00279g.
- [49] Lemaire C, Libert L, Franci X, Genon JL, Kuci S, Giacomelli F, et al. Automated production at the curie level of no-carrier-added 6-[^{18}F]fluoro- l -dopa and 2-[^{18}F]fluoro- l -tyrosine on a FASTlab synthesizer. *J Label Compd Radiopharm* 2015;58:281–90. doi:10.1002/jlcr.3291.

- [50] Jiang H, Jain MK, Cai H. HPLC-free and cassette-based nucleophilic production of [18F]FDOPA for clinical use. *Am J Nucl Med Mol Imaging* 2021;11:290–9.
- [51] Huang YY, Taylor S, Kozirowski J, Chang YN, Kao WH, Tzen KY, et al. A two-center study for the quality control of [18F]FDG using FASTlab phosphate cassettes. *Ann Nucl Med* 2016;30:563–71. doi:10.1007/s12149-016-1097-4.
- [52] Hoareau R, Bach-Gansmo T, Cumming P, Olberg DE. A new automated and putatively versatile synthesis of the PSMA-ligand derivative [18F]DCFPyL using the FASTlabTM synthesizer. *EJNMMI Radiopharm Chem* 2022;7. doi:10.1186/s41181-022-00157-0.
- [53] Edwards R, Greenwood HE, McRobbie G, Khan I, Witney TH. Robust and Facile Automated Radiosynthesis of [18F]FSPG on the GE FASTlab. *Mol Imaging Biol* 2021;23:854–64. doi:10.1007/s11307-021-01609-w.
- [54] Richter S, Wuest F. 18 F-labeled peptides: The future is bright. *Molecules* 2014;19:20536–56. doi:10.3390/molecules191220536.
- [55] Mercier F, Paris J, Kaisin G, Thonon D, Flagothier J, Teller N, et al. General method for labeling siRNA by click chemistry with fluorine-18 for the purpose of PET maging. *Bioconjug Chem* 2011;22:108–14. doi:10.1021/bc100263y.
- [56] O’Shea D, Ahmad R, Arstad E, Avory M, Chau WF, Durrant C, et al. Exploration of the structure-activity relationship of a novel tetracyclic class of TSPO ligands - Potential novel positron emitting tomography imaging agents. *Bioorganic Med Chem Lett* 2013;23:2368–72. doi:10.1016/j.bmcl.2013.02.057.
- [57] Azzouna R Ben, Alshoukr F, Leygnac S, Guez A, Gonzalez W, Rousseaux O, et al. A new 68Ga anionic concentration and purification method for automated synthesis of [68Ga]-DOTA or

- NODAGA conjugated peptides in high radiochemical purity. *J Label Compd Radiopharm* 2015;58:403–10. doi:10.1002/jlcr.3316.
- [58] Soto-Montenegro ML, Peña-Zalbidea S, Mateos-Pérez JM, Oteo M, Romero E, Morcillo MÁ, et al. Meningiomas: A comparative study of ⁶⁸Ga-DOTATOC, ⁶⁸Ga-DOTANOC and ⁶⁸Ga-DOTATATE for molecular imaging in mice. *PLoS One* 2014;9. doi:10.1371/journal.pone.0111624.
- [59] Thisgaard H, Kumlin J, Langkjær N, Chua J, Hook B, Jensen M, et al. Multi-curie production of gallium-68 on a biomedical cyclotron and automated radiolabelling of PSMA-11 and DOTATATE. *EJNMMI Radiopharm Chem* 2021;6:1–11. doi:10.1186/s41181-020-00114-9.
- [60] Bartoli F, Elsinga P, Nazario LR, Zana A, Galbiati A, Millul J, et al. Automated radiolabelling procedures for the preparation of OncoFAP-based radiopharmaceuticals for cancer imaging and therapy 2022:1–28.
- [61] Decristoforo C, Pickett RD, Verbruggen A. Feasibility and availability of ⁶⁸Ga-labelled peptides. *Eur J Nucl Med Mol Imaging* 2012;39. doi:10.1007/s00259-011-1988-5.
- [62] Sandell EB. Meaning of the Term “ Separation Factor .” *Anal Chem* 1968;40:834.
- [63] Luurtsema G, Pichler V, Bongarzone S, Seimbille Y, Elsinga P, Gee A, et al. EANM guideline for harmonisation on molar activity or specific activity of radiopharmaceuticals: impact on safety and imaging quality. *EJNMMI Radiopharm Chem* 2021;6. doi:10.1186/s41181-021-00149-6.
- [64] Coenen HH, Gee AD, Adam M, Antoni G, Cutler CS, Fujibayashi Y, et al. Open letter to journal editors on: International Consensus Radiochemistry Nomenclature Guidelines. *Ann Nucl Med* 2018;32:236–8. doi:10.1007/s12149-018-1238-z.
- [65] Batygin YK. Optimization of LANSCE proton beam performance for isotope production. *Nucl Instruments Methods Phys Res Sect A Accel Spectrometers, Detect Assoc Equip* 2019;916:8–21.

- doi:10.1016/j.nima.2018.10.071.
- [66] Gleason GI. A positron cow. *Int J Appl Radiat Isot* 1960;8:90–4. doi:10.1016/0020-708X(60)90052-1.
- [67] Steyn G, Anthony L, Azaiez F, Baard S, Bark R, Barnard A, et al. Development of New Target Stations for the South African Isotope Facility. *Instruments* 2018;2:29.
doi:10.3390/instruments2040029.
- [68] Faßbender M, Nortier FM, Phillips DR, Hamilton VT, Heaton RC, Jamriska DJ, et al. Some nuclear chemical aspects of medical generator nuclide production at the Los Alamos hot cell facility. *Radiochim Acta* 2004;92:237–43. doi:10.1524/ract.92.4.237.35596.
- [69] Meinken GE, Kurczak S, Mausner LF, Kolsky KL, Srivastava SC. Production of high specific activity ^{68}Ge at Brookhaven National Laboratory. *J Radioanal Nucl Chem* 2005;263:553–7.
doi:10.1007/s10967-005-0091-4.
- [70] Van der Meulen NP, Dolley SG, Steyn GF, van der Walt TN, Raubenheimer HG. The use of selective volatilization in the separation of ^{68}Ge from irradiated Ga targets. *Appl Radiat Isot* 2011;69:727–31. doi:10.1016/j.apradiso.2011.01.028.
- [71] Levkovski VN. Middle mass nuclides ($A=40-100$) activation cross-sections by medium energy ($E=10-50$ MeV) protons and α particles (experiments and systematics). Inter-Vesi, Moscow 1991.
- [72] Porile NT, Tanaka S, Furukawa M, Iwata S. Nuclear Reactions of Ga-69 and Ga-71 with 13-56 MeV Protons 1963;43.
- [73] Blosser HG, Handley TH. Survey of (p,n) Reactions at 12 MeV. *Phys Rev* 1955;100:1340–3.
- [74] Johnson CH, Trail CC, Galonsky A. Thresholds for (p, n) reactions on 26 intermediate-weight

- nuclei. *Phys Rev* 1958;136. doi:10.1103/PhysRev.136.B1719.
- [75] Johnson CH, Galonsky A, Ulrich JP. Proton strength functions from (p, n) cross sections. *Phys Rev* 1958;109:1243–54. doi:10.1103/PhysRev.109.1243.
- [76] Humes RM, Dell, G.F. J, Plougher WD, Hausman HJ. (p,n) Cross Sections at 6.75 MeV*. *Phys Rev* 1963;130:1522–4.
- [77] Koning AJ, Rochman D, Sublet JC, Dzysiuk N, Fleming M, van der Marck S. TENDL: Complete Nuclear Data Library for Innovative Nuclear Science and Technology. *Nucl Data Sheets* 2019;155:1–55. doi:10.1016/j.nds.2019.01.002.
- [78] Loc'h C, Maziere B, Comar D, Knipper R. A new preparation of germanium 68. *Int J Appl Radiat Isot* 1982;33:267–70. doi:10.1016/0020-708X(82)90025-4.
- [79] Ellison PA, Olson AP, Barnhart TE, Hoffman SLV, Reilly SW, Makvandi M, et al. Improved production of ⁷⁶Br, ⁷⁷Br and ^{80m}Br via CoSe cyclotron targets and vertical dry distillation. *Nucl Med Biol* 2019;1–5. doi:10.1016/j.nucmedbio.2019.09.001.
- [80] Chari A, Garay A, Arróyave R. Thermodynamic remodeling of the Co-Ga system. *Calphad Comput Coupling Phase Diagrams Thermochem* 2010;34:189–95. doi:10.1016/j.calphad.2010.02.004.
- [81] Bach HT, Claytor TN, Hunter JF, Olivas ER, Kelsey Iv CT, Engle JW, et al. Improving the survivability of Nb-encapsulated Ga targets for the production of ⁶⁸Ge. *Nucl Instruments Methods Phys Res Sect B Beam Interact with Mater Atoms* 2013;299:32–41. doi:10.1016/j.nimb.2013.01.035.
- [82] Otuka N, Takács S. Definitions of radioisotope thick target yields. *Radiochim Acta* 2015;103:1–6. doi:10.1515/ract-2013-2234.
- [83] Lin W, Wilkinson JT, Barrett KE, Barnhart TE, Gott M, Becker K V., et al. Excitation function of

- 54Fe(p, α)51Mn from 9.5 MeV to 18 MeV. Nucl Phys A 2022;1021:122424.
doi:10.1016/j.nuclphysa.2022.122424.
- [84] Barrett KE, Houson HA, Lin W, Lapi SE, Engle JW. Production, purification, and applications of a potential theranostic pair: Cobalt-55 and cobalt-58m. Diagnostics 2021;11:1–27.
doi:10.3390/diagnostics11071235.
- [85] Graves SA, Hernandez R, Fonslet J, England CG, Valdovinos HF, Ellison PA, et al. Novel Preparation Methods of 52Mn for ImmunoPET Imaging. Bioconjug Chem 2015;26:2118–24.
doi:10.1021/acs.bioconjchem.5b00414.
- [86] A.J. Koning, Rochman D, Sublet J, Dzysiuk N, Fleming M, Marck S van der. TENDL: Complete Nuclear Data Library for Innovative Nuclear Science and Technology 2021.
https://tendl.web.psi.ch/tendl_2021/tendl2021.html (accessed October 2, 2022).
- [87] Barfoot KM, Mitchell I V, Avaldi L, Eschbach HL, Gilboy WB. Si(Li) Detector efficiency below 10 keV. Nucl Inst Methods Phys Res B 1984;5:534–44. doi:10.1016/0168-583X(84)90014-4.
- [88] Hansen JS, McGeorge JC, Nix D, Schmidt-Ott WD, Unus I, Fink RW. Accurate efficiency calibration and properties of semiconductor detectors for low-energy photons. Nucl Instruments Methods 1973;106:365–79. doi:10.1016/0029-554X(73)90365-0.
- [89] Verma HR. Efficiency calibration of Si(Li) and HpGe detectors in the energy range of 5-60 keV. Pramana 1985;25:565–9. doi:10.1007/BF02847234.
- [90] Verma HR. Measurements of M and L X-ray energies and relative intensities emanating from 241Am source. Appl Radiat Isot 2017;122:41–6. doi:10.1016/j.apradiso.2017.01.005.
- [91] IAEA. Production of Long Lived Parent Radionuclides for Generators : 68Ge, 82Sr, 90Sr and 188W. IAEA Radioisot Radiopharm Ser 2010.

- [92] Ellison PA, Nickles RJ, Barnhart TE, Engle JW, Kuttyreff CJ. Intermetallic compounds of cobalt as targets for the production of theranostic radionuclides. WO2020251727A1, 2020.
- [93] Mirzadeh S, Kahn M, Grant PM, O'Brien Jr. HA. Studies of the Chemical Behavior of Carrier-Free ^{68}Ge I. Purification by Distillation from Acidic Chloride Solutions. *Radiochim Acta* 1981;28:47–9.
- [94] Cluley HJ. The determination of germanium. *Analyst* 1951;76:517–22.
doi:10.1039/AN9517600517.
- [95] Mirzadeh S. Studies of the Chemical Behavior of Carrier-Free ^{68}Ge III. Adsorption 1986.
- [96] Sandell EB. Colorimetric determination of traces of metals. vol. 69. 1944. doi:10.1097/00010694-195103000-00016.
- [97] Van der Walt TN, Vermeulen C. Thick targets for the production of some radionuclides and the chemical processing of these targets at iThemba LABS. *Nucl Instruments Methods Phys Res Sect A Accel Spectrometers, Detect Assoc Equip* 2004;521:171–5. doi:10.1016/j.nima.2003.11.410.
- [98] Pourmand A, Dauphas N. Distribution coefficients of 60 elements on TODGA resin: Application to Ca, Lu, Hf, U and Th isotope geochemistry. *Talanta* 2010;81:741–53.
doi:10.1016/j.talanta.2010.01.008.
- [99] J W Engle, V Lopez-Rodriguez, R E Gaspar-Carcamo, H F Valdovinos, M Valle- Gonzalez, F Trejo-Ballado, G W Severin, T E Barnhart, R J Nickles and MAA-R. Very high specific activity $^{66}/^{68}\text{Ga}$ from zinc targets for PET. *Appl Radiat Isot* 2012;70:1792–6.
doi:10.1016/j.apradiso.2012.03.030.Very.
- [100] Aničin I V., Yap CT. New approach to detection limit determination in spectroscopy. *Nucl Inst Methods Phys Res A* 1987;259:525–8. doi:10.1016/0168-9002(87)90835-7.

- [101] Velikyan I, Antoni G, Sørensen J, Estrada S. Organ biodistribution of Germanium-68 in rat in the presence and absence of [(68)Ga]Ga-DOTA-TOC for the extrapolation to the human organ and whole-body radiation dosimetry. *Am J Nucl Med Mol Imaging* 2013;3:154–65.
- [102] Rosenfeld G. *Studies of the Metabolism of Germanium* 1953:268–80.
- [103] Schroeder HA. *Germanium, Tin and Arsenic in Rats: Effects on growth, survival, pathological lesions and life span* 1968.
- [104] Dudley HC. *Pharmacological Studies of Radiogermanium (Ge-71)* 1960.
- [105] Mehard CW, Volcani BE. Similarity in uptake and retention of trace amounts of ³¹Silicon and ⁶⁸Germanium in rat tissues and cell organelles. *Bioinorg Chem* 1975;5:107–24. doi:10.1016/S0006-3061(00)80055-1.
- [106] Kang KS, Yun JW, Yoon BS, Lim YK, Lee YS. Preventive effect of germanium dioxide on the inhibition of gap junctional intercellular communication by TPA. *Cancer Lett* 2001;166:147–53. doi:10.1016/S0304-3835(01)00446-3.
- [107] FDA. Import Alert 54-07 2019. https://www.accessdata.fda.gov/cms_ia/importalert_139.html.
- [108] Legha SS. *Phase I Study of Spirogermanium Given Daily* 1983.
- [109] Aso H, Suzuki F, Yamaguchi T, Hayashi Y, Ebina T, Ishida N. Induction of Interferon and Activation of NK Cells and of Macrophages in Mice by Oral Administration Ge-132 , an Organic Germanium Compound. *Microbiol Immunol* 1985;29:65–74.
- [110] Slawson RM, Van Dyke MI, Lee H, Trevors JT. Germanium and silver resistance, accumulation, and toxicity in microorganisms. *Plasmid* 1992;27:72–9. doi:10.1016/0147-619X(92)90008-X.
- [111] Kaars Sijpesteijn A. Growth inhibition of bacteria by tributylgermanium acetate and its reversal

- by blood constituents. *Antonie Van Leeuwenhoek* 1968;34:85–92. doi:10.1007/BF02046418.
- [112] Mrema JEK. Spirogermanium: a new drug with antimalarial activity against chloroquine-resistant *Plasmodium falciparum* 1983:167–71.
- [113] Schroeder HA, Balassa JJ. Abnormal trace metals in man: Germanium. *J Chronic Dis* 1965;18:229–41. doi:10.1016/0021-9681(65)90150-5.
- [114] Krapf R, Schaffner T, Iten PX. Abuse of germanium associated with fatal lactic acidosis. *Nephron* 1992;62:351–6.
- [115] Sanai T, Okuda S, Onoyama K, Oochi N, Oh Y, Kobayashi K, et al. Germanium dioxide-induced nephropathy: A new type of renal disease. *Nephron* 1990;54:53–60.
- [116] Okada K. Renal failure caused by long-term use of a germanium preparation as an elixir 1989.
- [117] Slavik M, Elias L, Mrema J, Sakers JH. Laboratory and clinical studies of spirogermanium, a novel heterocyclic anticancer drug. *Drugs Exp Clin Res* 1982;8:379–85.
- [118] Keith LS, Faroon OM, Maples-reynolds N, Fowler BA. *Handbook on the Toxicology of Metals: Ch 37: Germanium* 2015.
- [119] Dixon C. *Pulmonary Toxicity Associated With Spirogermanium* 1984.
- [120] FDA. *Safety Risks Associated with Certain Bulk Drug Substances Nominated for Use in Compounding* 2018. <https://www.fda.gov/drugs/human-drug-compounding/safety-risks-associated-certain-bulk-drug-substances-nominated-use-compounding>.
- [121] Soares MA, Mattos JL, Pujatti PB, Leal AS, Dos Santos WG, Dos Santos RG. Evaluation of the synergetic radio-chemotherapy effects of the radio labelled cisplatin for the treatment of glioma. *J Radioanal Nucl Chem* 2012;292:61–5. doi:10.1007/s10967-011-1414-2.

- [122] Umbricht CA, Benešová M, Schmid RM, Türler A, Schibli R, van der Meulen NP, et al. 44Sc-PSMA-617 for radiotheragnostics in tandem with 177Lu-PSMA-617—preclinical investigations in comparison with 68Ga-PSMA-11 and 68Ga-PSMA-617. *EJNMMI Res* 2017;7. doi:10.1186/s13550-017-0257-4.
- [123] de Blois E, Sze Chan H, Naidoo C, Prince D, Krenning EP, Breeman WAP. Characteristics of SnO₂-based 68Ge/68Ga generator and aspects of radiolabelling DOTA-peptides. *Appl Radiat Isot* 2011;69:308–15. doi:10.1016/j.apradiso.2010.11.015.
- [124] Rösch F. Past, present and future of 68Ge/68Ga generators. *Appl Radiat Isot* 2013;76:24–30. doi:10.1016/j.apradiso.2012.10.012.
- [125] Chakravarty R, Shukla R, Ram R, Tyagi AK, Dash A, Venkatesh M. Development of a nano-zirconia based 68Ge/68Ga generator for biomedical applications. *Nucl Med Biol* 2011;38:575–83. doi:10.1016/j.nucmedbio.2010.10.007.
- [126] Lambrecht RM, Sajjad M. Accelerator-Derived Radionuclide Generators. *Radiochim Acta* 1988;43:171–80. doi:10.1524/ract.1988.43.3.171.
- [127] Neirinkx R. Potential Column Chromatography Generators for Ionic Ga-68 1979;20.
- [128] Chakravarty R, Valdovinos HF, Chen F, Lewis CM, Ellison PA, Luo H, et al. Intrinsically Germanium-69 Labeled Iron Oxide Nanoparticle: Synthesis and In Vivo Dual-modality PET/MR Imaging. *Adv Mater* 2014;26:5119–23. doi:10.1016/j.physbeh.2017.03.040.
- [129] Arefyeva N, Sandleben A, Krest A, Baumann U, Schäfer M, Kempf M, et al. [2 × 2] molecular grids of ni(ii) and zn(ii) with redox-active 1,4-pyrazine-bis(thiosemicarbazone) ligands. *Inorganics* 2018;6:1–18. doi:10.3390/INORGANICS6020051.
- [130] Santoro A, Vileno B, Palacios Ò, Peris-Díaz MD, Riegel G, Gaiddon C, et al. Reactivity of Cu(II)-,

- Zn(II)- and Fe(II)-thiosemicarbazone complexes with glutathione and metallothionein: From stability to dissociation to transmetallation. *Metallomics* 2019;11:994–1004.
doi:10.1039/c9mt00061e.
- [131] Whitnall M, Howard J, Ponka P, Richardson DR. A class of iron chelators with a wide spectrum of potent antitumor activity that overcomes resistance to chemotherapeutics. *Proc Natl Acad Sci U S A* 2006;103:14901–6. doi:10.1073/pnas.0604979103.
- [132] Eußner JP, Dehnen S. Formation of thiosemicarbazone-functionalized complexes with (GeS₂)₂ and (SnS₂)₂ units. *Zeitschrift Fur Anorg Und Allg Chemie* 2012;638:1827–32.
doi:10.1002/zaac.201200292.
- [133] Verma A, Varshney AK. Coordination compounds of germanium (IV) with semicarbazones and thiosemicarbazones and their biological studies. *Int J Pharm Sci Rev Res* 2015;30:18–21.
- [134] Singh R V., Gupta P, Chaudhary P, Deshmukh CN. Coordination compounds of germanium(IV) formed with soft and hard donor atoms: A look into the past and present work. *Main Gr Met Chem* 2005;28:93–118. doi:10.1515/MGMC.2005.28.2.93.
- [135] LeMaster DM, Minnich M, Parsons PJ, Anderson JS, Hernández G. Tetrathiolate coordination of germanium(IV) in a protein active site. *J Inorg Biochem* 2006;100:1410–2.
doi:10.1016/j.jinorgbio.2006.03.014.
- [136] Pokrovski GS, Martin F, Hazemann JL, Jacques Schott. An X-ray absorption fine structure spectroscopy study of germanium-organic ligand complexes in aqueous solution. *Chem Geol* 2000;163:151–65. doi:10.1016/S0009-2541(99)00102-3.
- [137] Rosenberg E. Germanium: Environmental occurrence, importance and speciation. *Rev Environ Sci Biotechnol* 2009;8:29–57. doi:10.1007/s11157-008-9143-x.

- [138] Najafi Khosroshahi F, Feng Y, Ma L, Manring S, Rold TL, Gallazzi FA, et al. A New, Second Generation Trithiol Bifunctional Chelate for $^{72,77}\text{As}$: Trithiol(b)-(Ser) $_2$ -RM $_2$. *Bioconjug Chem* 2021;32:1364–73. doi:10.1021/acs.bioconjchem.0c00658.
- [139] Czaplicki S. *Chromatography in Bioactivity Analysis of Compounds*. Column Chromatogr 2013. doi:10.5772/55620.
- [140] Ellison PA, Barnhart TE, Chen F, Hong H, Zhang Y, Theuer CP, et al. High Yield Production and Radiochemical Isolation of Isotopically Pure Arsenic-72 and Novel Radioarsenic Labeling Strategies for the Development of Theranostic Radiopharmaceuticals. *Bioconjug Chem* 2016;27:179–88. doi:10.1021/acs.bioconjchem.5b00592.
- [141] Pouget JP, Navarro-Teulon I, Bardiès M, Chouin N, Cartron G, Pèlerin A, et al. Clinical radioimmunotherapy-the role of radiobiology. *Nat Rev Clin Oncol* 2011;8:720–34. doi:10.1038/nrclinonc.2011.160.
- [142] Sihver W, Pietzsch J, Krause M, Baumann M, Steinbach J, Pietzsch HJ. Radiolabeled cetuximab conjugates for EGFR targeted cancer diagnostics and therapy. *Pharmaceuticals* 2014;7:311–38. doi:10.3390/ph7030311.